Study of the Kerr phase-interrogator and its applications

by

Yang Lu

Thesis submitted to the
Faculty of Graduate and Postdoctoral Studies
In partial fulfillment of the requirements for the Degree of

Doctor of Philosophy

in

Physics

Ottawa-Carleton Institute for Physics
University of Ottawa

To my family

Abstract

This thesis proposes and develops a novel optic configuration, Kerr phase-interrogator, which investigates the phase-shift between two sinusoidally modulated optical signals (SMOS) utilizing Kerr effect. The Kerr phase-interrogator gives birth to an entirely new technique for measuring the phase-shift between two light-waves. Taking advantage of all-optical signal processing, ultrafast responses, and being free from the coherent properties of a laser source, the Kerr phase-interrogator based technique for measuring the phase-shift is a promising novel approach for monitoring and sensing applications.

The thesis begins with theoretically demonstrating the operation of Kerr phase-interrogator. As the core of optical process occurs in Kerr phase-interrogator, nonlinear interactions between two SMOSs in the Kerr medium are theoretically analyzed utilizing the models of nonlinear phase-modulation and four-wave mixing (FWM). The phase-modulation-based model is intuitive and allows for conceptual understanding of the operation of the Kerr phase-interrogator. However, this model does not account for the impact of chromatic-dispersion (CD) of the Kerr medium on the operation of the Kerr phase-interrogator. Compared with the former model, the FWM-based model is essential for acquiring insight into Kerr phase-interrogator, and can explain the CD impact of the Kerr medium. The analytical solution of the power of the first order sideband as a result of the nonlinear interaction is obtained in both theoretical models. The obtained solution shows sinusoidal dependence of the power on the phase-shift of the SMOSs. Utilizing this sinusoidal dependence, the phase-shift of two SMOSs can be acquired by measuring the power of the first-order sideband.

Birefringence and CD are critical factors that affect the nonlinear interactions and thus impact the operation of Kerr phase-interrogator. In this work, vector analysis is performed on the nonlinear interaction between two SMOSs in a Kerr medium with randomly varying birefringence, and the effect of polarization-states of SMOSs on the operation of Kerr phase-interrogator is investigated. Impact of CD of Kerr medium on the operation of Kerr phase-interrogator is theoretically investigated using theory of FWM and is experimentally verified.

Four typical applications, which comprehensively reflect the advantages of Kerr phase-interrogator, are proposed and experimentally demonstrated in this thesis. First, we present a novel approach for measurements of CD in long optical fibers using a Kerr phase-interrogator. The Kerr phase-interrogator measures the phase variation of a SMOS induced by CD in a fiber under test as the laser carrier wavelength is varied. This approach takes advantage of all-optical signal-processing based on Kerr effect to acquire the phase variation, and consequently removes the requirement of complex electrical signal-processors in existing techniques of CD measurement. CD measurement for several fibers is experimentally demonstrated.

Second, a novel temperature sensor that utilizes temperature dependence of reflection group-delay in a linearly chirped fiber Bragg grating is presented. The reflection group-delay of chirped grating changes with temperature leading to a

variation in the phase of a SMOS reflected from the grating. A Kerr phase-interrogator converts the phase-variation into power variation allowing for temperature sensing with a resolution of 0.0089 ^{o}C and a sensitivity of 1.122 rad/^{o}C.

Third, a Kerr phase-interrogator is applied for implementation of real-time CD monitoring. CD induces a phase-shift between two SMOSs carried by two different wavelengths. A Kerr phase-interrogator converts the phase-shift into power variation and CD monitoring is achieved by measurement of the power variation in real time with a resolution of 0.196 ps/nm. This application takes advantages of ultrafast response of Kerr phase-interrogator and achieves the real-time monitoring.

Lastly, a novel approach for incoherent optical frequency-domain reflectometry based on a Kerr phase-interrogator is presented. The novel approach eliminates the limitation of finite coherent length of the light source, and achieves measurement of long-range distance beyond the coherent length of the light source. Long-range detection of reflection points as far as 151 km at a spatial-resolution of 11.2 cm is experimentally demonstrated.

Statement of Originality

This work contains no material which has been accepted for the award of any other degree or diploma in any university or other tertiary institution and, to the best of my knowledge and belief, contains no material previously published or written by another person, except where due reference has been made in the text.

I give consent to this copy of my thesis, when deposited in the University Library, being available for loan and photocopying.

SIGNED:……..

DATA:……..

Supervisor: Prof. Xiaoyi Bao

Acknowledgments

It is my great honor to take this opportunity to thank all the people who have helped me during my doctoral study.

First and foremost, I would like to thank my supervisor, Prof. Xiaoyi Bao for offering me the opportunity to pursue my doctoral degree in fiber optics group. She is a supervisor in my research field and a friend in my daily life. Her patience and great encouragement got me through the tough time in the first year of my study. With her strong passion, diligence, and rigorousness in research, she sets me a good example of how to be an outstanding researcher. Her dedication and perseverance towards her research is respectable, and will always be regarded as inspiring model in my future research. I would also express my great gratitude to Prof. Liang Chen. His profound knowledge in physics and mathematics impress me deeply, and his critical and thoughtful approach to problems has always been the source of improvement of my work.

I would like to give my most sincere thanks to Dr. Chams Baker for his great ideas, instructive suggestions and strict requirements on my work. I am deeply impressed by his profound knowledge, strong passion as well as his kindness, and have learned so much from him. This thesis would be impossible without his continuous guidance.

I would like to appreciate Dr. Meng Pang. His guidance benefits me a lot in terms of how to analyze and solve the problems that I meet during the research. I am

thankful to Dr. Ping Lu for his thoughtful discussions and valuable suggestions on my research. Spatial thanks are given to Jia Song who joined in the fiber optics group at the same time with me. His company made me brave and confident to face the challenges in my first year in Canada. Many thanks to other colleagues in fiber optics group: Mr. Yanping Xu, Ms. Meiqi Ren, Mr. Dao Xiang, Dr. Zengguang Qin, Prof. Zhonghua Ou, Dr. Yang Li, Ms. Qian He, Mr. Song Gao, Dr. Wenhai Li, Dr. Daisy Williams and Mr. Bhavaye Saxena. Their company made my life in Ottawa wonderful. It is a memorable experience to work together with them on several exciting research projects. I am also thankful to my roommates and friends, Yu Wang and Zhong Han. The time I lived with them is unforgettable to me.

Special thanks to Prof. Zhou Meng and Prof. Weihong Hua for their guidance and help during my graduate studies at National University of Defense Technology in China. I would like to acknowledge China Scholar Council for the funding support over the past three years.

I shall sincerely thank my fiancée Lanqing. No words can describe my apology, gratitude and appreciation to her. Her understanding, support, tolerance and patience are the motivation for me to pursue my study.

Last, but not the least, I am deeply indebted to my parents for being understanding and supportive throughout my life in Canada! I dedicate this dissertation to them.

Content

List of Figure

List of Tables

List of Acronyms

AM	Amplitude Modulation
APC	Angle-Polished Connector
BIF	Bend-Insensitive Fiber
CD	Chromatic Dispersion
CDE	Chromatic Dispersion Emulator
C-OFDR	Coherent Optical Frequency Domain Reflectometry
CW	Continuous-Wave
DSF	Dispersion Shifted Fiber
EDFA	Erbium-Doped Fiber Amplifier
EOM	Electro-Optic Modulator
FBG	Fiber Bragg Grating
FUT	Fiber Under-Test
FWM	Four-Wave Mixing
I-OFDR	Incoherent Optical Frequency Domain Reflectometry
LC-FBG	Linearly Chirped Fiber Bragg Grating
LDF	Low-Dispersion Fiber
M	Mirror
OBPF	Optical Band-Pass Filter
OFDR	Optical Frequency-Domain Reflectometry
OSA	Optical Spectrum Analyzer

OSC	Oscilloscope
P	Power
PD	Photodiode
PBC	Polarization Beam Combiner
PBS	Polarization Beam Splitter
PC	Polarization Controller
PMC	Polarization-Maintaining Circulator
PMF	Polarization-Maintaining Fiber
PSD	Power Spectral Density
PWM	Power Meter
RF	Radio Frequency
S	Speaker
SMF	Single-Mode Fiber
SMOS	Sinusoidally Modulated Optical Signal
SNR	Signal-to-Noise Ratio
SOP	State of polarization
SPM	Self-Phase Modulation
SWG	Sinusoidal Waveform Generator
TL	Tunable Laser
UPC	Ultra-Polished Connector
VDL	Variable Delay Line
XPM	Cross-Phase Modulation

1 Introduction

1.1 The Kerr phase-interrogator

A Kerr phase-interrogator is a novel approach for measuring the phase-shift between two sinusoidally modulated optical signals (SMOS). We begin with two sinusoidally modulated optical powers of two continuous light-wave signals, whose power can be given as $P_{j=1,2} = P_0 \cos(\phi_j)$ where *j*=1,2 refers to two optical signals, $\phi_j = 2\pi f_{s,j} t - \phi_{j,0}$ is the phase of the SMOS, $f_{s,j}$ is oscillation frequency, and $\phi_{j,0}$ is initial phase shift of the SMOS. By exploiting the nonlinear Kerr effect induced from a km-long single mode fiber [1], which results in the generation of sidebands in the optical spectra, the proposed Kerr phase-interrogator translates the phase-shift $\Delta\phi = \phi_2 - \phi_1$ between these two SMOSs into sinusoidal power-variation of these sidebands, which can then be easily detected using basic opto-electronic devices.

By manipulating the oscillation frequencies of the two SMOSs, the newly developed Kerr phase-interrogator can be realized two different scenarios. The first scenario consists of identical oscillation frequencies $f_{s,1} = f_{s,2}$, from which $\Delta\phi = \phi_{2,0} - \phi_{1,0}$ is obtained, and a Kerr phase-interrogator measures the difference in the initial phases of two SMOSs. In the other case, we use two different oscillation frequencies $f_{s,1} \neq f_{s,2}$, resulting in $\Delta\phi = 2\pi(f_{s,2} - f_{s,1})t - (\phi_{2,0} - \phi_{1,0})$ which varies with time, so that the phase information is embedded on a signal with the beat frequency $\Delta f_s = f_{s,2} - f_{s,1}$, which can then be measured by a Kerr phase-interrogator.

1.2 Thesis contribution

This thesis proposes and demonstrates an entirely new approach for measuring the phase-shift between two SMOSs. Utilizing the nonlinear Kerr effect, the Kerr phase-interrogator has unique merits such as ultrafast response time, utilization of all-optical signal processing, and independence of coherence properties of the laser sources, which makes Kerr phase-interrogator promising and practical in a wide range of applications. The novel phase-interrogator open a completely new and powerful way for phase-shift measurements.

In the beginning of this thesis, the operation of Kerr phase-interrogator is theoretically analyzed. Specifically, we derive the nonlinear interaction between two SMOSs in the Kerr medium analytically using two different approaches which rely on the third-order susceptibility present in silica-based single-mode fibers [1]. The first approach utilizes pre-existing equations of the intensity-dependent nonlinear phase-modulation induced over each SMOS, which provides an intuitive understanding of the operation of the Kerr phase-interrogator. The second approach is more thorough and is derived from the rate equations of FWM in silica fibers [1]. This approach provides more insight into the Kerr phase-interrogator with regards to nonlinear interaction between the electrical fields of the SMOSs in the fiber.

From these analyses, we realized that CD and birefringence also begin to play an important role in the nonlinear-interaction process, which affect the operation of Kerr phase-interrogator. In this thesis, impact of CD and birefringence of Kerr medium on the generation of first-order sideband is analyzed. The analyses accurately predict the

impact of CD and birefringence as confirmed by the close agreement between theoretical and experimental results. The theoretical study supplements the theory of Kerr phase-interrogator, and provides the tools required to optimize the performance of the Kerr phase-interrogator in terms of achieving the best signal-to-noise ratio, sensitivity and accuracy.

The advantages of Kerr phase-interrogator make it an optimized approach in monitoring and sensing applications when compared with existing approaches, and open ways for novel sensing applications. In this thesis, four typical applications of Kerr phase-interrogator are proposed and demonstrated theoretically and experimentally.

The first application of Kerr phase-interrogator demonstrated in this thesis is CD characterization of optical fibers. Current method of CD characterization measures the shift in the phase of a SMOS induced by propagation in a fiber under-test as the laser wavelength is varied allowing for the determination of the relative group-delay as a function of wavelength. CD is then obtained using the wavelength dependence of the relative group-delay. Current implementations of this method utilize electronic signal-processing for phase-shift acquisition [2, 3]. Utilization of high oscillation-frequency of the SMOS guarantees high-resolution of relative group-delay measurement and that of CD measurements. However, high oscillation-frequency leads to the requirement of a broadband electronic signal-processor, which dramatically increases the cost of CD measurements. Unlike conventional modulation phase-shift implementations, the proposed approach acquires the phase-shift of a

SMOS by all-optical signal-processing based on Kerr effect rather than electronic signal-processing. The utilization of all-optical signal processing eliminates the requirement of broadband electronic signal-processor, and ensures both high-resolution and low cost of CD measurements.

The Kerr phase-interrogator is also applied to high-resolution temperature sensing based on linearly-chirped fiber Bragg grating (LC-FBG). Existing FBG-based temperature sensors measure temperature variation by measuring shift in the central wavelength of the reflection spectrum. This type of FBG sensors requires a spectrum analyzer for acquisition of the reflection spectrum making temperature-sensing slow and impractical for real-time monitoring applications. Furthermore, the temperature resolution is limited by the wavelength resolution of spectrum analysis approaches. The proposed temperature sensor utilizes temperature dependence of reflection group-delay in a LC-FBG. The reflection group-delay of chirped grating changes with temperature leading to a variation in the phase of a SMOS reflected from the grating. A Kerr phase-interrogator converts the phase-variation into power variation allowing for high precision temperature sensing. Experimental measurements demonstrate temperature sensing in a LC-FBG at a sensitivity of 1.122 rad/^{o}C and a resolution of 0.0089 ^{o}C. Since the temperature-variation is acquired by mere power measurement, the proposed temperature sensor is capable of real-time temperature monitoring.

Real-time CD monitor based on Kerr phase-interrogator is also presented. Owing to the ultrafast response-time of Kerr-effect and utilization of all-optical signal processing, this novel approach can respond to dispersion-variation as fast as

femtosecond, which is only limited by the response-time of Kerr effect. In addition, the proposed CD monitor accomplishes real-time CD monitoring by a mere power measurement, and hence is free from complex signal acquisition that is required in current CD monitor [4-7]. Due to the temperature and strain dependence of CD in optical fibers and chirped FBG, CD monitor can be used for sensing applications. Therefore, the high sensitivity and fast response of the proposed CD monitoring approach opens the way for novel sensing applications.

Lastly, a Kerr phase-interrogator is configured for incoherent optical frequency domain reflectometry, which eliminates the limitation of finite coherent length of the light source. For the proposed approach, the maximum measurable range is only limited by the loss over long-distance transmission, and measurement of long-range distance beyond the coherent length of the light source is achieved by the proposed approach.

1.3 Thesis outline

This thesis contains nine chapters and is organized as follows:

Chapter 2 theoretically demonstrates the operation of Kerr phase-interrogator using the model of phase-modulation. Analysis on the nonlinear interaction between two orthogonally polarized SMOSs is presented, and the analytical solution of first-order sidebands arising from the nonlinear interaction is obtained. Impact of peak-power difference of the two SMOSs on the generation of first-order sidebands is investigated in this chapter.

Chapter 3 performs vector analysis of nonlinear interaction between two SMOSs with orthogonal polarization-states or identical polarization-state in a Ker medium with randomly varying birefringence, and the generation of first-order sidebands in the cases of these two polarization-schemes is investigated theoretically and experimentally.

Chapter 4 studies the impact of CD of Kerr medium on the nonlinear interaction between two SMOSs using theory of FWM, and the impact of the CD on the generation of first-order sidebands is theoretically and experimentally demonstrated.

Four applications of Kerr phase-interrogator are theoretically and experimentally demonstrated in the following four chapters. In chapter 5, CD characterization of optical fibers based on Kerr phase-interrogator is demonstrated. Chapter 6 presents a high-resolution temperature sensor based on LC-FBG and Kerr phase-interrogator. A real-time CD monitor based on a Kerr phase-interrogator is presented in chapter 7. Chapter 8 demonstrates an incoherent optical frequency domain reflectometry based on a Kerr phase-interrogator for long-range distance measurement with high spatial resolution.

Chapter 9 concludes all the work in this thesis and proposes possible directions for future research.

2 Operation principle of a Kerr phase-interrogator

In this chapter, the operation principle of Kerr phase-interrogator that acquires phase-shift of two sinusoidally modulated optical signals (SMOS) is theoretically demonstrated. Generation of the first-order sideband that arises from sinusoidal phase-modulations induced by two orthogonally polarized SMOSs through Kerr effect is analyzed. The analytical solution of power generated by first-order sideband P_1 is obtained showing sinusoidal variation with the phase-shift of the orthogonally polarized SMOSs. The phase-shift is then demodulated from the sinusoidal variation of P_1. This phase-modulation-model based analysis is intuitive to understand the operation of the Kerr phase-interrogator.

Generation of sidebands using an electro-optic modulator is also demonstrated in this chapter. The double sidebands generation provides sinusoidally modulated optical signals required in a Kerr phase-interrogator.

2.1 Operation principle of a Kerr phase-interrogator

Figure 2.1 presents a schematic of a Kerr phase-interrogator. Two SMOSs oscillate at f_s, and the optical spectrum of each SMOS consists of two distinct peaks centered at $v_{j=1,2}$ and separated by $\Delta v=f_s$, where v_1 and v_2 are the optical frequencies

and could be either identical or different. The parallel and perpendicular components of the SMOSs are respectively combined by a polarization beam combiner (PBC) to obtain two orthogonally polarized SMOSs. The usage of orthogonally polarized SMOSs avoids the interference between the electric fields of the SOMSs. Two polarization controllers, PC1 and PC2, maximize and equalize the powers of the parallel and perpendicular components at the output of PBC.

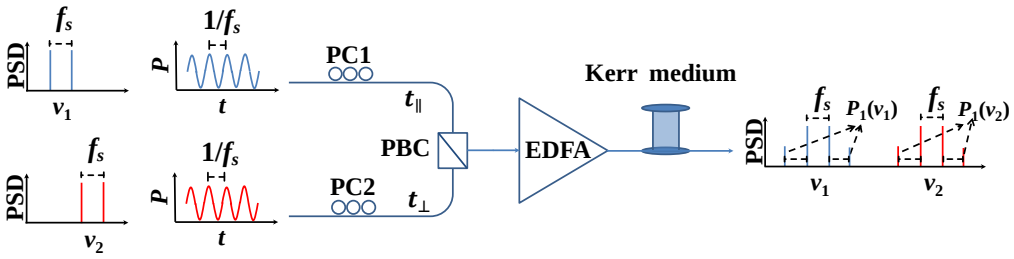

Figure 2.1: Schematic of a Kerr phase-interrogator, and illustrations of the optical spectra of the SMOSs at different positions of the setup. PC: polarization controller; PBC: polarization beam combiner; EDFA: erbium-doped fiber amplifier; PSD: power spectral density; P: power.

The parallel and perpendicular components at the output of PBC are given by

$$A_{\|0} = \sqrt{\frac{P_P}{2}} \cos\left[\pi f_s \left(t - t_{\|0}\right)\right] \tag{2.1}$$

$$A_{\perp 0} = \sqrt{\frac{P_P}{2}} \cos\left[\pi f_s \left(t - t_{\perp 0}\right)\right] \tag{2.2}$$

where P_P is the peak power of the combined SMOS, $t_{\|0}$ and $t_{\perp 0}$ are the group-delay of the parallel and perpendicular components respectively with the difference $t_d = t_{\|0} - t_{\perp 0}$. The combined signal at the output of PBC is amplified using an Erbium-doped fiber amplifier and then is launched into a Kerr medium comprised of dispersion-shifted fiber with a length L_{Kerr}.

The amplified signal propagating in the Kerr medium undergoes self-phase

modulation (SPM) and cross-phase modulation (XPM). The amplitude of the parallel and perpendicular field components at the output of the Kerr medium are given by

$$A_{\parallel} = \sqrt{\frac{P_P}{2}} \cos\left[\pi f_s \left(t - t_{\parallel}\right)\right] \exp\left(i\phi_{NL}\right) \tag{2.3}$$

$$A_{\perp} = \sqrt{\frac{P_P}{2}} \cos\left[\pi f_s \left(t - t_{\perp}\right)\right] \exp\left(i\phi_{NL}\right) \tag{2.4}$$

where $\phi_{NL} = \phi_{SPM} + \phi_{XPM} = \left(8\gamma L_{Kerr} / 9\right)\left(\left|A_{\parallel}\right|^2 + \left|A_{\perp}\right|^2\right)$ is the sinusoidal phase-modulation as a result of the superposition of SPM and XPM induced by the parallel and perpendicular field components, γ is the waveguide nonlinearity of the Kerr medium , $t_{\parallel} = t_{\parallel 0} + t_{\parallel}^{Kerr}$ and $t_{\perp} = t_{\perp 0} + t_{\perp}^{Kerr}$ are the group-delay of the parallel and perpendicular components at the output of Kerr medium respectively, with $t_{\parallel}^{Kerr}$ and $t_{\perp}^{Kerr}$ being delay-times required to travel the Kerr medium.

The factor of 8/9 in ϕ_{NL} results from mode-coupling and polarization-state average of the perpendicular and parallel fields induced by random birefringence in the Kerr medium, as will be demonstrated in detail in chapter 3. For the non-dispersive Kerr medium, one has $t_{\parallel}^{Kerr} = t_{\perp}^{Kerr}$ and thus $t_{\parallel} - t_{\perp} = t_{\parallel 0} - t_{\perp 0} = t_d$. The analysis regarding the impact of dispersion of a dispersive Kerr medium will be presented in chapter 4.

Figure 2.2 (a) presents the normalized sinusoidal phase-modulation $\phi_{NL} / \left(8\gamma L_{Kerr} P_P / 9\right)$ with f_s=20 GHz at the output of the Kerr medium for different values of t_d. The visibility $r = \left[\max\left(\phi_{NL}\right) - \min\left(\phi_{NL}\right)\right] / \left[\max\left(\phi_{NL}\right) + \min\left(\phi_{NL}\right)\right]$ of ϕ_{NL} varies between 0 and 1 based on the value of the phase-shift of orthogonally polarized SMOSs $\Delta\phi = \left|\pi f_s \left(t - t_{\perp}\right) - \pi f_s \left(t - t_{\parallel}\right)\right| = \pi f_s t_d$. The peak visibility r=1

corresponding to $\phi_{NL} = (8\gamma L_{Kerr} P_P / 9)\cos^2[\pi f_s (t - t_\perp)]$ is obtained when $\Delta\phi = 0, \pi, 2\pi, 3\pi, \ldots$ leading to the strongest time-dependent sinusoidal phase-modulation of $A_\parallel$ and $A_\perp$, and the minimum visibility $r=0$ corresponding to $\phi_{NL} = 4\gamma L_{Kerr} P_P / 9$ is obtained when $\Delta\phi = \pi/2, 3\pi/2, 5\pi/2, \ldots$ leading to a time-independent phase-modulation of $A_\parallel$ and $A_\perp$.

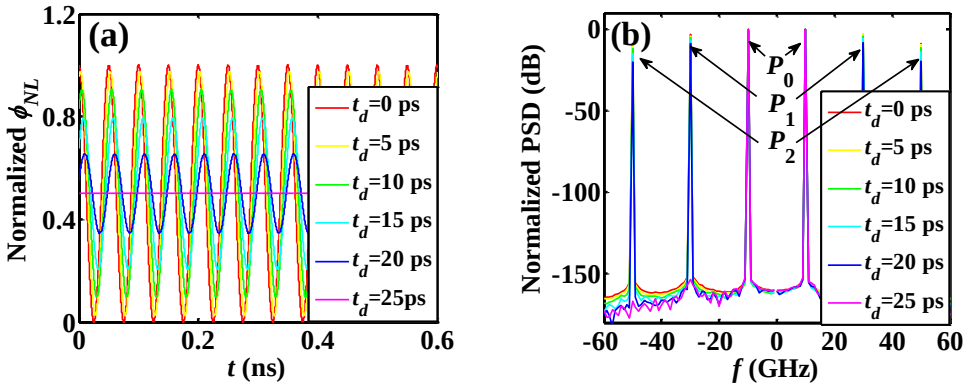

Figure 2.2: Calculated values of (a) normalized ϕ_{NL} as a function of time t and (b) normalized PSDs of the SMOS at the output of Kerr medium for different values of t_d.

The sinusoidal phase-modulation ϕ_{NL} of $A_\parallel$ and $A_\perp$ leads to the formation of distinct sidebands $P_{\parallel\perp,i}$ with i=1, 2, 3, ..., as illustrated in Fig. 2.2(b). $P_{\parallel\perp,0}$ refers to the original sidebands that form the two SMOSs. The power of first-order sideband $P_{\parallel\perp,1}$ can be derived analytically by applying the Jacobi–Anger expansion to Eqs. (2.3)–(2.4) to obtain (see Appendix A)

$$P_{\parallel,1} = \frac{P_P}{8}\left[J_1^2(\theta) + J_2^2(\theta) - 2\sin(\Delta\phi/2) J_1(\theta) J_2(\theta)\right] \tag{2.5}$$

$$P_{\perp,1} = \frac{P_P}{8}\left[J_1^2(\theta) + J_2^2(\theta) + 2\sin(\Delta\phi/2) J_1(\theta) J_2(\theta)\right] \tag{2.6}$$

where $\theta = m\cos(\Delta\phi)$, $m = 4\gamma L_{Kerr} P_P / 9$ and $J_{\alpha=1,2}(\theta)$ is Bessel function of the first kind.

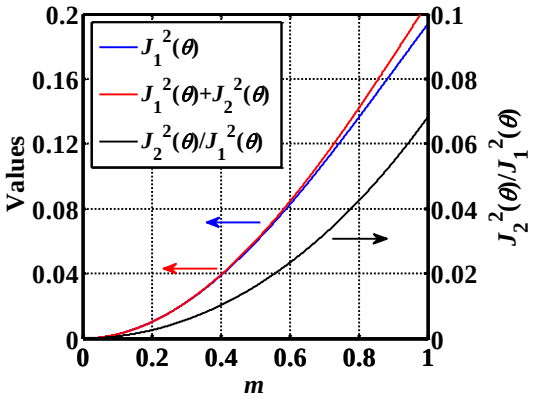

Figure 2.3: The calculated values of $J_1^2(\theta)$, $J_2^2(\theta)$ and $J_2^2(\theta)/J_1^2(\theta)$ with $\cos(\Delta\phi)=1$ as a function of m.

In the case of $v_1=v_2$, $P_{\parallel,1}$ and $P_{\perp,1}$ are overlapped in the optical spectrum, and the total power of the first-order sideband $P_1 = P_{\perp,1} + P_{\parallel,1}$ is given by

$$P_1 = \frac{P_P}{4}\left[J_1^2(\theta) + J_2^2(\theta)\right] \tag{2.7}$$

Figure 2.3 shows calculated values of $J_1^2(\theta)$, $J_1^2(\theta)+J_2^2(\theta)$ and their relative difference $J_2^2(\theta)/J_1^2(\theta)$ with $\cos(\Delta\phi)=1$ as a function of m. For m<0.4, relative difference $J_2^2(\theta)/J_1^2(\theta)$ is smaller than 0.01 indicating that $J_1^2(\theta)$ dominates in P_1 for every value of $\Delta\phi$. Therefore, Eq. (2.7) reduces to

$$P_1 = \frac{P_P}{4}J_1^2(\theta) \tag{2.8}$$

For small arguments $0 < x \ll \sqrt{\alpha+1}$, one obtains, when α is not a negative integer: $J_\alpha(x) \approx (0.5x)^\alpha / \Gamma(\alpha+1)$ [8]. For m<0.4, $0 < \theta \le m \ll \sqrt{2}$ is valid, and $J_1(\theta) = (0.5\theta)/\Gamma(2)$ is attained. Using $J_1(\theta) = (0.5\theta)/\Gamma(2)$ with $\Gamma(2)=1$, $\theta = m\cos(\Delta\phi)$ and $m = 4\gamma L_{Kerr} P_P / 9$ in Eq. (2.8) leads to

$$P_1 = \frac{\gamma^2 P_P^3 L_{Kerr}^2}{81}\cos^2(\Delta\phi) \tag{2.9}$$

In the case of $v_1 \neq v_2$, $\left|2\sin(\Delta\phi/2)J_1(\theta)J_2(\theta)\right| / J_1^2(\theta) \le 0.05$ is valid for m<0.2 as indicated in Fig. 2.3. As a result, $J_1^2(\theta)$ dominates in Eq. (2.5) an Eq. (2.6),

and consequently $P_{\|,1}$ and $P_{\perp,1}$ are approximately given by

$$P_{\|,1} = P_{\perp,1} = \frac{P_P J_1^2(\theta)}{8} = \frac{\gamma^2 P_P^3 L_{Kerr}^2}{162}\cos^2(\Delta\phi) \tag{2.10}$$

Equations (2.9)–(2.10) indicate that the power of first-order sideband varies sinusoidally with the phase-shift $\Delta\phi$ for m<0.2.

Considering the attenuation of Kerr medium, the amplitude of the perpendicular and the parallel field components at position z of a Kerr medium are given by

$$A_{\|} = \sqrt{\frac{P_P e^{-\alpha_{Loss} z}}{2}}\cos\left[\pi f_s\left(t - t_{\|}\right)\right]\exp\left(i\phi_{NL}^{'}(z)\right) \tag{2.11}$$

$$A_{\perp} = \sqrt{\frac{P_P e^{-\alpha_{Loss} z}}{2}}\cos\left[\pi f_s\left(t - t_{\perp}\right)\right]\exp\left(i\phi_{NL}^{'}(z)\right) \tag{2.12}$$

where $\phi_{NL}^{'}(z) = 4\gamma P_P\left[\left(1 - e^{-\alpha_{Loss} z}\right)/\alpha_{Loss}\right]\left\{\cos^2\left[\pi f_s\left(t - t_{\|}\right)\right] + \cos^2\left[\pi f_s\left(t - t_{\perp}\right)\right]\right\}/9$, and α_{Loss} is attenuation parameter. Accordingly, Eq. (2.10) turns to be

$$P_{\|,1} = P_{\perp,1} = \left(\frac{1 - e^{-\alpha_{Loss} L_{Kerr}}}{\alpha_{Loss}}\right)^2 \frac{e^{-\alpha_{Loss} L_{Kerr}} \gamma^2 P_P^3}{162}\cos^2(\Delta\phi) \tag{2.13}$$

In the case that the peak powers of the perpendicular and parallel components are different, the superposed sinusoidal phase-modulation induced by Kerr effect becomes

$$\phi_{NL} = \frac{8\gamma L_{Kerr}}{9}\left\{P_{\|}\cos^2\left[\pi f_s\left(t - t_{\|}\right)\right] + P_{\perp}\cos^2\left[\pi f_s\left(t - t_{\perp}\right)\right]\right\} \tag{2.14}$$

where $P_{\|}$ and $P_{\perp}$ are peak powers of the parallel and perpendicular components of combined SMOS. Replacing Eq. (2.14) in Eq. (2.3) and Eq. (2.4) leads to the values of $P_{\|,1}$ and $P_{\perp,1}$ that are given by (see Appendix B)

$$P_{\perp,1} = \frac{P_{\perp}\gamma^2 L^2_{Kerr}\left[P_{\|}^2 + P_{\perp}^2 + 2P_{\|}P_{\perp}\cos\left(2\Delta\phi\right)\right]}{81} \tag{2.15}$$

$$P_{\|,1} = \frac{P_{\|}\gamma^2 L^2_{Kerr}\left[P_{\|}^2 + P_{\perp}^2 + 2P_{\|}P_{\perp}\cos(2\Delta\phi)\right]}{81} \tag{2.16}$$

for $m' = 8\gamma L_{Kerr} g / 9 < 0.2$ with $g = 0.5\sqrt{P_{\|}^2 + P_{\perp}^2 + 2P_{\|}P_{\perp}\cos(2\Delta\phi)}$. For the special case of $P_{\perp} = P_{\|} = P_P / 2$, Eq. (2.15) and Eq. (2.16) turn to Eq. (2.10) as expected.

The minimum value of $P_{\|\perp,1}$ in the case of $P_{\perp} = P_{\|}$ is $\min\{P_{\|\perp,1}\} = 0$ at $\Delta\phi$ =π/2, 3π/2, 5π/2,… as indicated in Eq. (2.10), whereas $\min\{P_{\|\perp,1}\} = P_{\|\perp}\gamma^2 L^2_{Kerr}\left(P_{\|} - P_{\perp}\right)^2 / 81$ in the case of $P_{\perp} \neq P_{\|}$, which is implied by Eq. (2.15) and Eq. (2.16). Essentially, the first-order sideband arises from the existence of sinusoidal phase-modulation ϕ_{NL} that is superposition of phase-modulations ϕ_{SPM} and ϕ_{XPM}. The magnitudes of ϕ_{SPM} and ϕ_{XPM} are respectively proportional to the peak powers of the SMOSs, and determine the magnitude ϕ_{NL_mag} of the sinusoidal phase-modulation ϕ_{NL}. Figure 2.4 shows illustrations of ϕ_{SPM}, ϕ_{XPM} and $\phi_{NL} = \phi_{SPM} + \phi_{XPM}$ in the cases of $P_{\perp} = P_{\|}$ and $P_{\perp} \neq P_{\|}$ at $\Delta\phi$ =π/2. As Fig. 2.4 shows, the magnitudes of ϕ_{SPM} and ϕ_{XPM} are identical in the case of $P_{\perp} = P_{\|}$, and thus ϕ_{SPM} and ϕ_{XPM} compensate each other completely at $\Delta\phi$ =π/2 leading to $\phi_{NL\_mag} = 0$. The vanishing of the sinusoidal phase-modulation ϕ_{NL} leads to the vanishing of the first-order sideband and thus $\min\{P_{\|\perp,1}\} = 0$. In the case of $P_{\perp} \neq P_{\|}$, however, the magnitudes of ϕ_{SPM} and ϕ_{XPM} are different, and consequently residual sinusoidal phase-modulation ϕ_{NL} exists at $\Delta\phi$ =π/2. The existence of residual sinusoidal phase-modulation ϕ_{NL} leads to the existence of first-order sideband and thus $\min\{P_{\|\perp,1}\} \neq 0$.

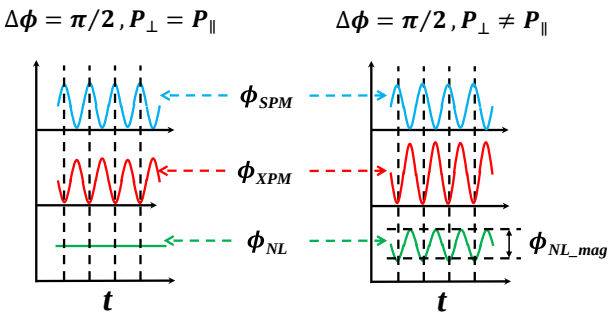

Figure 2.4: Illustrations of ϕ_{SPM}, ϕ_{XPM} and $\phi_{NL}=\phi_{SPM}+\phi_{XPM}$ as a function of time in the cases of $P_\parallel=P_\perp$ and $P_\parallel\neq P_\perp$ at $\Delta\phi=\pi/2$.

2.2 Sideband generation using an electro-optic modulator

2.2.1 Double sidebands generation

Double sidebands (DSB) generation provides a beat signal that is the sinusoidally modulated optical signal required in a Kerr phase-interrogator. Figure 2.5 presents a schematic diagram of a Mach-Zehnder-interferometer based electro-optic modulator (MZI-EOM) for generation of DSB. The electric field E_{in} oscillating at optical frequency ν_0 is split into E_1 and E_2 which respectively propagate in two arms of the MZI with equal magnitude $0.5A$. A piece of Lithium-niobate ($LiNbO_3$) crystal is placed in one arm, along which the optical phase can be modulated by an applied voltage due to Pockels effect. After recombination, interference power P_{out} of E_1 and E_2 at the output of the MZI varies with the phase-shift $\Delta\varphi$ between E_1 and E_2 in the way that $P_{out}=(E_1+E_2)(E_1+E_2)^*=|A|^2\cos^2(0.5\Delta\varphi)$.

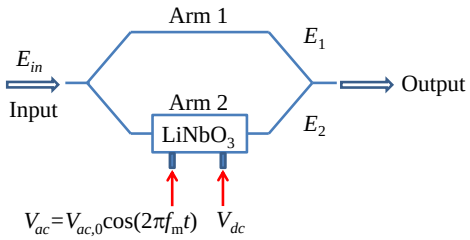

Figure 2.5: Schematic diagram of a MZI-EOM to generate DSB.

When the modulation voltage $V_{ac}=V_{ac,0}\cos\left(2\pi f_m t\right)$ and DC bias voltage V_{dc} are applied to the $LiNbO_3$, refractive index of the $LiNbO_3$ is modulated due to Pockels effect. Modulated refractive index leads to $\Delta\varphi=2\varphi_{ac,0}\cos\left(2\pi f_m t\right)+2\varphi_{dc}$ with $\varphi_{ac,0}=0.5\pi V_{ac,0}/V_\pi$, $\varphi_{dc}=0.5\pi V_{dc}/V_\pi$, f_m being modulation frequency, V_π being half-wave voltage that causes π phase-change. Due to the applied voltages, the interference power at the output of MZI is given by $P_{out}=|A|^2\cos^2\left[\varphi_{ac,0}\cos\left(2\pi f_m t\right)+\varphi_{dc}\right]$.

Employing first series of Bessel function, the interference power is written as

$$P_{out}=|A|^2\left\{\begin{array}{l}\left[J_0\left(\varphi_{ac,0}\right)+2\sum_{k=1}^{\infty}(-1)^k J_{2k}\left(\varphi_{ac,0}\right)\cos\left(4k\pi f_m t\right)\right]\cos\left(\varphi_{dc}\right)\\ -\left[2\sum_{k=1}^{\infty}(-1)^k J_{2k-1}\left(\varphi_{ac,0}\right)\cos\left((4k-2)\pi f_m t\right)\right]\sin\left(\varphi_{dc}\right)\end{array}\right\}^2 \quad (2.17)$$

where "k" is a positive integer. The sinusoidal phase-modulation $\Delta\varphi=2\varphi_{ac,0}\cos\left(2\pi f_m t\right)+2\varphi_{dc}$ gives rise to the formation of distinct sidebands separated by f_m in the output optical spectrum of the MZI, as shown in Fig. 2.6(b). The power of generated n^{th}-order sideband located $(2n-1)\times f_m$ away from central frequency ν_0 in the optical spectrum is determined by the n^{th}-order Bessel function $J_n\left(\varphi_{ac,0}\right)$ as indicated in Eq. (2.17), where $n=2k$ or $2k$-1 represents even- or odd-order Bessel functions. As the value of V_{dc} is selected as $V_{dc}=2mV_\pi$,

$\varphi_{dc} = 0.5\pi V_{dc}/V_{\pi} = m\pi$ with m being an integer is obtained leading to $\left|\cos(\varphi_{dc})\right| = 1$ and $\sin(\varphi_{dc}) = 0$. As a result, Eq. (2.17) reduces to

$$P_{out} = |A|^2 \left[J_0(\varphi_{ac,0}) + 2\sum_{k=1}^{\infty} (-1)^k J_{2k}(\varphi_{ac,0}) \cos(4k\pi f_m t) \right]^2. \tag{2.18}$$

Equation (2.18) reveals that the odd-order sidebands are suppressed and only the even-order sidebands survive, as shown in Fig. 2.6(c). For $V_{ac} < 0.4V_{\pi}/\pi$, $\varphi_{ac,0} = 0.5\pi V_{ac,0}/V_{\pi} < 0.2$ is obtained, and $J_0(\varphi_{ac,0})$ is dominating on the right-hand side of Eq. (2.18). As a result, only the central frequency component at ν_0 contributes to the output power of MZI, and the output power is given by

$$P_{out} = |A|^2 \left| J_0(\varphi_{ac,0}) \right|^2 \tag{2.19}$$

which indicates constant output power.

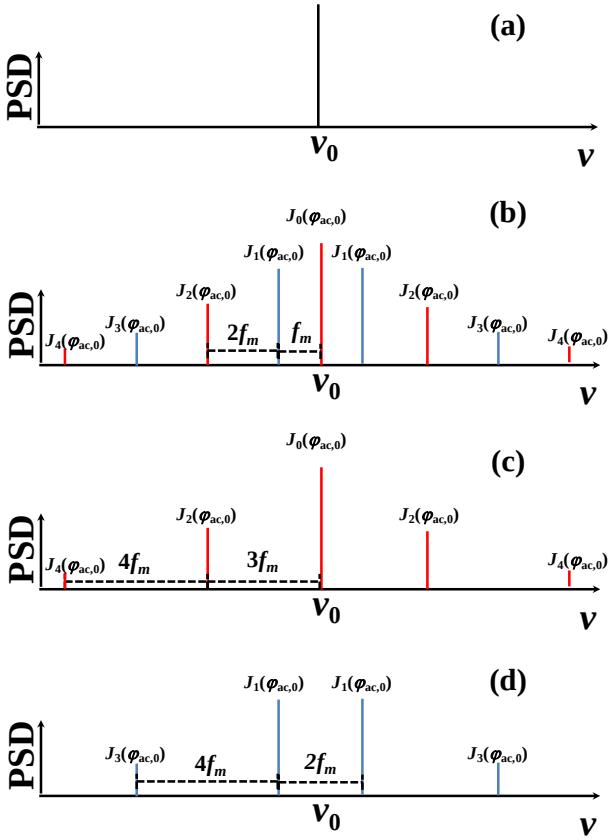

Figure 2.6: Illustration of the optical spectra at the (a) input and (b) output of a MZI, and illustration of output optical spectra when (c) V_{dc}=2mV_{π}. and (d) V_{dc}=(2m+1)V_{π}.

As the value of V_{dc} is selected as $V_{dc}=(2m+1)V_{\pi}$, $\varphi_{dc}=(m+0.5)\pi$ is obtained leading to $\cos(\varphi_{dc})=0$ and $|\sin(\varphi_{dc})|=1$. As a result, Eq. (2.17) becomes

$$P_{out}=|A|^2\left[2\sum_{k=1}^{\infty}(-1)^k J_{2k-1}(\varphi_{ac,0})\cos((4k-2)\pi f_m t)\right]^2. \quad (2.20)$$

In this case, only the odd-order generated sidebands exist in the output optical spectrum, as shown in Fig. 2.6(d). For $V_{ac}<0.4V_{\pi}/\pi$, $\varphi_{ac,0}=0.5\pi V_{ac,0}/V_{\pi}<0.2$ is obtained, and $J_1(\varphi_{ac,0})\cos(2\pi f_m t)$ is dominating on the right-hand side of Eq. (2.20). As a result, only two first-order generated sidebands contribute to the output power P_{out}, and Eq. (2.20) reduces to

$$P_{out}=4|A_0|^2 J_1^2(\varphi_{ac,0})\cos^2(2\pi f_m t) \quad (2.21)$$

which indicates sinusoidal variation in the output power of MZI.

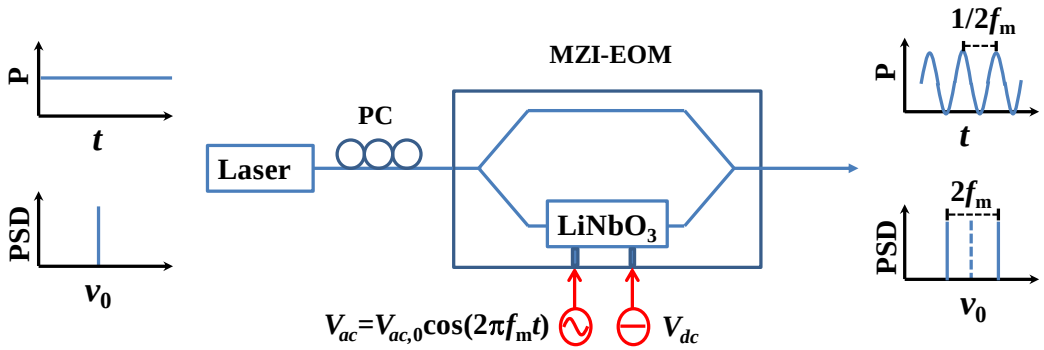

Figure 2.7: Schematic of the experimental setup that is used to generate double sidebands optical signal through a MZI-EOM. P: power; PSD: power spectrum density; PC: polarization controller; MZI-EOM: Mach-Zehnder-interferometer based electro-optic modulator.

Figure 2.7 presents a schematic of the experimental setup that is used to generate the DSB. A continuous light-wave with constant power 5 mw is launched into a MZI-EOM (EO-space) with half-wave voltage $V_{\pi}=1.5$ V. By adjusting the polarization state of the input light-wave through a polarization controller, the optical powers of light-waves in two arms of the MZI-EOM are identical. A sinusoidal

electrical signal with magnitude of $V_{ac,0}$ and oscillation frequency $f_m = 10\,\text{GHz}$ is applied to the MZI-EOM by a sinusoidal electrical signal generator (HP 83752A) to obtain the sinusoidal modulation in the phase-shift between two light-waves in two arms of the MZI-EOM. This sinusoidal phase-modulation leads to distinct sidebands with frequency interval of $2f_m$ in the output optical spectrum of the MZI-EOM. The bias voltage $V_{dc} = 3V_\pi = 4.5\,\text{V}$ is applied to the MZI-EOM to suppress the even order generated sideband in the output optical spectrum of the MZI-EOM. The magnitude of applied sinusoidal electrical signal is chosen $V_{ac,0} = 0.1\,\text{V}$ that is less than $0.4V_\pi / \pi = 0.2$ to ensure that only two first-order generated sidebands dominate in the output optical spectrum of the MZI-EOM. The existence of two dominating sidebands separated by $2f_m$ in the optical spectrum leads to the sinusoidal output power oscillating at frequency $2f_m$, as Eq. (2.21) indicates.

2.2.2 Singe sideband generation

In telecommunication systems, an optical carrier is modulated by a radio frequency (RF) to generate an optical field with the carrier and DSB. When the signal is sent over a fiber, chromatic dispersion of the fiber causes spectral components located at two sidebands to experience different phase shift. If the phase difference between the two optical sidebands at the photo-detector is π, destructive mixing will cancel all power at the RF frequency. Therefore, generation of the optical single-sideband (SSB) is required to eliminate the dispersion effect.

The SSB generation can be achieved using a dual-electrode MZI-EOM, and carrier-suppression can be attained by utilizing a Sagnac interferometer loop with a

dual-electrode MZI-EOM in the loop. Figure 2.8(a) presents the MZI-EOM employed to generate SSB which is a commercial dual-electrode and dual-output traveling wave modulator. Compared with the regular MZI-EOM employed to generate double sidebands output, a dual-electrode MZI-EOM consists of a MZI with two piece of $LiNbO_3$ crystal respectively in two arms of the MZI. Two sinusoidal electrical signals $V_{ac,1} = V_{ac,0}\cos(\omega_m t)$ and $V_{ac,2} = V_{ac,0}\sin(2\pi f_m t)$ are applied to modulate both $LiNbO_3$ with 0.5π phase-shift, where $\omega_m = 2\pi f_m$, and f_m is modulation frequency. Applying two sinusoidal electrical signals with 0.5π phase-shift allows to implement a SSB modulator [11-13]. A DC bias voltage V_{dc} is applied to one $LiNbO_3$ while the other DC terminal is grounded. If the MZI is biased by $V_{dc} = 0.5V_\pi$, the output optical field of the MZI can be written in terms of Bessel functions as [11]

$$E(t) = \frac{A}{2}\left\{\begin{array}{l} \sqrt{2}J_0\left(\frac{\pi V_{ac,0}}{V_\pi}\right)\cos\left(\omega_0 t - \frac{\pi}{4}\right) \\ -2J_1\left(\frac{\pi V_{ac,0}}{V_\pi}\right)\sin\left((\omega_0 - \omega_m)t\right) \\ +\sqrt{2}J_2\left(\frac{\pi V_{ac,0}}{V_\pi}\right)\left[\sin\left((\omega_0 + 2\omega_m)t - \frac{\pi}{4}\right) + \sin\left((\omega_0 - 2\omega_m)t - \frac{\pi}{4}\right)\right] \\ +2J_3\left(\frac{\pi V_{ac,0}}{V_\pi}\right)\sin\left((\omega_0 + 3\omega_m)t\right) \\ +\text{high order terms} \\ \end{array}\right\} \quad (2.22)$$

assuming an input optical field $E_{in}(t) = A\cos(\omega_0 t)$ with ω_0 being the optical carrier frequency, and V_π being a half-wave voltage of the modulator at a given modulation frequency ω_m.

The first term on the right-hand side of Eq. (2.22) is the optical carrier, and the second term is the lower generated first-order sideband, with the upper sideband being

effectively suppressed. The third term is the lower and upper second-order sidebands. The fourth term is the upper third-order sideband, with lower sideband being effectively suppressed. By carefully selecting the magnitude of modulation voltage $V_{ac,0} < V_\pi$, modulation efficiency $\pi V_{ac,0}/V_\pi < \pi$ is attained leading to negligible magnitudes of second-order and higher-order generated sidebands compared with that of the carrier and the first-order generated band. In this case, Eq. (2.22) reduces to

$$E_0(t) = \frac{A}{2}\left\{\sqrt{2}J_0\left(\frac{\pi V_{ac,0}}{V_\pi}\right)\cos\left(\omega_0 t - \frac{\pi}{4}\right) - 2J_1\left(\frac{\pi V_{ac,0}}{V_\pi}\right)\sin\left((\omega_0 - \omega_m)t\right)\right\} \quad (2.23)$$

Equation (2.2.3) indicates that the generation of SSB with the carrier is achieved by modulating the MZI using two sinusoidal electrical signals with 0.5π phase-shift and magnitudes $V_{ac,0} < V_\pi$, and by biasing the MZI with the voltage $V_{dc} = 0.5V_\pi$. To suppress the carrier and obtain a pure single first-order sideband, a Sagnac interferometer loop is employed.

Figure 2.8 (b) presents a schematic of the Sagnac interferometer loop with a dual-electrode MZI-EOM to generate a SSB with suppressed carrier. A linearly polarized optical carrier is launched into one axis of the polarization-maintaining-fiber (PMF) based Sagnac interferometer loop through a nominally 50% polarization-maintaining coupler (PMC). In the loop, optical carrier along with single first-order sideband propagates both clockwise and anticlockwise.

Equation (2.23) is valid for optical waves propagating in both directions in the Sagnac interferometer loop. The difference between the two cases appears in the modulation efficiency $\pi V_{ac,0}/V_\pi$ that is related to the half-wave voltage V_π due to

the nonreciprocity of the MZI-EOM. The modulation half-wave voltage relationship for the clockwise and anticlockwise traveling optical waves can be expressed as [11]

$$V_{\pi,anti} = V_{\pi,clock} \frac{\omega_m \tau}{\sin(\omega_m \tau)} \tag{2.24}$$

where τ is the signal transit time in a traveling-wave MZM.

When the carrier and the sidebands recombine at the 50% coupler, the output optical field amplitude of the carrier is given by [11]

$$E_{carr}(t) = \frac{A}{2}\left[J_0\left(\frac{\pi V_{ac,0}}{V_{\pi,clock}}\right) - J_0\left(\frac{\pi V_{ac,0}}{V_{\pi,anti}}\right)\right]\cos(\omega_0 t) \tag{2.25}$$

where the minus sign on the right-hand side of Eq. (2.25) results from π phase-shift between clockwise and anticlockwise propagating optical carrier induced by the PMC. If the MZI-EOM is not perfectly centered in the loop, there is an additional phase difference introduced between the forward and reverse propagating optical generated sidebands. The output optical field amplitude of the single first-order sideband is given by [11]

$$\begin{aligned} &E_{sideband}(t) \\ &= \frac{A}{\sqrt{2}}\sqrt{\left[J_1\left(\frac{\pi V_{ac,0}}{V_{\pi,forw}}\right) - J_1\left(\frac{\pi V_{ac,0}}{V_{\pi,resv}}\right)\cos(\omega_m T)\right]^2 + \left[J_1\left(\frac{\pi V_{ac,0}}{V_{\pi,resv}}\right)\sin(\omega_m T)\right]^2} \\ &\times\cos\left((\omega_0 - \omega_m)t\right) \end{aligned} \tag{2.26}$$

where T is the difference in the optical signal propagation time from the 50% coupler to the MZM in the clockwise and anticlockwise directions. The comparison between Eq. (2.25) and Eq. (2.26) indicates that the carrier can be eliminated and the single first-order sideband can survive by carefully selecting the value of $V_{ac,0}$ or the power of applied sinusoidal electrical signals that is associated with $V_{ac,0}$. It is

reported that 33 dB optical carrier suppression and 60 dB unwanted signal sideband rejection at 6 GHz modulation frequency is achieved by applying 8dBm modulation sinusoidal electrical signal to a dual-electrode MZI-EOM [11].

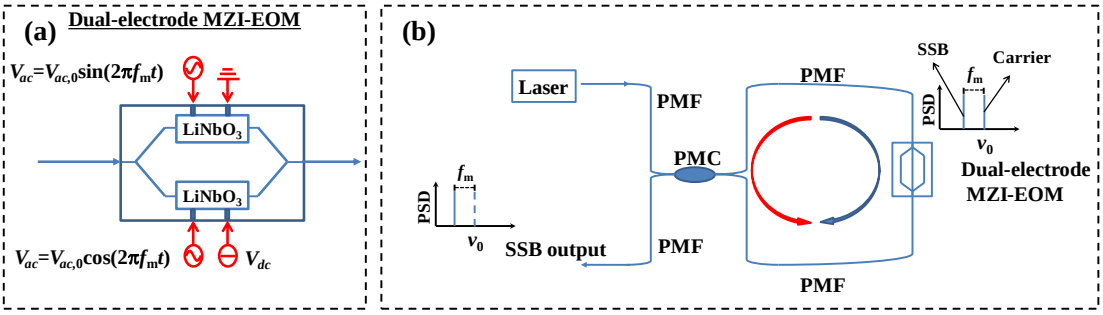

Figure 2.8: Schematic of (a) a dual-electrode MZI-EOM and (b) a Sagnac interferometer loop to implement SSB generation with carrier-suppression. MZI-EOM: Mach-Zehnder-interferometer based electro-optic modulator; SSB: single sideband; PSD: power spectrum density; PMF: polarization-maintaining fiber; PMC: polarization-maintaining controller.

3 Vector analysis of nonlinear interaction between two sinusoidally modulated optical signals in Kerr phase-interrogator

Birefringence of Kerr medium plays important role in the nonlinear-interaction process, and affects the operation of Kerr phase-interrogator. For the Kerr medium comprised of an optical fiber, the birefringence is randomly varying along the Kerr medium leading to random variation in the states-of-polarization (SOP) of two sinusoidally-modulated optical signals (SMOS) that propagate in the Kerr medium. The resulting SOP-variation affects the nonlinear sinusoidal phase-modulation, and consequently affects the generation of first-order sidebands. To account for the impact of birefringence-induced SOP-variation on the generation of first-order sidebands, vector analysis on the nonlinear interaction between two SOMSs is required.

Vector theories of XPM and four-wave mixing have been studied in [14-16], where the nonlinear interaction between continuous light-waves or solitons with arbitrary SOPs is analyzed. However, these studies do not go deep into the nonlinear interaction between orthogonally polarized SMOSs as is the case in the Kerr phase-interrogator. Nonetheless, these studies provide theoretical foundation for the vector analysis of the nonlinear interaction occurring in the Kerr phase-interrogator.

Light-waves that operate at identical wavelengths with identical SOPs guarantee nonlinear interaction with maximum efficiency, and utilization of these light-waves

could improve the measurement signal-to-noise ratio of optical devices that take advantage of nonlinear interaction such as the Kerr phase-interrogator. However, interference among these light-waves occurs along with the nonlinear interaction, and the phase-noise of the light sources is introduced through the interference, which perturbs the nonlinear interaction. The impact of interference on the nonlinear interaction has not been studied.

In this chapter, the phase-modulations generated in the nonlinear interaction between two orthogonally-polarized or co-polarized SMOSs in a Kerr medium with randomly-varying low birefringence is analyzed using two vector-formed nonlinear Schrodinger equations, and the resulting generation of first-order sidebands is analyzed. Experiments are performed using an optical fiber with random birefringence as Kerr medium in the Kerr phase-interrogator, and the results confirm the predictions of the theoretical analysis. This study supplements the analysis of the nonlinear interaction between two SMOSs by considering the birefringence-induced randomly-varying SOPs of the SOMSs, and is essential for understanding the dependence of the operation of a Kerr phase-interrogator on the SOPs of the SOMSs.

3.1 Vector analysis of nonlinear interaction between two orthogonally polarized SMOSs

Electric fields of two SMOSs with power-oscillation frequency f_s are given by

$$E_j = \left| A_j \right\rangle e^{i\left(2\pi\nu_j t - \beta_j z_j - \phi_{j0}\right)} \tag{3.1}$$

where j=1,2 refer to two SMOSs, β_j is propagation constant, ϕ_{j0} is initial phase,

and ν_j is optical frequency. $\left|A_j\right\rangle$ is two-dimensional column vector representing the two components of the amplitude of E_j in the x-y plane such that $\left\langle A_j \middle| A_j \right\rangle = \left|A_j\right|^2 = 0.5P_P \cos^2\left[\pi f_s\left(t-t_j\right)\right]$ is power of E_j with $\left\langle A_j\right|$ being Hermitian conjugate of $\left|A_j\right\rangle$, and P_P being total peak power of two SMOSs. In a Kerr medium, two SMOSs undergo nonlinear interaction and the evolutions of $\left|A_1\right\rangle$ and $\left|A_2\right\rangle$ are governed by the following vector-formed nonlinear Schrodinger equations [14-17]

$$\frac{d}{dz}\left|A_j\right\rangle = \frac{i\gamma}{3}\begin{bmatrix} 3\left\langle A_j \middle| A_j\right\rangle + 2\left\langle A_{3-j} \middle| A_{3-j}\right\rangle \\ -s_3\left(A_j\right)\sigma_3\left|A_j\right|^2 + 4\left|A_{3-j}\right\rangle\left\langle A_{3-j}\right| - 2s_3\left(A_{3-j}\right)\sigma_3\left|A_{3-j}\right|^2 \end{bmatrix}\left|A_j\right\rangle \quad (3.2)$$

where γ is the waveguide nonlinearity, $s_3\left(A_j\right) = \langle A_j \,|\, \sigma_3 \left|A_j\right\rangle / \left|A_j\right|^2$ is normalized Stokes parameter, and $\sigma_3 = \begin{bmatrix} 0 & -i \\ i & 0 \end{bmatrix}$ is Pauli spin matrice [18].

In the case that $\left|A_1\right\rangle$ and $\left|A_2\right\rangle$ are orthogonally polarized, $\left\langle A_{3-j} \middle| A_j\right\rangle = 0$ and $s_3\left(A_j\right) = -s_3\left(A_{3-j}\right) = s_3$ are attained, and Eq. (3.2) becomes

$$\frac{d}{dz}\left|A_j\right\rangle = \frac{i\gamma}{3}\left[\left(3\left|A_j\right|^2 + 2\left|A_{3-j}\right|^2\right) - s_3\sigma_3\left|A_j\right|^2 + 2s_3\sigma_3\left|A_{3-j}\right|^2\right]\left|A_j\right\rangle. \quad (3.3)$$

Random birefringence of the Kerr medium makes the Stokes parameters of $\left|A_j\right\rangle$ and $\left|A_{3-j}\right\rangle$ randomly walk on the Poincare sphere. Therefore, $s_3\left(A_j\right)\sigma_3\left|A_j\right\rangle$ in Eq. (3.3) requires the average and turns to be $\left|A_j\right\rangle / 3$ [1, 18]. Integrating $\left|A_j\right\rangle$ over *z* and using $\left|A_j\left(z\right)\right|^2 = 0.5P_P \cos^2\left[\pi f_s\left(t-t_j\right)\right]$ gives a solution $\left|A_j\left(L_{Kerr}\right)\right\rangle = \left|A_j\left(0\right)\right\rangle \exp\left(i\phi_{NL}\right)$, where

$$\phi_{NL,j} = \frac{4}{9}L_{Kerr}\gamma P_P\left\{\cos^2\left[\pi f_s\left(t-t_j\right)\right] + \cos^2\left[\pi f_s\left(t-t_{3-j}\right)\right]\right\} \quad (3.4)$$

with L_{Kerr} being the length of the Kerr medium.

The phase-modulations $\phi_{NL,j}$ in Eq. (3.4) is comprised of

$\phi_{SPM,j} = 4/9 L_{Kerr}\gamma P_P \cos^2\left[\pi f_s\left(t-t_j\right)\right]$ induced by self-phase modulation (SPM) and $\phi_{XPM,j} = 4/9 L_{Kerr}\gamma P_P \cos^2\left[\pi f_s\left(t-t_{3-j}\right)\right]$ induced by cross-phase modulation (XPM). The combination of $\phi_{SPM,j}$ and $\phi_{XPM,j}$ leads to the formation of distinct sidebands P_k with k=1,2,... at $\nu_j \pm (k+0.5) f_s$ in the optical spectrum of $\left|A_j\right\rangle$. For $4\gamma L_{Kerr} P_P / 9 < 0.4$, the power of first-order side band P_1 is approximately given by

$$P_1 = P_{1,0}\cos^2\left(\pi f_s t_d\right) \tag{3.5}$$

where $t_d = t_2 - t_1$ is the group delay of the SMOSs.

3.2 Vector analysis of nonlinear interaction between two co-polarized SMOSs

3.2.1 Different carrier-wavelengths

In the case that $\left|A_1\right\rangle$ and $\left|A_2\right\rangle$ are co-polarized and are carried by lasers with different wavelengths, $\left|A_{3-j}\right\rangle\left\langle A_{3-j}\right|\left|A_j\right\rangle = \left|A_{3-j}\right|^2\left|A_j\right\rangle$ and $s_3\left(A_j\right) = s_3\left(A_{3-j}\right) = s_3$ are attained, and Eq. (3.2) becomes

$$\frac{d}{dz}\left|A_j\right\rangle = \frac{i\gamma}{3}\left[3\left|A_j\right|^2 + 6\left|A_{3-j}\right|^2 - s_3\sigma_3\left|A_j\right|^2 - 2s_3\sigma_3\left|A_{3-j}\right|^2\right]\left|A_j\right\rangle. \tag{3.6}$$

Averaging the last two terms on the right-hand side in term of SOP results in $s_3\left(A_j\right)\sigma_3\left|A_j\right\rangle \to \left|A_j\right\rangle/3$. Integrating $\left|A_j\right\rangle$ over z in Eq. (3.6) and using $\left|A_j(z)\right|^2 = 0.5P_P\cos^2\left[\pi f_s\left(t-t_j\right)\right]$ gives a solution $\left|A_j\left(L_{Kerr}\right)\right\rangle = \left|A_j(0)\right\rangle\exp\left(i\phi_{NL}\right)$, where

$$\phi_{NL,j} = \frac{4}{9}L_{Kerr}\gamma P_P\left\{\cos^2\left[\pi f_s\left(t-t_j\right)\right] + 2\cos^2\left[\pi f_s\left(t-t_{3-j}\right)\right]\right\}. \tag{3.7}$$

$4/9 L_{Kerr}\gamma P_P \cos^2\left[\pi f_s\left(t-t_j\right)\right]$ and $8/9 L_{Kerr}\gamma P_P \cos^2\left[\pi f_s\left(t-t_{3-j}\right)\right]$ in $\phi_{NL,j}$ respectively correspond to SPM and XPM. The power of first-order sideband that arises from $\phi_{NL,j}$ is given by

$$P_1 = \frac{P_{1,0}}{4}\left[5 + 4\cos\left(2\pi f_s t_d\right)\right] \tag{3.8}$$

3.2.2 Identical carrier-wavelengths

In the analysis so far, the evolutions of $|A_1\rangle$ and $|A_2\rangle$ in the Kerr medium are distinguishable due to the difference either in carrier-wavelengths or in SOPs of $|A_1\rangle$ and $|A_2\rangle$. In the case of two co-polarized SMOSs carried by identical wavelengths, however, discrimination of evolutions of $|A_1\rangle$ and $|A_2\rangle$ becomes difficult. Therefore, the total electric field $E_{tot} = E_1 + E_2$ is involved in the analysis. Undergoing SPM in the Kerr medium, the amplitude of E_{tot} at the output of Kerr medium is given by $|A_{tot}(L_{Kerr})\rangle = |A_{tot}(0)\rangle \exp\left(i\phi_{NL,tot}\right)$, where $\phi_{NL,tot} = 8/9\gamma L_{Kerr}|A_{tot}|^2$. The factor of $8/9$ results from random-birefringence-induced mode-coupling between two polarization components of $|A_{tot}\rangle$ oriented along the principal axes of Kerr medium [1]. Using $|A_{tot}|^2 = |A_1|^2 + |A_2|^2 + 2|A_1||A_2|\cos(\Delta\phi_0)$ and $|A_j(z)|^2 = 0.5P_P\cos^2\left[\pi f_s\left(t - t_j\right)\right]$ in $\phi_{NL,tot}$ leads to

$$\phi_{NL,tot} = \frac{4}{9}P_P L_{Kerr}\gamma\left[1 + \cos\left(\pi f_s t_d\right)\cos\left(\Delta\phi_0\right)\right] + m_{ac}\cos\left[2\pi f_s\left(t - \frac{t_j + t_{3-j}}{2}\right)\right] \tag{3.9}$$

where $\Delta\phi_0 = \phi_{20} - \phi_{10} + \beta\Delta z$, $\Delta z = z_2 - z_1$, $\beta = \beta_1 = \beta_2$ and $m_{ac} = 4/9P_P L_{Kerr}\gamma\left[\cos\left(\pi f_s t_d\right) + \cos\left(\Delta\phi_0\right)\right]$. The term of $2|A_1||A_2|\cos\left(\Delta\phi_0\right)$ in $|A_{tot}|^2$ arises from the interference between E_1 and E_2. The sinusoidally time-varying term $m_{ac}\cos\left[2\pi f_s\left(t - 0.5\left(t_j + t_{3-j}\right)\right)\right]$ in $\phi_{NL,tot}$ gives birth to the distinct sidebands in the optical spectrum, and the power of first-order sideband is given by

$$P_1 = P_{1,0}\left[\cos\left(\pi f_s t_d\right) + \cos\left(\Delta\phi_0\right)\right]^2 . \quad (3.10)$$

3.3 Analysis of sinusoidal power-variation of first-order sideband with the phase-shift of SMOSs

In the Kerr medium, the generated first-order sideband in the optical spectrum arises from the existence of sinusoidal phase-modulation in $\phi_{NL,j}$, and the value of P_1 is determined by the magnitude of this sinusoidal phase-modulation. Because $\phi_{NL,j}$ is the superposition of sinusoidal phase-modulations $\phi_{\mathrm{SPM},j}$ and $\phi_{\mathrm{XPM},j}$, the magnitude of the sinusoidal phase-modulation in $\phi_{NL,j}$ is determined by the phase-shift between the sinusoidal phase-modulations $\phi_{\mathrm{SPM},j}$ and $\phi_{\mathrm{XPM},j}$, which is $\left|2\pi f_s\left(t-t_j\right)-2\pi f_s\left(t-t_{3-j}\right)\right| = 2\pi f_s t_d$. As a result, the value of P_1 is governed by the phase-shift $2\pi f_s t_d$.

Figure 3.1 shows $\phi_{NL,j}$, $\phi_{\mathrm{SPM},j}$ and $\phi_{\mathrm{XPM},j}$ in the case of two orthogonally polarized SMOSs. In this case, the magnitude of $\phi_{\mathrm{XPM},j}$ is identical to that of $\phi_{\mathrm{SPM},j}$ as Eq. (3.4) indicates. When sinusoidal phase-modulations $\phi_{\mathrm{SPM},j}$ and $\phi_{\mathrm{XPM},j}$ are in-phase, that is $2\pi f_s t_d = 2n\pi$ with *n* being integer, the sinusoidal phase-modulation in $\phi_{NL,j}$ is enhanced and the magnitude of this sinusoidal modulation reaches maximum leading to the maximum value of P_1. In comparison, when $2\pi f_s t_d = 2n\pi + \pi$, sinusoidal phase-modulations $\phi_{\mathrm{SPM},j}$ and $\phi_{\mathrm{XPM},j}$ are out-of-phase, and the sinusoidal modulation in $\phi_{NL,j}$ is compensated completely. The vanishing of the sinusoidal modulation in $\phi_{NL,j}$ results in the vanishing of first-order sideband,

and thus the value of P_1 reduces to zero as Eq. (3.5) indicates.

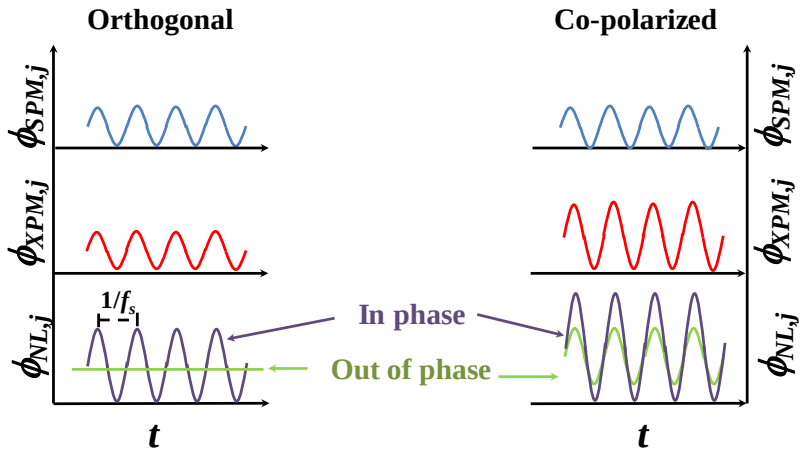

Figure 3.1: Illustrations of nonlinear phase-modulations in the cases of orthogonally polarized and co-polarized SMOSs.

Compared with P_1 in the case of orthogonally polarized SMOSs, P_1 never reduces to zero in the case of co-polarized SMOSs carried by different wavelengths, as Eq. (3.8) indicates. Figure 3.1 also shows $\phi_{NL,j}$, $\phi_{\mathrm{SPM},j}$ and $\phi_{\mathrm{XPM},j}$ in the case of co-polarized SMOSs carried by different wavelengths. Because the magnitude of $\phi_{\mathrm{XPM},j}$ is twice that of $\phi_{\mathrm{SPM},j}$ as indicated in Eq. (3.7), the sinusoidal modulation in $\phi_{NL,j}$ still exists even when the sinusoidal phase-modulations $\phi_{\mathrm{SPM},j}$ and $\phi_{\mathrm{XPM},j}$ are out-of-phase, and the residual sinusoidal modulation in $\phi_{NL,j}$ results in $P_1 \neq 0$.

In the case of co-polarized SMOSs carried by identical carrier-wavelengths, the phase noise of light sources of the co-polarized SOMSs is involved in $\phi_{20}-\phi_{10}$ due to the interference between E_1 and E_2, which leads to the fluctuation in the total power $|A_{tot}|^2$. Because $\phi_{NL,tot}$ results from SPM and the value of $\phi_{NL,tot}$ is proportional to $|A_{tot}|^2$, the fluctuation in $|A_{tot}|^2$ leads to the fluctuation in $\phi_{NL,tot}$. Since the first-order sideband arises from $\phi_{NL,tot}$, the phase noised induced fluctuation in $\phi_{NL,tot}$ perturbs the generation of first-order sideband as indicated in Eq. (3.10).

3.4 Experimental verification

Figure 3.2(a) shows a schematic of a Kerr phase-interrogator employed to demonstrate sinusoidal variation of P_1 in the case of orthogonally polarized SMOSs carried by different carrier-wavelengths. Two continuous-wave lasers (Agilent 81980A) respectively operating at wavelengths of λ_1 =1551.70 nm and λ_2 =1552.36 nm are amplitude-modulated using a sinusoidal electrical signal generator (HP 83752A) with modulation frequency f_m =10 GHz to obtain two SMOSs with a power oscillation frequency of $f_s = 2 f_m$. Two SMOSs are combined by a polarization beam combiner (PBC) to obtain two orthogonally polarized SMOSs. A variable delay line is placed in the delay path to vary group-delay difference t_d, and two polarization controllers, PC1 and PC2, ensure the peak powers of the orthogonal components of the combined signal are maximum and equal. After amplification, the combined signal with total peak power P_P =20mW is launched into a Kerr medium comprised of a dispersion-shifted fiber (DSF) with length of 2 km and waveguide nonlinearity of γ =2.28 W^{-1}/km. Because zero-dispersion wavelength of the DSF locates at 1552 nm, the dispersion-impact of Kerr medium on the sinusoidal variation of P_1 is neglected. The first-order sideband generated in the Kerr medium is extracted by a band-pass filter (TeraXion TFC) with a 3 dB bandwidth of 3 GHz, and a power-meter (Agilent/HP 81536A) is used to measure P_1 as t_d is varied. Figure 3.3 presents the normalized value of measured P_1 as a function of t_d showing sinusoidal variation of P_1 with period of 50 ps. In addition, the minimum power value P_1^{min} is zero. Using f_s=20 GHz and t_d=25 ps in Eq. (3.5) gives $\pi f_s t_d = 0.5\pi$ leading to $P_1^{min} = 0$ in

agreement with the experimental result.

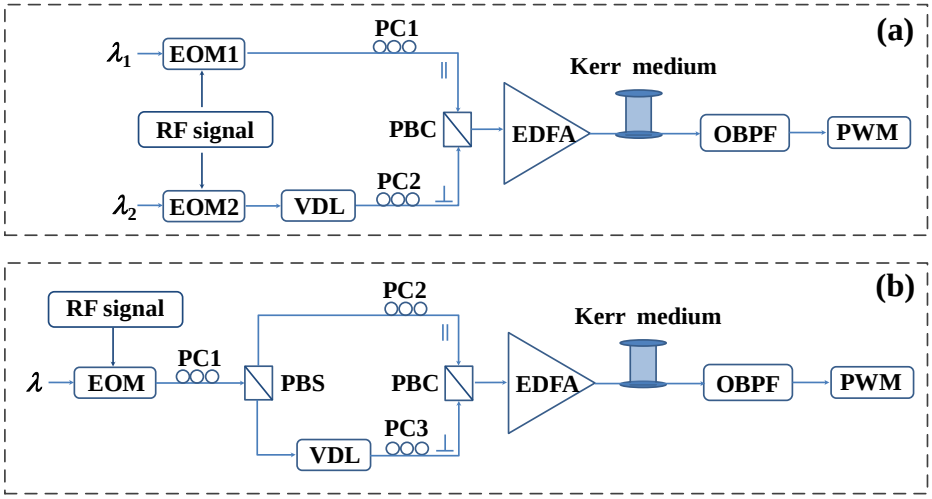

Figure 3.2: Schematic of a Kerr phase-interrogator with two orthogonally polarized SMOSs carried by (a) different wavelengths and (b) identical wavelengths. EOM: electro-optic modulator; RF: radio frequency; PC: polarization controller; PBS: polarization beam splitter; VDL: variable delay line; PBC: polarization beam combiner; EDFA: erbium-doped fiber amplifier; OBPF: optical band-pass filter; PWM: power meter.

The Kerr phase interrogator shown in Fig. 3.2(a) is modified as presented in Fig. 3.2(b) to demonstrate sinusoidal variation of P_1 in the case of orthogonally polarized SMOSs carried by identical wavelengths. A SMOS oscillating at a frequency f_s =20 GHz and carried by wavelength λ =1552 nm is split into orthogonally polarized components by a polarization beam splitter (PBS). The orthogonally polarized components are recombined by a PBC, and their powers after recombination are ensured maximum and identical by PC1 and PC2. As t_d is varied from 0 to 120 ps, P_1 is recorded and the normalized values of measured P_1 as a function of t_d are presented in Fig. 3.3 showing sinusoidal variation with $P_1^{min} = 0$ in agreement with theoretical values calculated using Eq. (3.5).

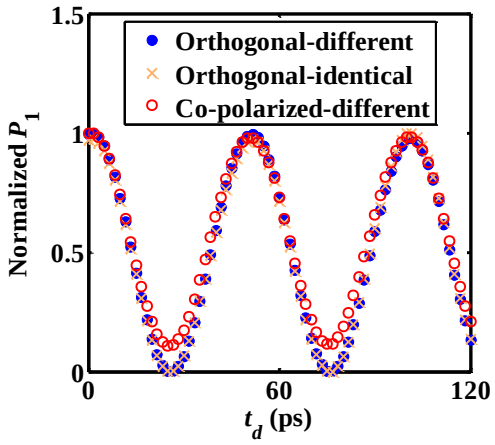

Figure 3.3: Measured values of P_1 as a function of t_d in the cases of orthogonally polarized SMOSs carried by different or identical wavelengths, and co-polarized SMOSs carried by different wavelengths.

The PBC in Fig. 3.2(a) is replaced with a 50/50 fiber coupler followed by a polarizer to attain co-polarized SMOSs with equal peak-powers and different carrier-wavelengths. As t_d is varied, the value of P_1 is recorded by a power-meter, and the normalized values of measured P_1 as a function of t_d are also presented in Fig. 3.3. The minimum value of the normalized P_1 shown in Fig. 3.3 is 0.1082 indicating the extinction ratio of $P_1^{max} / P_1^{min} = 1/0.1082 = 9.24$, where P_1^{max} is the maximum value of measured P_1. Using Eq. (3.8) gives $P_1^{max} = 9P_{1,0}/4$ for $2\pi f_s t_d = 2n\pi$ and $P_1^{min} = P_{1,0}/4$ for $2\pi f_s t_d = 2(n+1)\pi$ leading to the theoretical value of $P_1^{max} / P_1^{min} = 9$ in close agreement with the experimental value.

The PBS in Fig. 3.2(b) is replaced with a 50/50 fiber coupler, and the PBC is replaced with a 50/50 fiber coupler followed by a polarizer to attain co-polarized SMOSs with equal peak-powers and identical carrier-wavelengths. As t_d is varied, P_1 is recorded and is presented in Fig. 3.4. As indicated by Eq. (3.10), dramatically fluctuation on the sinusoidal variation of P_1 with t_d is shown in Fig.3.4, which is

induced by the phase noise of the laser through the interference between co-polarized E_1 and E_2.

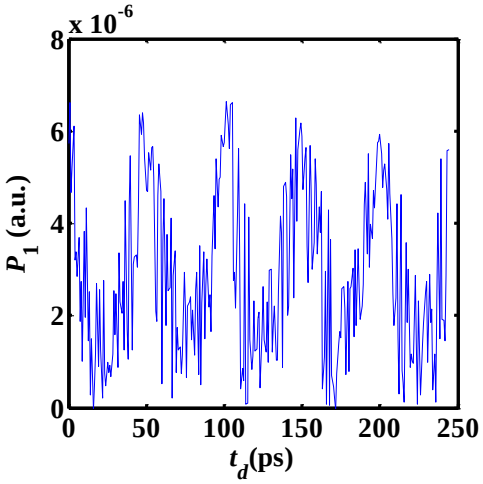

Figure 3.4: Measured values of P_1 as a function of t_d in the case of co-polarized SMOSs carried by identical wavelengths.

The sinusoidal variation $P_1(t_d)$ accounts for the core functionality of the Kerr phase-interrogator for sensing applications. Utilization of two co-polarized SMOSs carried by different wavelengths reduces the extinction ratio of the sinusoidal variation $P_1(t_d)$ leading to reduced sensitivity in the Kerr phase-interrogator based phase-shift measurements. Furthermore, when two co-polarized SMOSs carried by identical wavelengths are used in the Kerr phase-interrogator, $P_1(t_d)$ is dramatically perturbed by the phase noise of light source leading to reduction in the accuracy of the phase-shift measurement. Therefore, the optimal phase-shift measurement based on Kerr phase-interrogator requires utilization of two orthogonally polarized SOMSs carried by either identical or different wavelengths.

3.5 Conclusion

Vector analysis of nonlinear interaction between two orthogonally-polarized or

co-polarized SMOSs with identical or different carrier-wavelengths in the Kerr medium with randomly varying birefringence is performed. The analysis reveals that for orthogonally polarized SMOSs, the nonlinear phase induced by XPM is identical to the nonlinear phase induced by SPM. However, for co-polarized signals, the nonlinear phase induced by XPM is doubled that induced by SPM. Based on the vector analysis, sinusoidal variation of P_1 with t_d is analyzed. Predictions of the theoretical analysis are experimentally verified, and experimental results show that $P_1^{min} = 0$ and $P_1^{max} / P_1^{min} = \infty$ in the cases of orthogonally polarized SMOSs carried by different or identical wavelengths, whereas $P_1^{max} / P_1^{min} = 9$ in the case of co-polarized SMOSs carried by different wavelengths. In addition, sinusoidal variation of P_1 is dramatically perturbed by the phase noise of the laser sources when two co-polarized SMOSs are carried by identical wavelengths. This study provides insight into the dependence of operation of the Kerr phase-interrogator on the SOPs of SMOSs.

4 Chromatic-dispersion impact on the generation of first-order sidebands using theory of four-wave mixing

The sinusoidal dependence is found in power of first-order sideband P_1 versus phase-shift between two orthogonally-polarized sinusoidally-modulated optical signals (SMOS). Hence, a Kerr phase-interrogator can measure parameters that change the phase-shift between two orthogonally-polarized SMOSs by measurement of P_1, and is a promising novel approach for monitoring and sensing applications as will be presented in chapter 5-8. Because chromatic dispersion (CD) affects the efficiency of the nonlinear process, CD of the Kerr medium that is used in a Kerr phase-interrogator has impact on the generation of first-order sidebands leading to deviation from the expected phase-shift measurement.

The phase-modulation-based model demonstrated in chapter 2 is intuitive and allows for conceptual understanding of the operation of the Kerr phase-interrogator in terms of superposition of the sinusoidal phase-modulations of two orthogonally polarized SMOSs. Unfortunately, the phase-modulation-based model does not account for the impact of CD of the Kerr medium on the operation of the Kerr phase-interrogator. An analytical model that includes the effect of CD of the Kerr medium will provide insight into the impact of CD on the operation of the Kerr phase-interrogator as a sensing and signal-processing device, and will simplify the design of the Kerr phase interrogator to achieve optimal performance. Such analytical

model can be obtained by utilization of the theory of four-wave mixing (FWM) to study the nonlinear interaction between two orthogonally-polarized SMOSs.

There have been relevant studies that investigate the impact of CD on the nonlinear interaction between co-polarized SMOSs for wavelength-division multiplexing systems [19, 20]. Unfortunately, these studies apply only to co-polarized SMOSs, and there has not been any study on the interaction between two orthogonally polarized SMOSs in a despersive Kerr medium as is the case in a Kerr phase-interrogator. Furthermore, these studies only account for the CD-induced group-velocity difference between SMOSs that are centered at different carrier wavelengths. In practice, the optical spectrum of each SMOS consists of two frequency-components, and CD in the Kerr medium induces phase-mismatch among these frequency-components reducing the efficiency of the nonlinear interaction [21, 22].

In this chapter, the impact of CD on the generation of first-order sidebands that arise from nonlinear interaction between two orthogonally-polarized SMOSs with identical or different carrier-wavelengths is investigated analytically and experimentally. Analytical solution of P_1 accounting for CD of a Kerr medium is obtained using theory of FWM. Experimental verification of the analytical solution is achieved by comparison between the measured and the calculated values of P_1 at the output of the Kerr phase-interrogator that utilizes a dispersive fiber as Kerr medium. This study is essential for acquiring insight into the operation of a Kerr phase-interrogator when the Kerr medium is dispersive, as well as for optimal

performance in sensing and signal-processing devices based on a Kerr phase-interrogator.

4.1 Analysis of chromatic dispersion impact

The electric field $E_{j=1,2}$ for each of the orthogonally-polarized SMOSs consists of two distinct spectral components $E_j^{\pm}$ located at $\omega_j \pm \omega_m$ such that $E_{j=1,2} = E_j^{+} + E_j^{-}$, as illustrated in Fig. 4.1, where $\omega_m = 2\pi f_m$, $f_m = 0.5 f_s$ is the field modulation frequency, and f_s is the power oscillation frequency. The orthogonally-polarized SMOSs with identical peak powers are launched into a dispersive optical fiber with a length L_{Kerr}. Propagation of the fields E_1 and E_2 in the optical fiber induces third-order nonlinear polarization $P_{NL}^{(3)}$ which leads to the generation of new n^{th}-order spectral components $E_j^{(2n+1)\pm}$ at angular frequencies $\omega_j \pm (2n+1)\omega_m$ with n being an integer and $n \geq 0$. The zeroth-order spectral components with n=0 are located at $\omega_j \pm \omega_m$ and correspond to the spectral components of the SMOS such that $E_j^{\pm} = E_j^{(1)\pm}$.

After generation of the new spectral components, the electric field of the signal is given by $E_j = \sum_n E_j^{(2n+1)\pm}$. Assuming the amplitude of generated sideband $E_j^{(2n+1)\pm}$ is much smaller than that of $E_j^{\pm}$, the signal field becomes $E_j = E_j^{+} + E_j^{-}$ and the third-order nonlinear polarization $P_{NL}^{(3)}$ is given by [23]

$$P_{NL,j}^{(3)}\Big|_{\omega_j \pm (2n+1)\omega_m} = \frac{8}{9}\frac{3\varepsilon_0 \chi_{1111}^{(3)}}{4}\left(E_j^{\pm} E_j^{\mp *} + E_{3-j}^{\pm} E_{3-j}^{\mp *}\right) E_j^{(2n-1)\pm} \tag{4.1}$$

where $\chi_{1111}^{(3)}$ is one component of third-order susceptibility. The factor 8/9 in Eq. (4.1)

results from polarization mode-coupling and polarization-state average of the orthogonally polarized electric fields E_1 and E_2 due to random birefringence in the optical fiber [24-26]. For *n*=1, Eq. (4.1) reduces to

$$P_{NL,j}^{(3)}\Big|_{\omega_j \pm 3\omega_m} = \frac{8}{9}\frac{3\varepsilon_0 \chi_{1111}^{(3)}}{4}\left(E_j^{\pm}E_j^{\mp *} + E_{3-j}^{\pm}E_{3-j}^{\mp *}\right)E_j^{\pm} \quad . \tag{4.2}$$

where the FWM terms $E_j^{\pm}E_j^{\mp *}E_j^{\pm}$ and $E_{3-j}^{\pm}E_{3-j}^{\mp *}E_j^{\pm}$ generate first-order sidebands $E_j^{(3)\pm}$ at angular frequencies $\omega_j \pm 3\omega_m$.

Propagation of the electric field component $E_j^{(3)\pm}$ at $\omega_j^{(3)\pm} = \omega_j \pm 3\omega_m$ in a fiber is governed by the wave equation [1]

$$\frac{\partial^2 E_j^{(3)\pm}}{\partial z^2} - \frac{n^2}{c^2}\frac{\partial^2 E_j^{(3)\pm}}{\partial t^2} = \mu_0 \frac{\partial^2 P_{NL,j}^{(3)}\Big|_{\omega_j \pm 3\omega_m}}{\partial t^2} \tag{4.3}$$

where *n* is the refractive-index of Kerr medium, *c* is speed of light in vacuum and μ_0 is permeability of free space. Using $E_j^{(3)\pm}(z,t) = FA_j^{(3)\pm}(z)\exp\left[i\left(\omega_j^{(3)\pm}t - \beta_j^{(3)\pm}z\right)\right]$ with $1/F^2$ being the effective mode area, $\beta_j^{(3)\pm}$ being the propagation constant of $E_j^{(3)\pm}$, and $A_j^{(3)\pm}(z)$ being the electric field amplitude at $\omega_j^{(3)+}$ [1], the left side of Eq. (4.3) becomes

$$F\left[-2i\beta_j^{(3)\pm}\frac{\partial}{\partial z}A_j^{(3)\pm}(z) + \left(\left(\frac{n}{c}\omega_j^{(3)\pm}\right)^2 - \left(\beta_j^{(3)\pm}\right)^2\right)A_j^{(3)\pm}(z)\right]e^{i\left(\omega_j^{(3)\pm}t - \beta_j^{(3)\pm}z\right)}, \tag{4.4}$$

where $A_1^{(3)\pm}(z)$ is assumed to have a slow varying envelop such that $\partial^2 A_j^{(3)\pm}/\partial z^2$ is neglected. Using $E_j^{\pm}(z,t) = FA_j^{\pm}(z)\exp\left[i\left(\omega_j^{\pm}t - \beta_j^{\pm}z - \phi_j^{\pm}\right)\right]$ with $\beta_j^{\pm}$ and $\phi_j^{\pm}$ being the propagation constant and the initial phase of the electric field $E_j^{\pm}$, respectively, and neglecting the loss in the Kerr medium such that $\left|A_j^{\pm}(z)\right| = \left|A_{3-j}^{\pm}(z)\right| = \sqrt{P_0}$, Eq. (4.2) becomes

$$P_{NL,j}^{(3)}\Big|_{\omega_j\pm3\omega_m}=\frac{8}{9}\frac{3\varepsilon_0\chi_{1111}^{(3)}}{4}F^3P_0^{1.5}\times\left\{e^{i\left[\left(\beta_j^{\mp}z+\phi_j^{\mp}\right)-\left(\beta_j^{\pm}z+\phi_j^{\pm}\right)\right]}+e^{i\left[\left(\beta_{3-j}^{\mp}z+\phi_{3-j}^{\mp}\right)-\left(\beta_{3-j}^{\pm}z+\phi_{3-j}^{\pm}\right)\right]}\right\}e^{i\left[\left(\omega_j\pm3\omega_m\right)t-\beta_j^{\pm}z-\phi_j^{\pm}\right]}. \quad (4.5)$$

where P_0 is power of $E_j^{\pm}$. Replacing Eq. (4.4) and Eq. (4.5) in Eq. (4.3), using $\left(\beta_j^{(3)\pm}\right)^2=\left(n\omega_j^{(3)\pm}/c\right)^2$, and neglecting imaginary part of $\chi_{1111}^{(3)}$, leads to

$$\frac{\partial A_j^{(3)\pm}(z)}{\partial z}=-i\frac{8}{9}\gamma P_0^{1.5}\left\{\sum_{j=1}^{2}e^{i\left[\left(\beta_j^{\mp}-\beta_j^{\pm}\right)z+\left(\phi_j^{\mp}-\phi_j^{\pm}\right)\right]}\right\}e^{i\left(\beta_j^{(3)\pm}z-\beta_j^{\pm}z-\phi_j^{\pm}\right)} \quad (4.6)$$

where $\gamma\approx3Re\left(\chi_{1111}^{(3)}\right)\omega_j^{(3)\pm}F^2/(8nc)$ is the waveguide nonlinearity parameter and $Re\left(\chi_{1111}^{(3)}\right)$ is real part of $\chi_{1111}^{(3)}$.

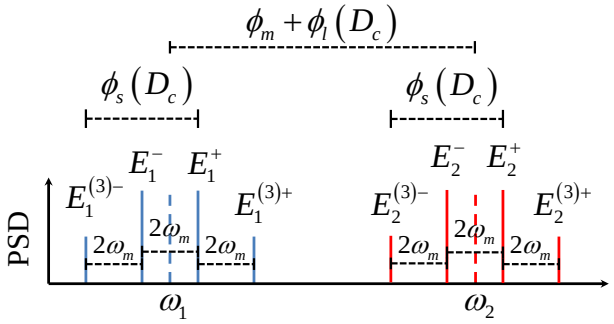

Figure 4.1: Illustrations of optical spectra and phase-mismatches among frequency-components of two SMOSs in a dispersive Kerr medium.

4.1.1 Identical carrier-wavelengths

In the case that E_1 and E_2 have the same carriers such that $\omega_1=\omega_2=\omega_0$, mode-propagation constants of $E_j^{\pm}$ and $E_1^{(3)\pm}$ are respectively given by $\beta^{\pm}=\beta_0^{\pm}\pm\omega_m\beta_1+0.5\omega_m^2\beta_2$ and $\beta^{(3)\pm}=\beta_0^{(3)\pm}\pm3\omega_m\beta_1+0.5\left(\pm3\omega_m\right)^2\beta_2$ with $\beta_{n=1,2}=d^n\beta^{\pm}/d\omega^n\Big|_{\omega=\omega_0}$ [1]. For the Kerr medium comprised of regular single-mode fiber (SMF), the birefrinigence of the SMF is on the order of 10^{-7} resulting in identical β_1 for orthogonally polarized E_1 and E_2. Using the initial phase-difference between the two SMOSs $\phi_m=0.5\left[\left(\phi_2^+-\phi_2^-\right)-\left(\phi_1^+-\phi_1^-\right)\right]$, $\phi_{L0}^{\pm}=2\phi_1^{\mp}-\phi_1^{\pm}$, and the

approximation of $\beta_0^+ \approx \beta_0^- \approx \beta_0^{(3)+} \approx \beta_0^{(3)-}$, Eq. (4.6) becomes

$$\frac{\partial}{\partial z} A_1^{(3)\pm}(z) = -i\frac{8}{9}\gamma P_0^{1.5}\left(1+e^{\mp i2\phi_m}\right)e^{i\left(4\omega_m^2\beta_2 z-\phi_{L0}^{\pm}\right)} \quad . \tag{4.7}$$

By integrating $A_1^{(3)\pm}$ over z in the Kerr medium, $A_1^{(3)\pm}$ at $z=L_{Kerr}$ is given by

$$A_1^{(3)\pm}(L_{Kerr}) = -\frac{2\gamma P_0^{1.5}\left(e^{\mp i2\phi_m}+1\right)\left(e^{i2\phi_s}-1\right)e^{-i\phi_{L0}^{\pm}}}{9\beta_2\omega_m^2} \tag{4.8}$$

where $\phi_s = 2\omega_m^2\beta_2 L_{Kerr} = \omega_m D_c \Delta\lambda_s L_{Kerr}$ is the intra-SMOS phase-mismatch, as illustrated in Fig. 4.1, with D_c being the CD parameter of the Kerr medium, $\Delta\lambda_s = \lambda^+ - \lambda^-$ being wavelength separation and $\lambda^{\pm}$ being wavelength of $E_1^{\pm}$. The power of $E_1^{(3)\pm}$ is calculated using $P_1^{(3)\pm} = \left|A_1^{(3)\pm}(L_{Kerr})\right|^2$ leading to

$$P_1^{(3)\pm} = \frac{256\gamma^2 P_0^3 L_{Kerr}^2}{81}\left(\frac{\sin(\phi_s)}{\phi_s}\right)^2 \cos^2(\phi_m). \tag{4.9}$$

Similarly, the power of $E_2^{(3)\pm}$ at the output of Kerr medium $P_2^{(3)\pm}$ is also given by modified Eq. (4.9). Equation (4.9) indicates that $P_1^{(3)\pm}$ varies sinusoidally with the initial phase-difference ϕ_m and is proportional to $sinc^2(\phi_s)$ which dramatically reduces the efficiency of the FWM process as the intra-SMOS phase-mismatch ϕ_s increases. $0.5\left(\phi_j^+ - \phi_j^-\right)$ in ϕ_m refers to the phase of the j^{th} SMOS $\omega_m t_j$ induced by group-delay of the SMOS t_j, and $\phi_m = 0.5\left[\left(\phi_2^+ - \phi_2^-\right) - \left(\phi_1^+ - \phi_1^-\right)\right] = \omega_m t_d$ represents the phase-shift of two SMOSs induced by group-delay difference $t_d = t_2 - t_1$ of the two SMOSs.

4.1.2 Different carrier-wavelengths

When E_1 and E_2 have different carriers such that $\omega_1 \neq \omega_2$, mode-propagation constants of $E_j^{\pm}$ and $E_1^{(3)\pm}$ are respectively given by $\beta_j^{\pm} = \beta_{j,0}^{\pm} \pm \omega_m\beta_{j,1} + 0.5\omega_m^2\beta_{j,2}$ and $\beta_1^{(3)\pm} = \beta_{1,0}^{(3)\pm} \pm 3\omega_m\beta_{1,1} + 0.5\left(\pm 3\omega_m\right)^2\beta_{1,2}$ with $\beta_{j,n} = d^n\beta_j^{\pm}/d\omega^n\big|_{\omega=\omega_j}$. Under the

approximations of $\beta_{1,0}^{+} \approx \beta_{1,0}^{-} \approx \beta_{1,0}^{(3)+} \approx \beta_{1,0}^{(3)-}$ and $\beta_{2,0}^{+} \approx \beta_{2,0}^{-}$, Eq. (4.6) becomes

$$\frac{\partial}{\partial z} A_1^{(3)\pm}(z) = -i\frac{8}{9}\gamma P_0^{1.5}\left[1+e^{\mp i\left(2\phi_l+2\phi_m\right)}\right]e^{i\left(4\omega_m^2\beta_{1,2}z-\phi_{L0}^{\pm}\right)} \tag{4.10}$$

where $\phi_l = \omega_m \Delta\beta_1 z$ is the inter-SMOS phase-mismatch, $\Delta\beta_1 = \beta_{2,1} - \beta_{1,1} = D_c \Delta\lambda_l$ corresponds to the group-velocity difference between $E_1^{\pm}$ and $E_2^{\pm}$, $\phi_m = 0.5\left[\left(\phi_2^{+} - \phi_2^{-}\right) - \left(\phi_1^{+} - \phi_1^{-}\right)\right] = \omega_m t_d$ is the initial phase-difference between the two SMOSs, and $\phi_{L0}^{\pm} = 2\phi_1^{\mp} - \phi_1^{\pm}$ is a constant phase-shift. Using $2\omega_m^2\beta_{1,2}L_{Kerr} = \phi_s$, the power of first-order sideband $P_1^{(3)\pm}$ at the output of Kerr medium is given by

$$P_1^{(3)\pm} = \frac{64\gamma^2 P_0^3 L_{Kerr}^2}{81}\left[a^2 + \left(b^{\mp}\right)^2 + 2ab^{\mp}\cos\left(2\phi_m - \phi_l\right)\right] \tag{4.11}$$

where $a = \sin(\phi_s)/\phi_s, b^{\mp} = \sin\left(\phi_l \mp \phi_s\right)/\left(\phi_l \mp \phi_s\right)$. Similarly, the power of $E_2^{(3)\pm}$ at the output of Kerr medium $P_2^{(3)\pm}$ is given by modified Eq. (4.11) where $\phi_s = 2\omega_m^2\beta_{2,2}L_{Kerr}$, ϕ_m and ϕ_l are replaced with $-\phi_m$ and $-\phi_l$, respectively. The inter-SMOS phase-mismatch parameter ϕ_l in Eq. (4.11) appears only when $\omega_1 \neq \omega_2$ and arises from the difference between the group-velocities of $E_1^{\pm}$ and $E_2^{\pm}$. Under the limit $\omega_1 \to \omega_2$, the group-velocities of $E_1^{\pm}$ and $E_2^{\pm}$ become identical, ϕ_l becomes zero, and Eq. (4.11) reduces to Eq. (4.9) as expected. Furthermore, as the value of $D_c \to 0$, Eq. (4.9) and Eq. (4.11) reduce to $P_1^{(3)\pm} = 256\gamma^2 P_0^3 L_{Kerr}^2 \cos^2(\phi_m)/81$ in agreement with Eq. (2.10) that describes the analytical solution of P_1 in the case of non-dispersive Kerr medium.

4.2 Experimental verification

Figure 4.2(a) presents a schematic of a Kerr phase-interrogator used for

experimental demonstration of the CD impact of Kerr medium in the case of identical carrier-wavelengths. A continuous-wave laser (Agilent 81980A) with wavelength $\lambda = 1550$ nm is amplitude-modulated using a sinusoidal electrical signal generator (HP 83752A) with a modulation frequency f_m to obtain a SMOS with a power oscillation frequency of $f_s = 2f_m$. A polarization beam splitter divides the power of the SMOS into parallel and perpendicular components that respectively propagate in reference and delay paths. A motorized variable delay line is placed in the delay path to vary the group-delay difference t_d between the parallel and perpendicular components. A polarization beam combiner recombines the parallel and perpendicular components, and the peak powers of these components are ensured to be maximum and equal using two polarization controllers, PC1 and PC2. The recombined signal is amplified using an Erbium-doped fiber amplifier (Amonics AEDFA-33-B-FA) to attain total peak power P_P = 20mW, and is launched into a Kerr medium comprised of a 2 km long single-mode fiber (SMF-28e) with waveguide nonlinearity of $\gamma = 1.25$ W^{-1} /km and chromatic dispersion of $D_c = 16.7$ ps/(nm×km) at a wavelength of 1550 nm. For most fiber such as SMF-28e, random variations in birefringence and the orientation of the birefringence axes force the Stokes vector to fill the entire surface of the Poincare sphere over a length scales ~1 km [1]. As this distance is shorter than the length of the SMF used as Kerr medium, the Stokes parameters of E_1 and E_2 can be considered filling the whole Poincare sphere, and thus the factor of 8/9 in Eq. (4.1) is valid. Propagation of the parallel and perpendicular components in the Kerr medium leads to the generation of sidebands

due to the nonlinear interaction between the orthogonally polarized components. In the case of identical carrier-wavelengths, generated first-order sidebands E_1^{3-} and E_2^{3-} are overlapped in the optical spectrum. The generated first-order sidebands are extracted by a tunable band-pass filter (TeraXion TFC) with a 3 dB bandwidth of 3 GHz.

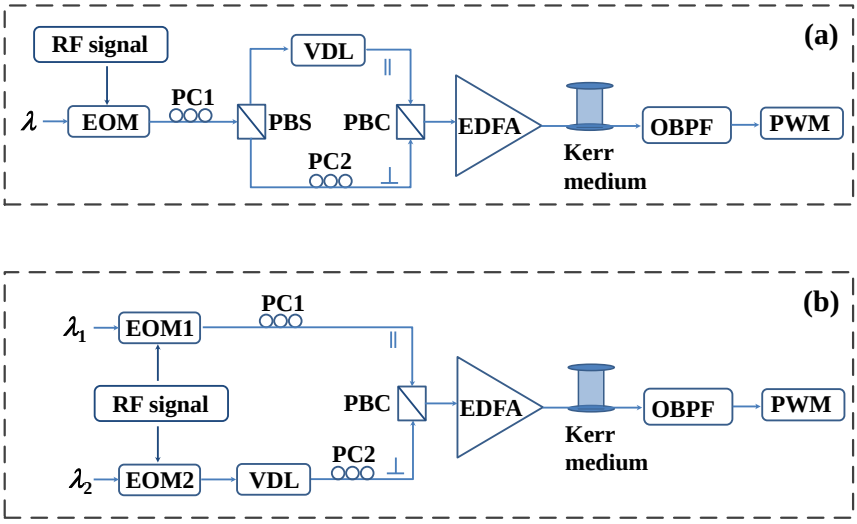

Figure 4.2: Schematic of a Kerr phase-interrogator used for demonstration of the CD impact of Kerr medium in the cases of (a) identical and (b) different carrier-wavelengths. EOM: electro-optic modulator; RF: radio frequency; PC: polarization controller; PBS: polarization beam splitter; VDL: variable delay line; PBC: polarization beam combiner; EDFA: erbium-doped fiber amplifier; OBPF: optical band-pass filter; PWM: power meter.

The total power of the sidebands $P_1 = P_1^{(3)-} + P_2^{(3)-} = 2P_1^{(3)-}$ is measured using a power-meter (Agilent/HP 81536A) as t_d is varied from -50 ps to 30 ps. Figure 4.3(a) presents the measured $P_1(t_d)$ at different values of f_m between 10 GHz and 30 GHz. Also presented in Fig. 4.3(a) are the theoretical values of $P_1(t_d)$ calculated using Eq. (4.9) with $\phi_m = 2\pi f_m t_d$, $|\phi_s| = |2\pi f_m D_c \Delta\lambda_s L_{Kerr}|$, $D_c = 16.7$ ps/(nm×km), $\lambda = 1550$ nm, L_{Kerr}=2 km, and $\Delta\lambda_s = (-\lambda^2 / c) f_s$ showing close agreement between theory and experiment. The initial phase-difference ϕ_m between the two SMOSs is linearly

proportional to t_d indicating that the measured P_1 varies sinusoidally with ϕ_m as predicted by Eq. (4.9). Also, for f_m=30 GHz, $|\phi_s| = 0.96\pi$ leading to $\text{sinc}^2(\phi_s) \approx 0$ and $P_1 \approx 0$ in agreement with experimentally measured value. To investigate the variation of P_1 with $|\phi_s|$, the value of t_d is fixed at 0 ps, and the value of f_m is varied between 10 GHz to 40 GHz to obtain $P_1(|\phi_s|)$. Figure 4.3(b) presents the measured values of $P_1(|\phi_s|)$ along with the theoretical values calculated using Eq. (4.9) with $\phi_m = 0$. The measured value of P_1 varies as a squared-sinc function of $|\phi_s|$ in close agreement with the theoretical calculations.

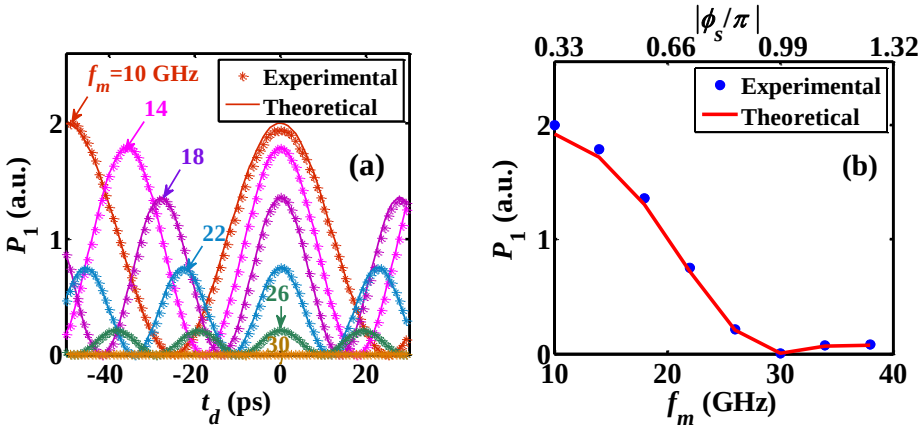

Figure 4.3: Experimental and theoretical results of (a) $P_1(t_d)$ at different f_m, and (b) P_1 at t_d=0 ps as a function of $|\phi_s|$ in the case of identical carrier-wavelengths.

To demonstrate the CD impact of Kerr medium in the case of different carrier-wavelengths, the Kerr phase-interrogator is modified as illustrated in Fig. 4.2(b) such that the SMOSs in the reference and the delay paths are carried by lasers at wavelengths $\lambda_1 = 1551$ nm and $\lambda_2 = \lambda_1 + \Delta\lambda_1$, respectively. Unlike the case of identical carrier-wavelength, generated first-order sidebands $E_1^{(3)-}$ and $E_2^{(3)-}$ do not overlap in optical spectrum. The tunable band-pass filter is used to extract $E_1^{(3)-}$ only and the power-meter measures the power of this extracted sideband such

that $P_1 = P_1^{(3)-}$. Figure 4.4(a) presents the measured values of P_1 as t_d is varied from 0 ps to 80 ps for different $\Delta\lambda_l$ between 0.55 nm and 1.15 nm. Figure 4.4(a) also presents theoretical values of P_1 calculated using Eq. (4.11) with D_c=16.7 ps/(nm×km), f_m =10 GHz, $\lambda_1 = 1551$ nm and L_{Kerr}=2 km showing close agreement between theory and experiment. Measurements in Fig. 4.4(a) show that increasing $\Delta\lambda_l$ causes a phase-shift to the sinusoidal variation $P_1(t_d)$ as predicted by Eq. (4.11) where increasing $\Delta\lambda_l$ increases $\phi_l = 2\pi f_m D_c \Delta\lambda_l L_{Kerr}$ which adds a phase-shift ϕ_l to the sinusoidal variation $P_1(\phi_m)$ with $\phi_m = 2\pi f_m t_d$. Also, the extinction ratio P_1^{max} / P_1^{min} declines as $\Delta\lambda_l$ increases indicating that a reduction in the extinction ratio of $P_1(t_d)$ occurs when the carrier wavelengths of SMOSs are different. To further investigate the extinction ratio of $P_1(t_d)$, the value of P_1^{max} / P_1^{min} is measured as $\Delta\lambda_l$ is varied from 0.66 nm to 3.66 nm in steps of 0.2 nm. Figure 4.4(b) presents the measured values of P_1^{max} / P_1^{min} as a function of $\Delta\lambda_l$ showing that the ratio P_1^{max} / P_1^{min} decreases dramatically as $\Delta\lambda_l$ increases to 1.46 nm and then remains low as $\Delta\lambda_l$ further increases. Also presented in Fig. 4.4(b) are theoretical values of P_1^{max} / P_1^{min} calculated using $P_1^{max} = 64\gamma^2 P_0^3 L_{Kerr}^2 (a+b)^2 / 81$ for $\cos(2\phi_m - \phi_l) = 1$ and $P_1^{min} = 64\gamma^2 P_0^3 L_{Kerr}^2 (a-b)^2 / 81$ for $\cos(2\phi_m - \phi_l) = -1$ in Eq. (4.11) in close agreement with the experimental results.

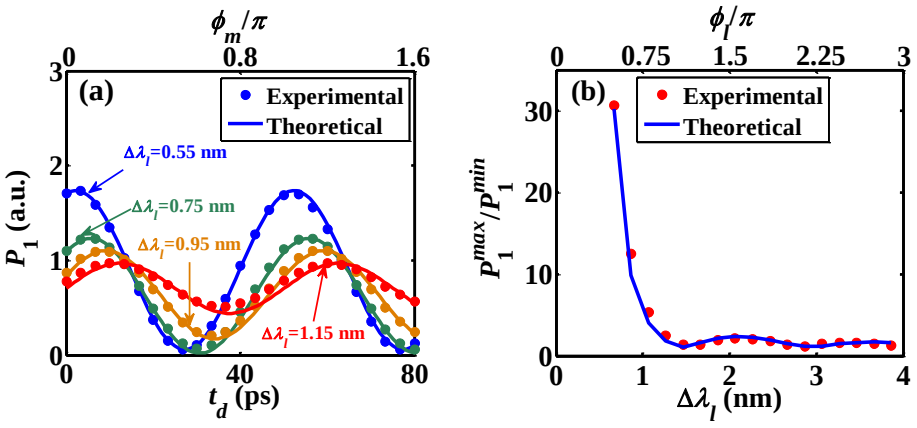

Figure 4.4: Experimental and theoretical results of (a) $P_1(t_d)$ for different $\Delta\lambda_l$, and (b) P_1^{max}/P_1^{min} as a function of ϕ_l.

4.3 Implication to Kerr phase-interrogator based sensing devices

The sinusoidal variation of P_1 with ϕ_m in Eqs. (4.9) and (4.11) accounts for the core functionality of the Kerr phase-interrogator for sensing applications. Any parameter that changes the ϕ_m can be acquired utilizing sinusoidal dependence of P_1 on ϕ_m. The maximum value of $P_1(\phi_m)$ reduces dramatically as ϕ_s increases which decreases the measurement signal-to-noise ratio (SNR). Furthermore, ϕ_l reduces the extinction ratio P_1^{max}/P_1^{min} of the sinusoidal variation $P_1(\phi_m)$ leading to reduced sensitivity in the Kerr phase-interrogator based sensor. Finally, ϕ_l induces additional phase between the SMOSs such that the final phase difference is $2\phi_m - \phi_l$ which leads to deviation of the measurements from expected values.

Reduction in the FWM efficiency and the extinction ratio P_1^{max}/P_1^{min} that arise from the intra-SMOS ϕ_s and inter--SMOS ϕ_l phase-mismatches, respectively, can be eliminated by utilization of Kerr medium with low CD. The single-mode fiber is

replaced with dispersion-shifted fiber (DSF) as Kerr medium with a zero dispersion wavelength at 1552 nm. The values of P_1 as a function of t_d are recorded for different $\Delta\lambda_l$ between 0.6 nm and 1.2 nm, and the measurements are presented in Fig. 4.5. The measured sinusoidal dependence of $P_1(t_d)$ presented in Fig. 4.5 are identical for different $\Delta\lambda_l$. Using D_c=0 gives a=1 and $b^{\mp}=1$, and Eq. (4.11) becomes $P_1^{(3)\pm}=256\gamma^2P_0^3L_{Kerr}^2\cos^2(\omega_m t_d)/81$ indicating dispersion-independent sinusoidal variation $P_1^{(3)\pm}(t_d)$ in agreement with experimental results.

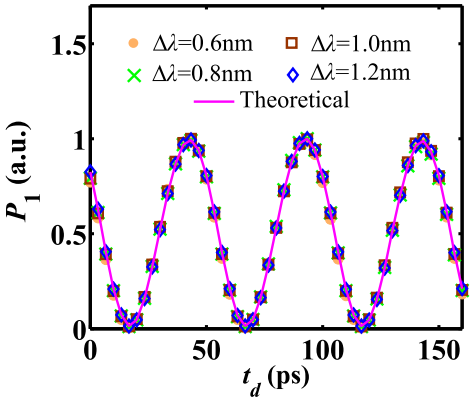

Figure 4.5: Experimental results of $P_1(t_d)$ for different $\Delta\lambda_l$ for a Kerr medium comprised of a 2 km long DSF with a zero-dispersion wavelength of 1552 nm.

4.4 Conclusion

The theory of FWM is employed to investigate the CD impact on the nonlinear interaction between two orthogonally-polarized SMOSs with identical or different carrier-wavelengths. Theoretical analysis reveals that CD induces intra-SMOS phase-mismatch ϕ_s when the carrier-wavelengths of two orthogonally polarized SMOSs are identical and additional inter-SMOS phase-mismatch ϕ_l when the carrier-wavelengths are different. Predictions of the theoretical analysis are

experimentally verified using a Kerr phase-interrogator with a dispersive Kerr medium. Experimental results show that increasing ϕ_s reduces the magnitude of the sinusoidal dependence of P_1 on ϕ_m, and that increasing ϕ_l leads to decrease in the magnitude, reduction in the extinction-ratio, and shift in the phase of $P_1(\phi_m)$ in agreement with the theoretical analysis. The impact of ϕ_s and ϕ_l can be eliminated by utilization of a Kerr medium with zero CD. This analytical study provides insight into CD impact on the operation of the Kerr phase-interrogator and the tools required for the optimization of the performance of Kerr phase-interrogator based sensing devices.

5 Chromatic-dispersion characterization of optical fibers using a Kerr phase-interrogator

This chapter presents a novel approach for measurements of chromatic dispersion (CD) in long optical fibers using a Kerr phase-interrogator. This approach utilizes a Kerr phase-interrogator to measure the phase variation of a sinusoidally-modulated optical signal (SMOS) induced by traveling in a fiber under test as the laser carrier wavelength and the modulation frequency of the SMOS are varied. CD measurements for several fibers including a standard single-mode silica fiber and a dispersion-shifted fiber are experimentally demonstrated.

Dispersion of group birefringence in a long polarization-maintaining fiber (PMF) is also characterized in this chapter. Two SMOSs are respectively launched into fast and slow axes of a PMF under test. Wavelength dependent group-delay difference between the two SMOSs induced by group birefringence of PMF is measured using a Kerr phase-interrogator, and dispersion of group birefringence is obtained utilizing the wavelength dependence of group-delay difference. Measurements of wavelength dependent group birefringence and group birefringence dispersion for a 459.4-m Panda PMF are experimentally demonstrated.

5.1 Background

Chromatic-dispersion is a critical parameter in optical fibers because it limits the data-rate of long-haul telecommunication systems and the efficiency of nonlinear four-wave mixing through pulse-broadening, walk-off, and phase mismatch. There are several approaches for the measurements of CD in kilometers-long optical fibers such as the pulse-delay method [27], the modulation phase-shift method [28], and the Sagnac interferometer based method [29, 30]. CD in fibers with lengths on the order of one meter is measured using methods based on Mach–Zehnder and Michelson interferometers [31, 32].

The modulation phase-shift method has been widely used because it enables the measurement of CD at picosecond-level precision. This method measures the shift in the phase of a SMOS induced by propagation in a fiber under-test (FUT) as the laser wavelength is varied allowing for the determination of the relative groups-delay $\Delta t_d(\lambda) = t_d(\lambda) - t_d(\lambda^{ref})$ as a function of wavelength λ. CD is then obtained using $D(\lambda) = (1/L)d\{\Delta t_d\}/d\lambda$, where L is the length of the fiber under-test, and λ^{ref} is a reference wavelength. Current implementations of this method are bandwidth-limited because they utilize electronic signal-processing for phase-shift acquisition. A novel implementation that utilizes all-optical signal processing for phase-shift acquisition can be achieved using a Kerr phase-interrogator. The Kerr phase-interrogator converts phase variation of a SMOS into power variation by ultrafast all-optical signal processing based on the Kerr nonlinear effect.

PMF can be used for ultrafast all optical switching, wavelength-tunable

ultra-short pulse generation, and quantum key distribution, where PMF is hundreds of meters in length [33-35]. For these applications, wavelength dependence of group birefringence is important because it governs the walk-off length that has influence on temporal profile of amplitude and spectra of optical pulses through nonlinear optical effects. Interferometric techniques are widely used to characterize wavelength dependent group birefringence by measurement of phase birefringence of a PMF [36-38]. However, the maximum length of investigated PMF is less than 10 m, which is limited by the short coherent length of a broadband light used in interferometric techniques. To extend the maximum measurable fiber length, a compensation for the optical path difference of fast and slow axes is required for each laser wavelength.

Kerr phase-interrogator has been demonstrated for measurement of group-delay difference of two SMOSs. Because the group-delay difference of two SMOSs that respectively propagate in the fast and slow axes of a PMF is proportional to the group birefringence, a Kerr phase-interrogator can characterize group birefringence and group birefringence dispersion of a PMF.

5.2 Chromatic-dispersion measurement of optical fibers

In this section, a novel approach for CD measurements in long optical fibers based on a Kerr phase-interrogator is presented. The Kerr phase-interrogator setup is configured for CD measurement by measuring relative and absolute group-delays of a SMOS as a function of laser carrier-wavelength. Theoretical analysis shows that the

variation of the sideband power generated by nonlinear Kerr effect determines the relative group-delay when the laser wavelength is varied, and determines the absolute group-delay when the frequency of the SMOS is varied. CD measurements in standard single-mode silica fibers (SMF-28) and other commercially available fibers are experimentally demonstrated.

5.2.1 Experimental setup

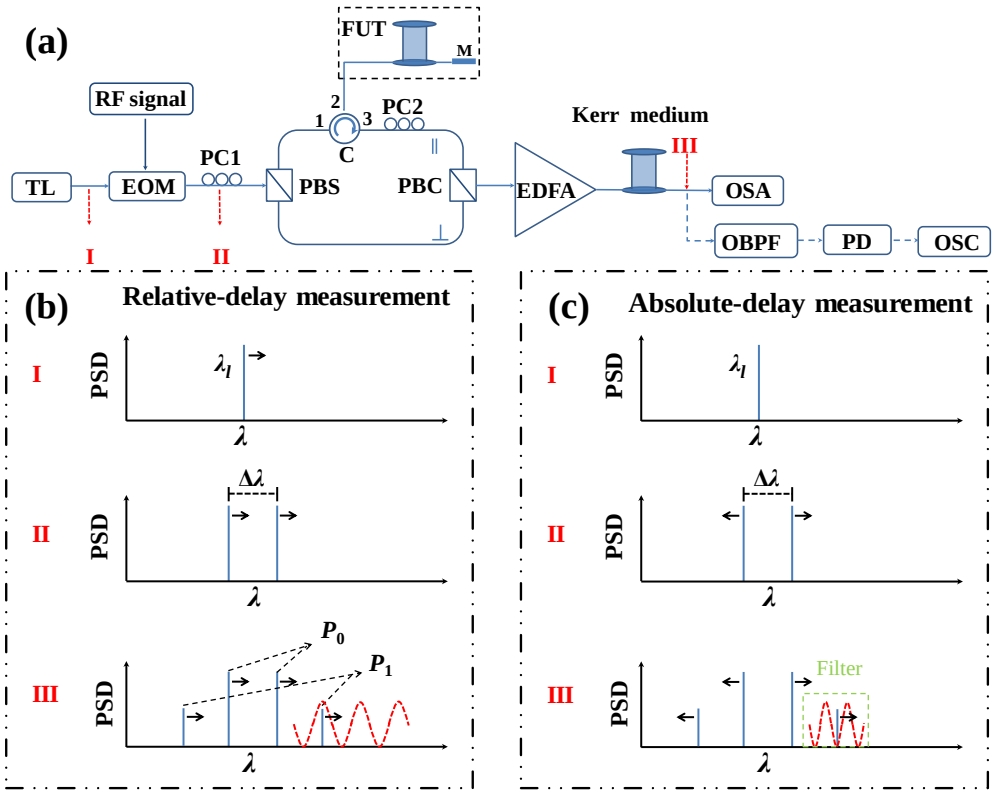

Figure 5.1: Schematic of (a) the dispersion measurement setup based on a Kerr phase-interrogator, and illustrations of the spectral evolution with the variation of (b) the laser wavelength λ_l and (c) SMOS frequency f_s; dotted line indicates the variation of the power of the side-band as λ_l and f_s are varied. TL: tunable laser; RF: radio-frequency; EOM: electro-optic modulator; PC: polarization controller; FUT: fiber under test; M: mirror; PBS: polarization beam splitter; PBC: polarization beam combiner; EDFA: Erbium-doped fiber amplifier; OSA: optical spectrum analyzer; PD: photodiode; OSC: oscilloscope; PSD: power spectral density.

Figure 5.1(a) shows the Kerr phase-interrogator configured for CD measurement. A tunable laser (Agilent 81980A) with a wavelength λ_l is amplitude-modulated using a sinusoidal electrical signal generator (HP 83752A) to obtain a SMOS oscillating at a frequency f_s. The optical spectrum of the SMOS is composed of two distinct peaks separated by $\Delta\lambda = |(-\lambda_l^2 / c) f_s|$ with *c* being speed of light in vacuum, as illustrated in Fig. 5.1(b). A polarization beam splitter splits the power of the SMOS into a fiber-under-test (FUT) path and a reference path, and a circulator connects a FUT that is terminated with a mirror to the FUT path. A polarization beam combiner recombines the signals from the FUT and the reference paths, and the combined signal is amplified using an Erbium-doped fiber amplifier (Amonics AEDFA-33-B-FA). Two polarization controllers, PC1 and PC2, ensure the peak powers of the orthogonal components of the combined signal are maximum and equal. The amplified signal is launched into a nonlinear Kerr medium comprised of a dispersion-shifted fiber (DSF) with a zero dispersion wavelength at $\lambda = 1552$ nm, a length L_{Kerr}=2.27 km and waveguide nonlinearity $\gamma = 2.28$ W^{-1}/km.

Nonlinear Kerr-effect in the Kerr medium leads to the formation of distinct sidebands P_i with i=1,2,..., as illustrated in Fig. 5.1(b), and the power of the first side-band is given by

$$P_1(\lambda_l) = P_1^{max} \cos^2\left[\pi f_s t_d(\lambda_l) + \phi_0\right] \tag{5.1}$$

for $4\gamma L_{Kerr} P_P / 9 < 0.4$, where P_P is total peak power of the orthogonal components of the combined signal, P_1^{max} is the maximum value that P_1 attains, $t_d(\lambda_l)$ is the time-delay required to travel through the FUT, and ϕ_0 is a constant phase-shift. As

the laser wavelength is varied, the value of t_d varies due to CD in the FUT leading to a variation in the power of the first-order sideband, as illustrated by the dotted red line in Fig. 5.1(b). The spectrum of the signal at the output of the Kerr medium is measured using an optical spectrum analyzer (Agilent 86142B).

The relative phase $\Delta\phi(\lambda_l) = \phi(\lambda_l) - \phi_{ref}$ is obtained from $P_1(\lambda_l)$ using the relation

$$\Delta\phi(\lambda_l) = \frac{1}{2}\arctan\left(\frac{\mathcal{H}\left\{2P_1(\lambda_l)/P_1^{max} - 1\right\}}{2P_1(\lambda_l)/P_1^{max} - 1}\right) - \phi_{ref} \tag{5.2}$$

where $\mathcal{H}$ is the Hilbert transform, and $\phi_{ref} = \pi f_s t_{ref} + \phi_0$ with t_{ref} being the absolute group-delay at a reference wavelength λ_l^{ref}. The Hilbert transform of signal *u* can be thought of as the convolution of $u(t)$ with the function $h(t) = 1/(\pi t)$, and thus $\mathcal{H}\{\cos(t)\} = \sin(t)$. Using $2P_1(\lambda_l)/P_1^{max} - 1 = \cos\left(2\pi f_s t_d(\lambda_l) + 2\phi_0\right)$ gives $\mathcal{H}\left\{2P_1(\lambda_l)/P_1^{max} - 1\right\} = \sin\left(2\pi f_s t_d(\lambda_l) + 2\phi_0\right)$. The relative group-delay $\Delta t_d(\lambda_l) = t_d(\lambda_l) - t_{ref}$ is obtained using

$$\Delta t_d(\lambda_l) = \Delta\phi(\lambda_l)/\pi f_s \tag{5.3}$$

and the CD is calculated using

$$D_c(\lambda_l) = \frac{1}{2L}\frac{d}{d\lambda_l}\left\{\Delta t_d(\lambda_l)\right\} \tag{5.4}$$

where *L* is the length of the FUT.

Measurement of the relative group-delay presented above does not specify whether Δt_d increases or decreases with λ_l, and hence, does not determine whether CD is normal with $D_c < 0$ or anomalous with $D_c > 0$. The absolute group-delay t_d must be measured at two consecutive wavelengths to specify the actual sign of

$D_c(\lambda_l)$. The Kerr phase-interrogator setup in Fig. 5.1(a) is modified for the measurement of t_d by replacing the optical spectrum analyzer with a 3 GHz band-pass filter (TeraXion TFC) followed by a photo-detector (New-Focus 1811) that is connected to an oscilloscope (Agilent DSO81204B). In the modified setup, the laser wavelength λ_l is fixed and the SMOS frequency f_s is varied which, according to Eq. (5.1), leads to the variation of the sideband power P_1, as illustrated by the dotted red line in Fig. 5.1(c). The relative phase $\Delta\phi(f_s)=\phi(f_s)-\phi_{init}$ is obtained from $P_1(f_s)$ using

$$\Delta\phi(f_s)=\frac{1}{2}\arctan\left(\frac{\mathcal{H}\{2P_1(f_s)/P_1^{max}-1\}}{2P_1(f_s)/P_1^{max}-1}\right)-\phi_{init} \tag{5.5}$$

where $\phi_{init}=\phi(f_s^{init})=\pi f_s^{init}t_d+\phi_0$ with f_s^{init} being the initial frequency of the SMOS. The absolute group-delay is calculated from the slope of $\Delta\phi(f_s)$ using

$$t_d=\frac{1}{\pi}\frac{d\Delta\phi(f_s)}{df_s} \tag{5.6}$$

5.2.2 Experimental results

We proof-test this approach by characterization of a standard single-mode SMF-28 with *L*=2.04 km. In the experiment, the total peak power P_P of two SMOSs is 20mW. The laser wavelength λ_l is varied in steps of 0.1 nm and the measured spectrum at the optical spectrum analyzer is recorded for each λ_l. Figure 5.2(a) presents several measured spectra clearly showing the variation of the sideband power as λ_l is increased. Figure 5.2(b) presents the measured values of P_1 as a function of λ_l for the wavelength range between $\lambda_l=1545$ nm and $\lambda_l=1555$ nm. Figure 5.2(c) presents the measured relative phase-difference $\Delta\phi_{meas}(\lambda_l)$ obtained from

$P_1(\lambda_l)$ using Eq. (5.2), and the polynomial fit $\Delta\phi_{fit}(\lambda_l)$ obtained by fitting $\Delta\phi_{meas}(\lambda_l)$ to a third degree polynomial. The value of $\Delta t_d(\lambda_l)$ is calculated from $\Delta\phi_{meas}(\lambda_l)$ using Eq. (5.3) and $D_c(\lambda_l)$ is obtained by using Eq. (5.4). Figure 5.2(d) presents the resulting $D_c(\lambda_l)$ showing close agreement with the results obtained using the standard modulation phase-shift method [28].

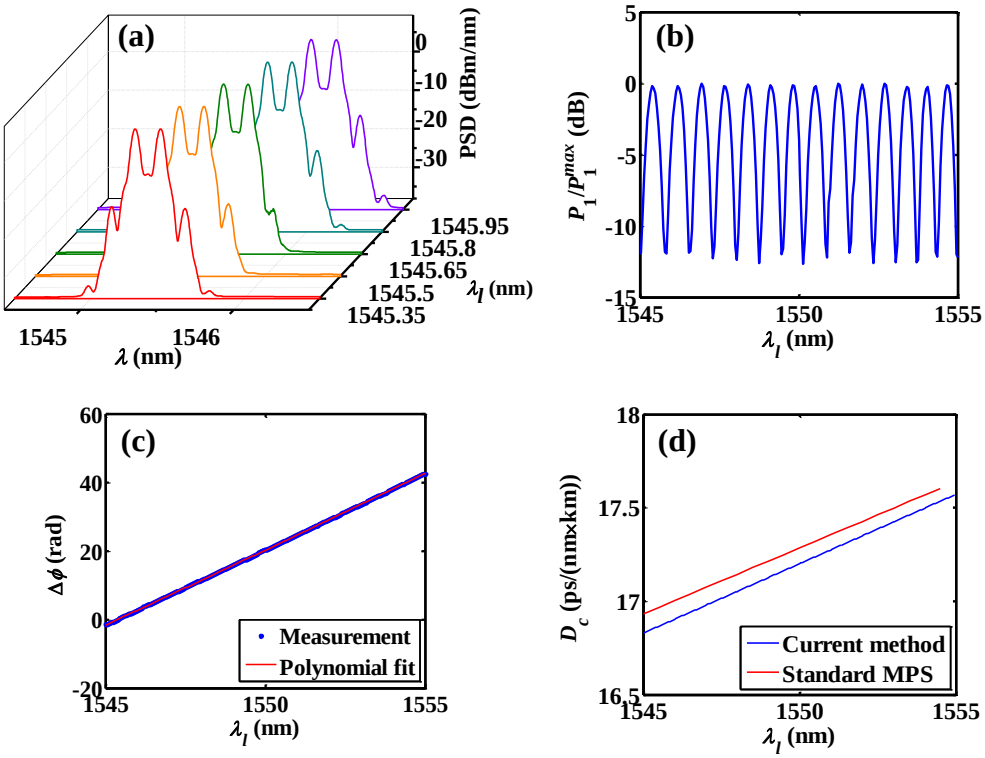

Figure 5.2: Experimental results for CD characterization of a single-mode fiber SMF-28 with L=2.04 km showing (a) spectra at the output of the Kerr medium for several laser wavelengths λ_l, (b) side-band power P_1 as a function of λ_l, (c) phase-difference $\Delta\phi$ as a function of λ_l, and (d) D_c as a function of λ_l along with values obtained using the standard modulation phase-shift method.

The laser wavelength is fixed at $\lambda_l = 1545$ nm and f_s is varied slowly at a rate of $r = 10$ MHz/s from an initial value $f_s^{init} = 20.000$ GHz to a final value $f_s^{fin} = 20.001$ GHz and the side-band power $P_1(t)$ is measured using an oscilloscope. The average of 16 traces of $P_1(t)$ is acquired using the oscilloscope and the time variable t is replaced by the frequency $f_s = rt$ leading to P_1 as a function

of f_s. Figure 5.3(a) presents a section of the measurement results of $P_1(f_s)$ showing a sinusoidal variation of P_1 as f_s increases in agreement with Eq. (5.1). The phase-difference $\Delta\phi(f_s)$ is obtained by applying Eq. (5.5) to $P_1(f_s)$ and the results are presented in Fig. 5.3(b). Application of Eq. (5.6) to $\Delta\phi(f_s)$ gives an absolute group-delay of $t_d = 20204.21458$ ns at $\lambda_l = 1545$ nm. Similarly, a value of $t_d = 20204.24123$ ns is measured at $\lambda_l = 1555$ nm indicating that t_d increases as λ_l increases and that CD is anomalous.

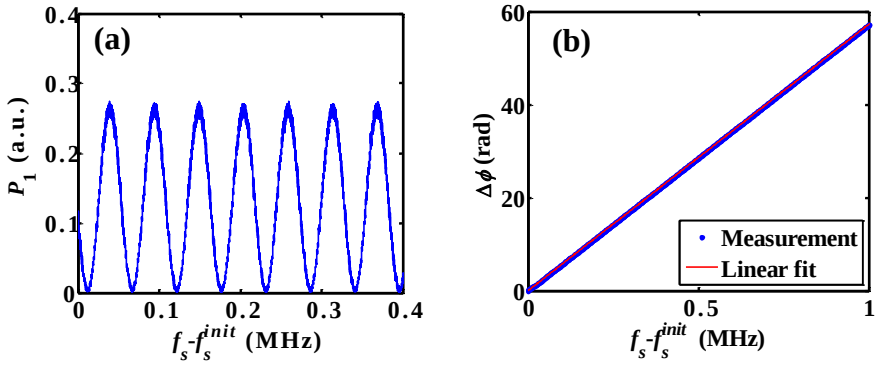

Figure 5.3: (a) Measured side-band power P_1 and (b) the measured phase-difference as a function of f_s-f_s^{init} with f_s^{init} =20 GHz.

The CD measurement process is repeated for a low-dispersion fiber (LDF) with L=5.96 km and a bend-insensitive fiber (BIF) with L=4.37 km, and the results are presented in Fig. 5.4.

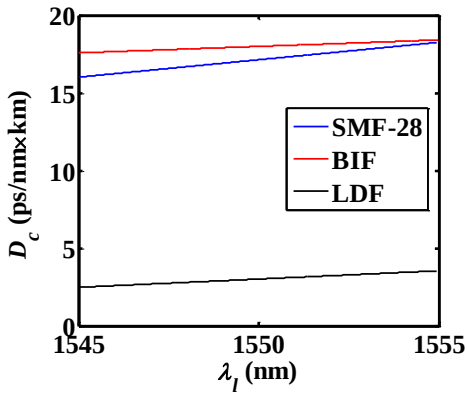

Figure 5.4: Measured $D_c(\lambda_l)$ for several fibers. SMF-28: standard single-mode fiber

with L=2.04 km; BIF: bend-insensitive fiber with L=5.96 km; LDF: low-dispersion fiber with L=4.37 km.

We also measure CD of a DSF with L=2.27 km for which the phase-difference $\Delta\phi$ does not vary monotonically with λ_l. Figure 5.5(a) presents the measured P_1 as λ_l is varied in steps of 0.5 nm within the wavelength range between $\lambda_l = 1535$ nm and $\lambda_l = 1565$ nm. Figure 5.5(b) presents the measured relative phase-difference $\Delta\phi_{meas}(\lambda_l)$ and a polynomial fit $\Delta\phi_{fit}(\lambda_l)$. Figure 5.5(c) presents the resulting $D_c(\lambda_l)$ showing a value of 0 ps/(nm×km) at $\lambda_l = 1552$ nm in close agreement with the value obtained using the standard modulation phase-shift method. The measured absolute group-delay t_d is 22298.17251 ns at $\lambda_l = 1535$ nm, 22298.13254 ns at $\lambda_l = 1550$ nm, and 22298.17712 ns at $\lambda_l = 1565$ nm indicating that CD is normal for $\lambda_l < 1552$ nm and anomalous for $\lambda_l > 1552$ nm.

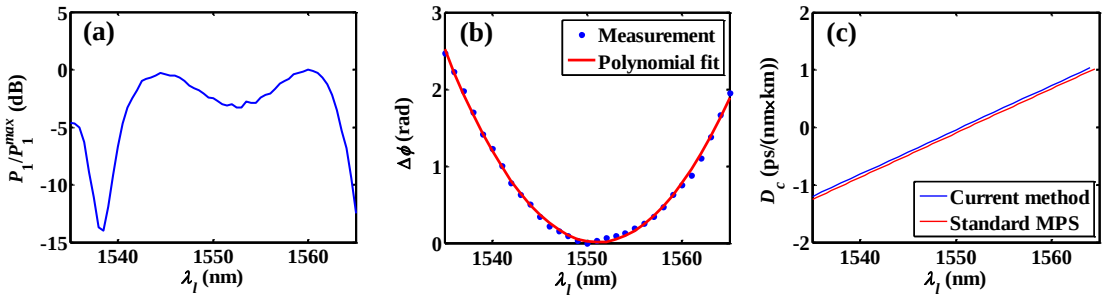

Figure 5.5： Experimental results for CD measurement of a DSF with L=2.27 km showing (a) the measured P_1 (λ_l), (b) measured phase-difference $\Delta\phi_{meas}(\lambda_l)$, and (c) measured CD $D_c(\lambda_l)$ along with the standard modulation phase-shift method measurement results.

5.2.3 Discussion

The precision of this method is obtained from the minimum detectable phase-difference $\Delta\phi^{min} = \pi f_s \Delta t_d^{min} = \alpha$ [39]. Using $f_s = 20$ GHz and $\alpha = 10^{-2}$ leads to a minimum detectable relative group-delay of $\Delta t_d^{min} = 159$ fs. It is possible to

achieve $f_s = 100$ GHz by using commercially available 50 GHz electro-optic modulators leading to $\Delta t_d^{min} = 32$ fs. Furthermore, the limits of CD measurement approach are estimated from the group-delay variation rate $\rho = D \times L = \Delta t_d / \Delta\lambda$ [30, 40]. The minimum measurable CD is $\rho^{min} = \Delta t_d^{min} / \Delta\lambda_l^{max} = \alpha / \pi f_s \Delta\lambda_l^{max}$ with $\Delta\lambda_l^{max}$ being the maximum laser scanning range. In our experimental setup, $\Delta\lambda_l^{max} = 30$ nm is limited by the gain region of the Erbium-doped fiber amplifier, $f_s = 20$ GHz, and $\alpha = 10^{-2}$ leading to $\rho^{min} = 5.3$ fs/nm. The maximum measurable CD is $\rho^{max} = \Delta t_d^{max} / \Delta\lambda_l^{min}$ where $\Delta\lambda_{min}$ is the minimum laser step. Requiring N sampling points within a cycle of $P_1(\lambda_l)$ leads to $\Delta\phi^{max} = \pi / N$ which corresponds to $\Delta t_d^{max} = 1/Nf_s$ and $\rho^{max} = 1/Nf_s\Delta\lambda_l^{min}$. Using the minimum wavelength step of our tunable laser $\Delta\lambda_{min} = 0.001$ nm, $f_s = 20$ GHz, and N=15 leads to $\rho^{max} = 3.33$ ns/nm.

5.3 Chromatic-dispersion characterization of birefringence in polarization-maintaining fiber

In this section, wavelength dependent group birefringence and group birefringence dispersion in 459.4 m Panda PMF are measured using a Kerr phase-interrogator.

5.3.1 Experimental setup

Figure 5.6 presents the schematic of a Kerr phase-interrogator for dispersion characterization of group birefringence. A continuous-wave light-wave from tunable

laser (Agilent 81980A, TL) with wavelength λ_l is amplitude modulated by electro-optic modulator (EO-Space) with modulation frequency f_m to obtain a SMOS oscillating at frequency $f_s=2f_m$. The SMOS is split by a polarization beam splitter into parallel and perpendicular components propagating in two paths with equal length, respectively, and are recombined by a polarization beam combiner. A polarization controller is used to adjust polarization state of the SMOS to ensure equal powers of two orthogonal polarization components after recombination. The parallel and perpendicular components of the combined SMOS respectively are launched into fast and slow axes of a PMF under test through a polarization-maintaining circulator (PMC). The transmission of FUT is reflected by a polarization-maintaining reflector that comprises a PMC with 1-port and 3-port connected and 2-port as input end. Amplified by an Erbium-doped fiber amplifier (Amonics AEDFA-33-B-FA), the combined signal is launched into 2.27 km DSF that acts as Kerr medium with a zero dispersion wavelength at $\lambda = 1552$ nm. Due to the nonlinear interaction in the Kerr medium, the formation of distinct sidebands is generated, and the power of the first-order sideband P_1 is expressed as

$$P_1(\lambda_l) = P_1^{max} \cos^2\left[\pi f_s t_d(\lambda_l) + \phi_0\right] \tag{5.7}$$

where $P_1^{\max}$ is the maximum value of $P_1(\lambda_l)$, ϕ_0 is a constant phase and t_d is group-delay difference corresponding to the round-trip-time difference between fast axis and slow axis of the FUT.

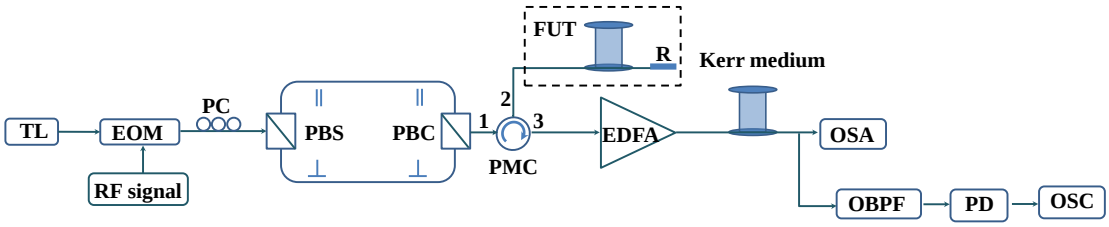

Figure 5.6: Schematic of the birefringence-characterization setup based on a Kerr phase-interrogator. TL: tunable laser; EOM: electro-optic modulator; RF: radio frequency; PC: polarization controller; PBS: polarization beam splitter; PBC: polarization beam combiner; PMC: polarization-maintaining circulator; FUT: fiber under test; R: reflector; EDFA: erbium-doped fiber amplifier; OSA: optical spectrum analyzer; OBPF: optical band-pass filter; PD: photodiode; OSC: oscilloscope.

Utilizing Eq. (5.2), the relative phase $\Delta\phi(\lambda_l)=\phi(\lambda_l)-\phi_{ref}$ is obtained from $P_1(\lambda_l)$, where $\phi(\lambda_l)=\pi f_s t_d(\lambda_l)+\phi_0$, and $\phi_{ref}=\pi f_s t_{ref}+\phi_0$ with t_{ref} being the absolute group-delay difference at a reference wavelength λ_{ref}. Accordingly, the relative group-delay difference $\Delta t_d(\lambda_l)=t_d(\lambda_l)-t_{ref}$ is obtained using Eq. (5.3), and the group birefringence dispersion D_B is quantified using Eq. (5.4).

The Kerr phase-interrogator setup in Fig. 5.6 is modified for measurement of t_{ref} by replacing the optical spectrum analyzer with a 3 GHz band-pass filter (TeraXion TFC) followed by a photo-detector (New-Focus 1811) that is connected to an oscilloscope (Agilent DSO81204B). In the modified setup, the laser wavelength is set at a reference wavelength λ_{ref} and the SMOS frequency f_s is linearly scanned which, according to Eq. (5.7), leads to the sinusoidal variation of the sideband power $P_1(f_s)$. The relative phase $\Delta\phi(f_s)=\phi(f_s)-\phi(f_s^{init})$ is demodulated from $P_1(f_s)$ using Eq. (5.5), where $\phi(f_s^{init})=\pi f_s^{init} t_{ref}+\phi_0$ with f_s^{init} being the initial frequency of the SMOS. The value of t_{ref} is calculated from the slope of $\Delta\phi(f_s)$ using Eq. (5.6).

Besides t_{ref}, another absolute group-delay difference t_{ref2} of the principal axes in the FUT must be measured at a wavelength λ_{ref2} to specify the actual sign of $\Delta t_d(\lambda_l)$.

The absolute group-delay difference is given by $t_d(\lambda_l)=t_{ref}+\Delta t_d(\lambda_l)$ leading to

$$B(\lambda_l)=\frac{c}{2L}\{t_d(\lambda_l)\} \tag{5.8}$$

where B represents group birefringence.

5.3.2 Experimental results

A Panda PMF in 459.4 m long is under test for birefringence characterization. In the experiment, the total peak power P_p of two SMOSs is 20mW. The laser wavelength λ_l is scanned from λ_1=1540 nm to λ_2=1565 nm in steps of 0.1 nm and the measured spectra at the optical spectra analyzer are recorded for each λ_l. Figure 5.7(a) presents the measured values of P_1 as a function of λ_l when the SMOS frequency is f_s=20GHz. Figure 5.7(b) presents the measured relative phase $\Delta\phi(\lambda_l)$ obtained from $P_1(\lambda_l)$ with $\lambda_{ref}=\lambda_1$.

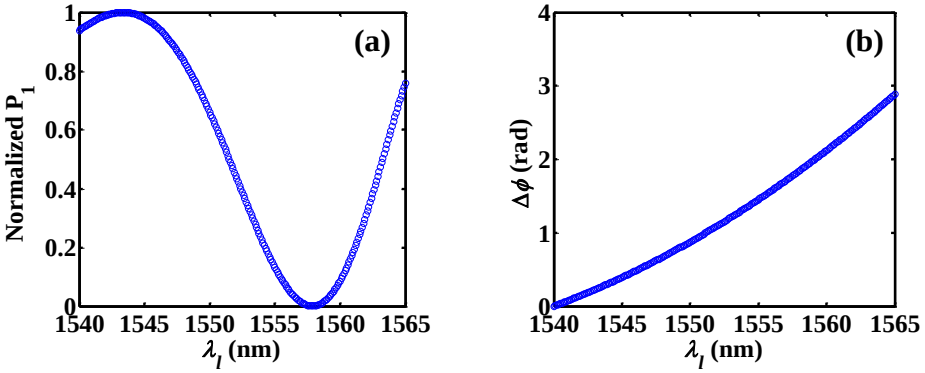

Figure 5.7: Experimental results of (a) sideband power P_1 and (b) relative phase $\Delta\phi$ as a function of λ_l for the Panda PMF when the oscillation frequency of SMOS is f_s=20GHz.

The laser wavelength is fixed at $\lambda_{ref}=\lambda_1$ and f_s is linearly scanned at a rate of r=80 GHz/s from an initial value f_s^{init}=16 GHz to a final value f_s^{fin}=24 GHz, and the sideband power $P_1(t)$ is acquired using an oscilloscope. The average of 16 traces of P_1(t) is acquired using the oscilloscope and the time variable t is replaced by the $f_s=rt$

leading to P_1 as a function of f_s. Figure 5.8(a) presents the measurement results for $P_1(f_s)$ showing a sinusoidal variation of P_1 as f_s increases in agreement with theoretical values calculated using Eq. (5.7). Presented in Fig. 5.8(b) are $\Delta\phi_{meas}(f_s)$ demodulated from $P_1(f_s)$ and the linear fit $\Delta\phi_{fit}(f_s)$ obtained by fitting $\Delta\phi(f_s)$ to a first degree polynomial. Application of Eq. (5.6) to $\Delta\phi_{meas}(f_s)$ results in an absolute group-delay difference of t_{ref}=1448 ps at λ_{ref}= λ_1. Similarly, a value of t_{ref2}=1493 ps is measured at λ_{ref2}= λ_2 indicating the increment of t_d as λ_l increases.

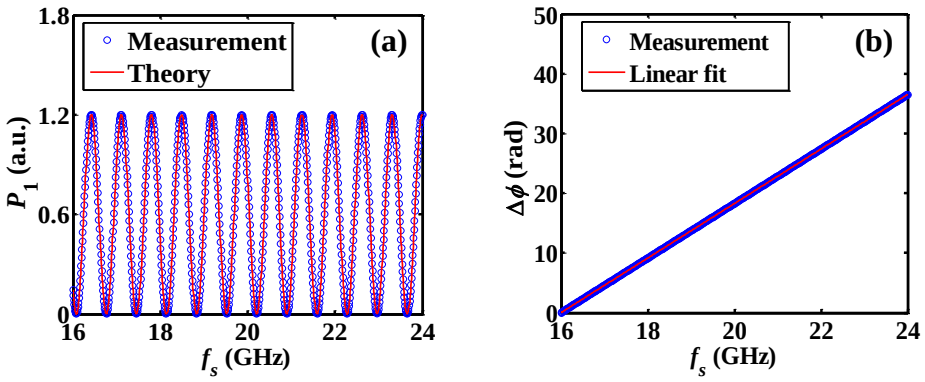

Figure 5.8: Experimental results of (a) sideband power P_1 and (b) relative phase $\Delta\phi$ as a function of f_s for the Panda PMF when the laser wavelength is λ_l= λ_1.

The values of absolute group-delay difference are calculated using $t_d(\lambda_l) = t_{ref} + \Delta t_d(\lambda_l)$ with t_{ref} =1448 ps and $\Delta t_d(\lambda_l) = \Delta\phi(\lambda_l)/\pi f_s$, and are presented in Fig. 5.9(a). Wavelength dependence of group birefringence $B(\lambda_l)$ is calculated from $t_d(\lambda_l)$ using Eq. (5.8) with L=459.4 m, and is presented in Fig. 5.9(b) showing a value of 4.785×10^{-4} at λ_l =1550 nm. Figure 5.9(c) presents group birefringence dispersion D_B calculated from $\Delta t_d(\lambda_l)$ using Eq. (5.4) showing D_B=1.85 ps/(nm×km) at λ_l =1550 nm.

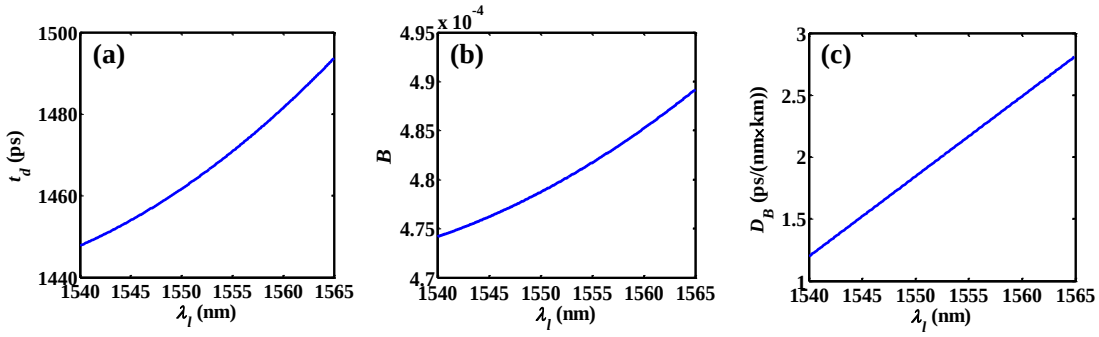

Figure 5.9: Experimental results of (a) absolute group-delay difference t_d, (b) group birefringence B and (c) group birefringence dispersion D_B as a function of λ_l for the Panda PMF.

6 Group-delay-based temperature sensing in linearly-chirped fiber Bragg gratings using a Kerr phase-interrogator

This chapter presents a novel temperature sensor that utilizes temperature dependence of reflection group-delay in a linearly chirped fiber Bragg grating (LC-FBG). The reflection group-delay of chirped grating changes with temperature leading to a variation in the phase of a sinusoidally-modulated optical signal (SMOS) reflected from the grating. A Kerr phase-interrogator converts the phase-variation into power variation allowing for high precision temperature sensing.

6.1 Background

Fiber Bragg grating (FBG) based temperature sensors have been widely used in medicine and industry [41-47]. These sensors utilize temperature dependence of fiber dimensions and refractive-index to measure temperature variation [48]. Existing FBG temperature sensors measure temperature variation by detecting shift in the central wavelength of the reflection spectrum allowing for a temperature sensitivity of 0.01nm/^{o}C at a wavelength of 1550 nm [49]. Spectral-variation based FBG sensors require a spectrum analyzer for acquisition of the reflection spectrum making temperature sensing slow and impractical for real-time monitoring applications. Furthermore, the temperature resolution is limited by the wavelength resolution of

spectrum analysis approaches.

Measurement of temperature change in FBGs can also be achieved by detection of variation in the phase of a laser reflected from a FBG. Homodyne and heterodyne interferometers can be used for conversion of the laser phase variation into power variation allowing for a high temperature sensitivity of 1 rad/^{o}C. However, homodyne and heterodyne interferometers require electronic feedback circuits to reduce environmental noise and require high-quality low phase-noise lasers limiting their use in practical applications.

A Kerr phase-interrogator that measures phase variation of a SMOS using nonlinear Kerr effect has been demonstrated. The phase of a SMOS is linearly proportional to the group-delay accumulated along the propagation path; therefore, a Kerr phase-interrogator can sense physical variations that induce group-delay changes in the propagation path of a SMOS. Indeed, the Kerr phase-interrogator can measure temperature-induced variations in the reflection group-delay of a LC-FBG allowing for temperature sensing.

In this chapter, a temperature sensor that utilizes temperature dependence of reflection group-delay in a LC-FBG is proposed and experimentally demonstrated. Theoretical analysis and numerical simulations show that the reflection group-delay in a LC-FBG varies linearly with temperature. A Kerr phase-interrogator setup is configured for sensing temperature-induced group-delay variation in a LC-FBG. Experimental measurements demonstrate temperature sensing in a LC-FBG at a sensitivity of 1.122 rad/^{o}C and a resolution of 0.0089 ^{o}C.

6.2 Temperature dependence of group-delay spectrum of a LC-FBG

6.2.1 Analytical model

The local Bragg period Λ at position *z* of a LC-FBG is expressed as

$$\Lambda_z = \Lambda_0 + c_{chirp} z \tag{6.1}$$

where Λ_0 is the Bragg period at the input of the grating and c_{chirp} is the grating's chirp rate given by $c_{chirp} = d\lambda_{res} / dz$ with λ_{res} being the resonance wavelength. At temperature T, an incident optical signal with a spectrum centered at λ_{res} is reflected from the LC-FBG at a resonance position *z* such that the Bragg period $\Lambda_{z,T}$ satisfies resonance condition [50]

$$\lambda_{res} = 2n_{eff}\Lambda_{z,T} \tag{6.2}$$

where n_{eff} is the effective refractive-index of the fiber. As the temperature changes from T to $T+\Delta T$, the effective refractive-index of the fiber changes to $(1+\alpha\Delta T)n_{eff}$, the resonance position shifts by Δz to $z+\Delta z$, and the local Bragg period $\Lambda_{z+\Delta z,T+\Delta T} = (1+\beta\Delta T)\Lambda_{0,T} + c_{chirp}(z+\Delta z)$ satisfies the resonance condition

$$\lambda_{res} = 2(1+\alpha\Delta T)n_{eff}\Lambda_{z+\Delta z,T+\Delta T} \tag{6.3}$$

where the constants $\alpha = (dn_{eff} / dT) / n_{eff}$ and $\beta = (d\Lambda / dT) / \Lambda$ are the normalized thermo-optic and thermal expansion coefficients of the fiber, respectively [51].

Replacing Eq. (6.2) in Eq. (6.3) leads to

$$\Delta z = -\frac{(\beta+\alpha)\Lambda_{z,T} + \alpha\beta\Lambda_{0,T}\Delta T - \beta c_{chirp} z}{c_{chirp}(1+\alpha\Delta T)}\Delta T \tag{6.4}$$

which reduces to

$$\Delta z = -\frac{(\beta+\alpha)\Lambda_z}{c_{chirp}}\Delta T \tag{6.5}$$

by ignoring the terms $\alpha\beta\Lambda_{0,T}\Delta T$ and $\beta c_{chirp} z$, and utilizing the approximation $1+\alpha\Delta T \approx 1$ and $\Lambda_{z,T} \approx \Lambda_z$. The relative reflection group-delay is given by $\Delta\tau_g = 2\Delta z / v_g$ and is expressed linearly in terms of ΔT by utilizing Eq. (6.5),

$$\Delta\tau_g = -\frac{2(\beta+\alpha)\Lambda_z}{v_g c_{chirp}}\Delta T \tag{6.6}$$

where v_g is group velocity. Figure 6.1 illustrates the variation of the resonance position along a LC-FBG with $c_{chirp} < 0$ as the temperature increases from T to $T+\Delta T$. The reflection position shifts away from the input of the LC-FBG leading to an increase in the reflection group-delay as indicated by Eq. (6.6).

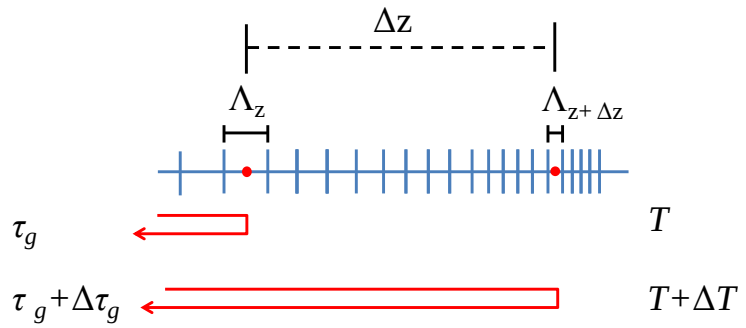

Figure 6.1: Illustration of the reflection group-delay change in a LC-FBG with c_{chirp}<0 as the temperature increases from T to $T+\Delta T$.

6.2.2 Numerical model

The reflection coefficient r as a function of wavelength for a LC-FBG with a raised-cosine apodization is numerically calculated using a piecewise-uniform approach [52]. Raised-cosine apodization with index-change profile $\delta n_{eff}(z) = \delta n_{eff\,0}\cos^2(\pi z / L)$ and $-L/2 \le z \le L/2$ [52] is used for the suppression of the ripples in the reflection group-delay spectrum of the LC-FBG, where L and

$\delta n_{eff\,0}$ are length and modulation depth of the LC-FBG, respectively. The reflection spectrum is then calculated using $R(\lambda)=|r(\lambda)|^2$, and the reflection group-delay spectrum is calculated from the phase of the reflection coefficient $\phi_r(\lambda)=phase\{r(\lambda)\}$ using [52]

$$\tau_g(\lambda)=\frac{d\phi_r(\lambda)}{d\omega}=-\frac{\lambda^2}{2\pi c}\frac{d\phi_r(\lambda)}{d\lambda} \tag{6.7}$$

where ω is the optical angular frequency, λ is the wavelength, and c is the speed of light in vacuum. The numerical calculations are repeated for different temperature variations ΔT using $n_{eff,T+\Delta T}=(1+\alpha\Delta T)n_{eff,T}$ and $\Lambda_{0,T+\Delta T}=(1+\beta\Delta T)\Lambda_{0,T}$ with $\alpha=7\times10^{-6}$ /°C and $\beta=5\times10^{-7}$ /°C for silica fibers [48].

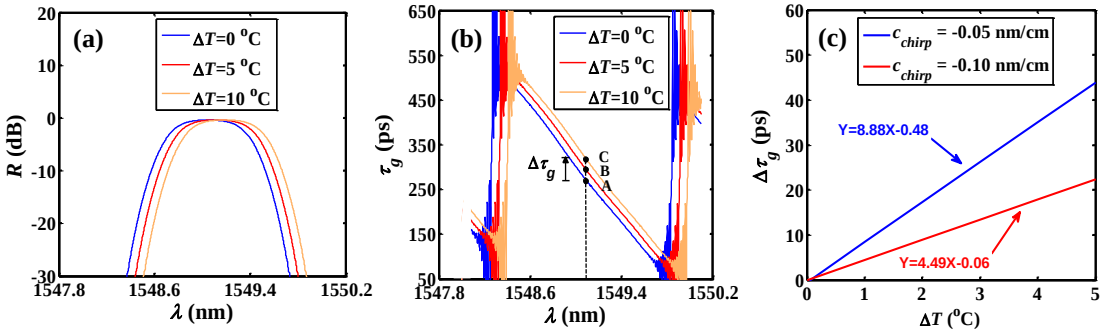

Figure 6.2: Numerical calculations of (a) reflection spectrum and (b) reflection group-delay spectrum of a LC-FBG as the temperature increases; (c) numerically calculated relative reflection group-delay as a function of temperature variation for two chirped FBGs.

Figure 6.2(a) and (b) present the calculated reflection and group-delay spectra of a LC-FBG with the parameters in Table 6.1 for $\Delta T=0$, 5, and 10 °C. Both the reflection and the group-delay spectra maintain their shapes but shift toward longer wavelengths as the temperature increases. The shift of the group-delay spectrum leads to a variation in the group-delay at a given wavelength. Figure 6.2(c) presents the numerically calculated relative reflection group-delay $\Delta\tau_g$ at an arbitrary

wavelength $\lambda = 1549.1$ nm as ΔT varies from 0 ^{o}C to 5 ^{o}C in steps 1 ^{o}C. The calculated $\Delta\tau_g$ increases linearly with ΔT in agreement with Eq. (6.6). Figure 6.2(c) also presents the calculated $\Delta\tau_g$ as a function of ΔT for $c_{chirp} = -0.05$ nm/cm. The slope $d\Delta\tau_g / d\Delta T$ doubles as c_{chirp} is changed from -0.10 nm/cm to -0.05 nm/cm, which confirms that $\Delta\tau_g$ is inversely proportional to $|c_{chirp}|$ as indicated by Eq. (6.6).

Table 6.1: Parameters of chirped FBG in the simulation.

Parameters	Value
Length of the grating (L: cm)	6
Effective refractive index (n_{eff})	1.452
Modulation depth ($\delta n_{eff\,0}$)	1.5×10^{-4}
Central wavelength (λ : nm)	1549
DC coupling coefficient (σ)	0
Chirp rate (c_{chirp} : nm/cm)	-0.1
Fringe visibility (ν)	1

6.3 Temperature sensing using a Kerr phase-interrogator

6.3.1 Experimental setup

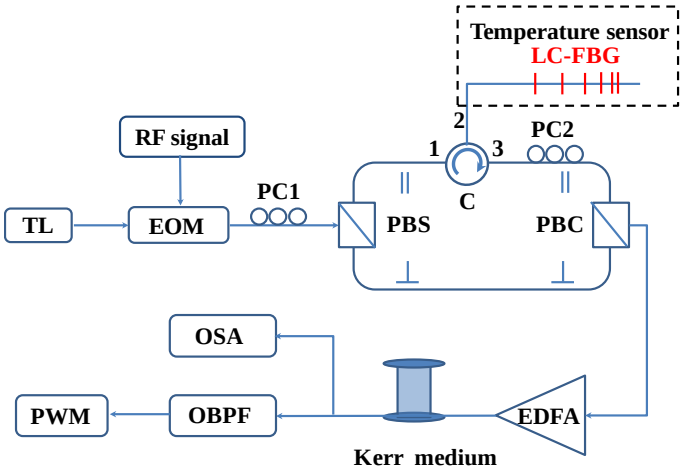

Figure 6.3: Kerr phase-interrogator setup for temperature sensing in LC-FBGs. TL: tunable laser; EOM: electro-optic modulator; PC: polarization controller; PBS: polarization beam splitter; C: circulator; LC-FBG: linearly chirped fiber Bragg grating; PBC: polarization beam combiner; EDFA: erbium-doped fiber amplifier; OSA: optical spectrum analyzer; OBPF: optical band-pass filter; PWM: power meter.

Figure 6.3 presents a schematic of the Kerr phase-interrogator configured for temperature sensing in a LC-FBG. A continuous-wave tunable laser (Agilent 81980A) with wavelength λ is amplitude modulated by an electro-optic modulator (EO-Space) at a modulation frequency $f_m = 10$ GHz to obtain SMOSs that oscillates at $f_s = 2 f_m$. The output of the modulator is split by a polarization beam splitter into parallel and perpendicular components propagating in a sensor path and a reference path, respectively. A LC-FBG is connected to the sensor path using an optical circulator and is used as a temperature sensor. The SMOSs from the sensor path and a reference path are recombined using a polarization beam-combiner. A polarization

controller (PC2) ensures equal powers for the two orthogonally polarized components after recombination. Amplified by an Erbium-doped fiber amplifier (Amonics AEDFA-33-B-FA), the combined signal is launched into a Kerr medium comprised of a dispersion-shifted fiber with a zero dispersion wavelength at $\lambda = 1552$ nm, a length L_{Kerr}=2.27 km and waveguide nonlinearity $\gamma = 2.28$ W^{-1}/km.

The power of the first-order sideband generated in the Kerr medium is given by

$$P_1 = P_1^{max} \cos^2\left(2\pi f_m \Delta\tau_g + \phi_0\right) \tag{6.8}$$

for $4\gamma L_{Kerr} P_P / 9 < 0.4$, where P_P =20mW is total peak power of the orthogonal components of the combined signal, P_1^{max} is the maximum value that P_1 attains, and ϕ_0 is a constant. The phase variation of the SMOS that is reflected from the LC-FBG is linearly proportional to the variation of the relative reflection group-delay and is given by $\Delta\phi = 2\pi f_m \Delta\tau_g$. Using Eq. (6.6), the variation in the phase of the SMOS becomes

$$\Delta\phi = -\frac{4\pi f_m \left(\beta + \alpha\right)\Lambda_z}{v_g c_{chirp}} \Delta T \tag{6.9}$$

leading to

$$P_1 = P_1^{max} \cos^2\left[-\frac{4\pi f_m \left(\beta + \alpha\right)\Lambda_z}{v_g c_{chirp}} \Delta T + \phi_0\right] \tag{6.10}$$

which indicates that P_1 varies sinusoidally with temperature. Figure 6.4 presents numerical simulation of the normalized power P_1 / P_1^{max} at the output of the Kerr phase-interrogator as a function of temperature change. Also presented in Fig. 6.4 is the normalized power calculated using Eq. (6.10) showing close agreement between the analytical and the numerical models.

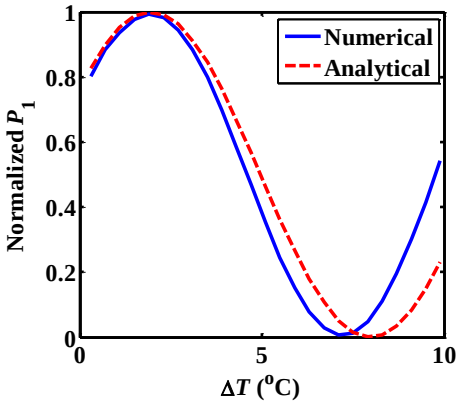

Figure 6.4: Numerical and analytical calculations of the normalized powers of the first-order sideband at the output of the Kerr phase-interrogator as a function of temperature variation.

6.3.2 Experimental results

The reflection and the reflection group-delay spectra of the LC-FBG that is used for temperature sensing are experimentally characterized. Figure 6.5(a) presents the reflection spectrum measured by launching amplified spontaneous emission noise from an EDFA into the LC-FBG and acquiring the optical spectrum of the reflected signal using an optical spectrum analyzer (Yokogawa AQ6370C). To characterize the reflection group-delay spectrum of the chirped grating, the laser wavelength is scanned over the flat part of the reflection spectrum from 1548.442 nm to 1548.656 nm in steps of 0.002 nm. The reflection group-delay of the LC-FBG changes as the laser wavelength is scanned leading to a variation of P_1 as indicated by Eq. (6.10). Optical spectra at the output of the Kerr medium are measured using an optical spectrum analyzer and the value of P_1 is recorded for each laser wavelength leading to $P_1(\lambda)$ as presented in Fig. 6.5(b). The wavelength values at the local maxima and minima of P_1 for which the relative phase $\Delta\phi = 2\pi f_m \Delta\tau_g$ is an integer

multiple of $\pi/2$ are recorded to obtain $\Delta\phi(\lambda)$. The spectrum of the relative reflection group-delay is then calculated from the $\Delta\phi(\lambda)$ using $\Delta\tau_g(\lambda) = \Delta\phi(\lambda)/2\pi f_m$ and the result is presented in Fig. 6.5(c).

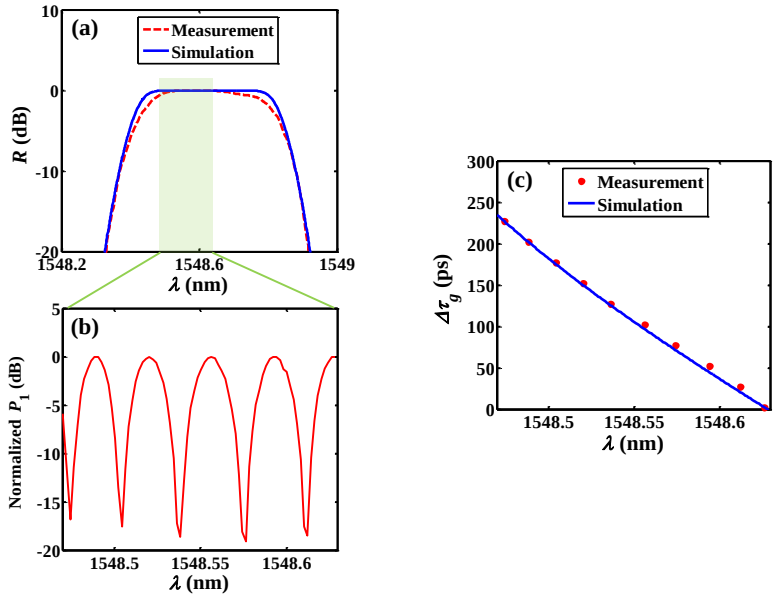

Figure 6.5: Experimental measurements of (a) the reflection spectrum of the LC-FBG, (b) the wavelength dependent P_1, and (c) the relative reflection group-delay spectrum of the LC-FBG.

The parameters of the LC-FBG are obtained by fitting the numerically calculated $R(\lambda)$ and $\Delta\tau_g(\lambda)$ obtained using the piecewise-uniform approach [52] with the experimentally measured spectra. Table 6.2 presents the parameters of the LC-FBG obtained from the fitting process. Figure 6.5(a) and (c) present the numerically calculated $R(\lambda)$ and $\Delta\tau_g(\lambda)$ showing close fit with the experimentally measured values.

Table 6.2: Parameters of the LC-FBG used in the experiment.

Parameters	Value
Length of the grating (L: cm)	13
Effective refractive index (n_{eff})	1.452
Modulation depth ($\delta n_{eff\,0}$)	1.5×10^{-4}
Central wavelength (λ : nm)	1548.65
DC coupling coefficient (σ)	0
Chirp rate (c_{chirp} : nm/cm)	-0.021
Fringe visibility (ν)	1

The wavelength of the laser source is fixed at 1548.57 nm and the OSA is replaced by an optical band-pass filter with a 3-dB bandwidth of 3 GHz (TeraXion TFC) followed by a power meter (Agilent/HP 81536A) to separate and measure the power of the first-order sideband. The LC-FBG is immersed in a water bath to ensure smooth variation and uniform distribution of temperature along the grating. The temperature of the water bath is increased to 34 ^{o}C, and then, is left to decrease to 30 ^{o}C over duration of 17 minutes. As water temperature decreases, P_1 as a function of time t is measured using the power meter and the corresponding water temperature is measured using a commercial electrical temperature sensor (Omega KMTXL-020G-6 with CNi3244-C24) that has a temperature resolution of 0.1 ^{o}C. Figure 6.6(a) presents the measured P_1 and T as a function of time t leading to $P_1(T)$ in Fig. 6.6(b). Figure 6.6(b) also presents the numerically calculated $P_1(T)$ obtained using the numerical model with the experimentally measured LC-FBG parameters in Table 6.2,

$\alpha = 7\times10^{-6}$ /°C, and $\beta = 5\times10^{-7}$ /°C showing close agreement with the experimental results.

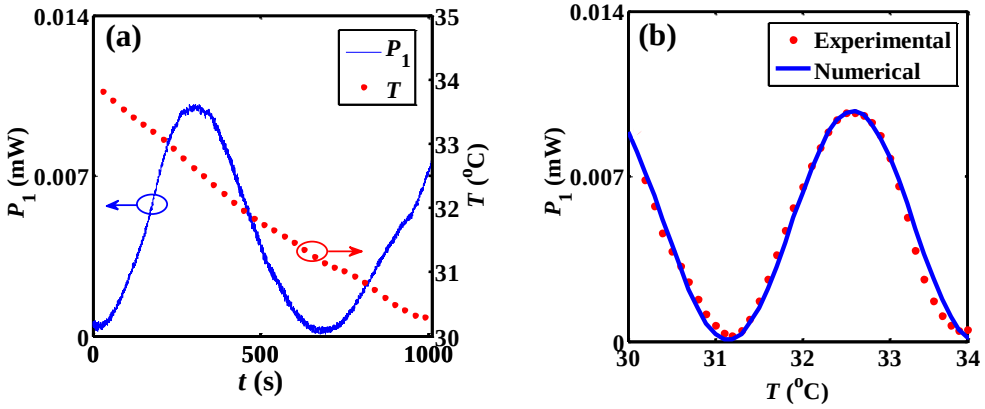

Figure 6.6: (a) Experimentally measured P_1 as a function of time as the temperature in the water bath is decreasing, and (b) experimentally measured and numerically calculated values of P_1 as a function of temperature.

6.4 Discussion

Temperature sensitivity is given by the rate of change of the phase with respect to temperature variation, $\rho_\phi = \Delta\phi / \Delta T$. Figure 6.6(b) shows that a temperature change of 2.8 °C induces π phase-shift leading to $\rho_\phi = 1.122$ rad/°C. The temperature sensitivity is theoretically estimated by rearranging Eq. (6.9) to obtain $\rho_\phi = -4\pi f_m (\alpha + \beta)\Lambda_T / v_g c_{chirp}$. Using $\lambda = 1550$ nm and $n_{eff} = 1.452$ in Eq. (6.2) results in $\Lambda_T = 534$ nm, and using $f_m = 10$ GHz, $\alpha = 7\times10^{-6}$ /°C, $\beta = 5\times10^{-7}$ /°C, $v_g = 2\times10^8$ m/s, and $c_{chirp} = -0.021\times10^{-7}$, the calculated temperature sensitivity is $\rho_\phi = 1.198$ rad/°C in close agreement with the measured value. The temperature resolution δT of the proposed temperature sensor is limited by the minimum detectable phase-change $\delta\phi$ of the Kerr phase-interrogator. The value of $\delta\phi$ is limited by the fluctuations of P_1 which arise from intensity-noise of the laser,

shot-noise of the photo-detector, and amplified spontaneous-emission noise of the EDFA. Using $\delta\phi = 0.01$ rad at the quadrature points and $\rho_\phi = 1.122$ rad/^{o}C leads to a temperature resolution of $\delta T = \delta\phi / \rho_\phi = 0.0089$ ^{o}C [39]. Both temperature sensitivity and resolution can be optimized by increasing f_m and reducing $|c_{chirp}|$. Furthermore, the value of $\delta\phi$ can be reduced to enhance the temperature resolution by utilization of a laser with low intensity-noise, a highly nonlinear Kerr-medium to eliminate the need for the EDFA, and a low noise photo-detector. Such high-sensitivity temperature measurement is critical for high-precision temperature control and week-temperature-variation monitoring, and will benefit aerospace industry, biomedicine and numbers of other research and industry fields.

The dynamic-range T_{DR} refers to the temperature range within which the proposed approach based on a Kerr phase-interrogator can measure, and is limited by the shift of the reflection spectrum with temperature, which is observed in Fig. 6.2(a), and the finite width of the flat section in the reflection spectrum of the LC-FBG. Differentiation of Eq. (6.2) with respect to T leads to an estimate of the rate of spectrum shift $\rho_{shift} = d\lambda / dT = 2n_{eff}\Lambda_T(\alpha + \beta) = 0.0116$ nm/^{o}C. The width of the optical spectrum of the SMOS is given by $\Delta\lambda_s = 2f_m\lambda^2 / c = 0.16$ nm and the width of the flat section of the reflection spectrum is $\Delta\lambda_{flat} = 0.3$ nm leading to a maximum allowed reflection spectrum shift of $\Delta\lambda_{shift}^{max} = \Delta\lambda_{flat} - \Delta\lambda_s = 0.14$ nm and a dynamic-range of $T_{DR} = \Delta\lambda_{shift}^{max} / \rho_{shift} = 12.06$ ^{o}C. The dynamic-range can be increased by using a LC-FBG with a broad flat reflection spectrum to increase $\Delta\lambda_{shift}^{max}$. In this case, the dynamic-range is broader and is limited by the temperature at which the

LC-FBG is erased [53, 54].

Limitation of temperature sensing to the linear range T_{LR} over which P_1 varies from $0.2P_1^{max}$ to $0.8P_1^{max}$ restricts the dynamic range to $T_{DR} \le T_{LR}$. Figure 6.6(b) shows that $P_1 = 0.2P_1^{max}$ at $T = 31.5\,^{o}\text{C}$ and $P_1 = 0.8P_1^{max}$ at T=32.2 ^{o}C leading to $T_{LR} = 0.7\,^{o}\text{C}$. The value of T_{LR} is analytically estimated from Eq. (6.10) to be $T_{LR} \approx v_g\,|c_{chirp}|/16 f_m(\beta+\alpha)\Lambda_z$. Using $v_g = 2\times10^8$ m/s, $c_{chirp} = -0.021\times10^{-7}$, $f_m = 10\,\text{GHz}$, $\alpha = 7\times10^{-6}\,/^{o}\text{C}$, and $\beta = 5\times10^{-7}\,/^{o}\text{C}$ leads to $T_{LR} = 0.67\,^{o}\text{C}$ in close agreement with the measured value.

7 Chromatic-dispersion monitor using a Kerr phase-interrogator

This chapter presents a novel approach for real-time chromatic-dispersion (CD) monitoring using a Kerr phase-interrogator. CD induces a phase-shift between two sinusoidally-modulated optical signals (SMOS) carried by two different wavelengths. A Kerr phase-interrogator converts the phase-shift into power variation and CD monitoring is achieved by measurement of the power variation in real time.

7.1 Background

Real-time CD monitoring is practical for automated CD compensation in high bit-rate and long-distance optical transmission systems [55]. Due to temperature and strain dependence of CD in optical fibers and chirped fiber Bragg gratings [56-59], CD monitors can be used for sensing applications. CD monitoring has been achieved using asynchronous amplitude sampling techniques and histogram evaluation approaches [60-62] where CD is acquired from statistical properties of the monitored optical signal. Time-consuming signal processing makes these statistical approaches impractical for real-time monitoring. Signal-modulation based approaches have also been used for monitoring CD by measurement of the peak-to-peak values of the amplitude modulated (AM) pilot tones [63-65], or the phase difference between the upper and lower sidebands of the AM pilot tones [66]. Signal-modulation approaches

require broad-band detector to obtain the AM pilot tones and special electronic circuits such as phase-locked loops for signal processing, leading to complex signal acquisition and bandwidth limitations.

A Kerr phase-interrogator is capable of measuring phase-shift between two SMOSs. Because the phase-shift of SMOSs carried by different wavelengths is linearly proportional to the CD in the propagation path of the two SMOSs, the Kerr phase-interrogator can monitor CD variations allowing for novel sensing applications. In comparison with existing approaches, CD monitoring is achieved by a mere power measurement at the output of the Kerr phase-interrogator without additional signal-processing allowing for measurement of fast CD variations and consequently real-time CD monitoring.

In this chapter, we propose and experimentally demonstrate a novel approach for real-time CD monitoring by a phase-shift method using a Kerr phase-interrogator. A Kerr phase-interrogator setup is configured for real-time CD monitoring by utilization of two orthogonally polarized SMOSs that are carried by two different laser wavelengths. Real-time CD monitoring by measurement of the power of the first-order sideband is experimentally demonstrated.

7.2 Experimental setup and results

7.2.1 Experimental setup

Figure 7.1 (a) shows the Kerr phase-interrogator configured for CD monitoring. Two continuous-wave lasers (Agilent 81980A) operating at wavelengths $\lambda_{j=1,2}$ are

amplitude-modulated by an electro-optic modulator (EO-Space) and a sinusoidal electrical signal generator (HP 83752A) at a radio frequency f_m. The outputs of the modulator are two SMOSs oscillating at a frequency $f_s=2f_m$. The optical spectrum for each SMOS consists of two distinct peaks separated by $\Delta\lambda_s = (\lambda_1^2 / c) f_s \approx (\lambda_2^2 / c) f_s$ with c being speed of light in vacuum, as illustrated in Fig. 1(b). The modulated signals then propagate through a tunable CD emulator (TDC-109181917) that induces an accumulated CD equivalent to $D_c \times L = t_d / \Delta\lambda_l$ where D_c is the CD parameter, L is the propagation distance, $t_d = t_2 - t_1$ is group-delay difference of two SMOSs induced by CD emulator with t_j being the group-delay accumulated by the SMOS carried by the laser carrier at λ_j, and $\Delta\lambda_l = \lambda_2 - \lambda_1$ is the laser carrier separation. The SMOSs are separated using a fiber Bragg grating and a circulator, and then recombined using a polarization beam combiner to obtain two orthogonally polarized SMOSs. Two polarization controllers, PC1 and PC2, ensure the powers of the parallel and perpendicular components of the combined signal are maximum and equal. The combined signal is amplified by an Erbium-doped fiber amplifier (Amonics AEDFA-33-B-FA) and then launched into a Kerr medium comprised of a dispersion-shifted fiber with a zero dispersion wavelength at $\lambda = 1552$ nm, a length L_{Kerr}=2.27 km and waveguide nonlinearity $\gamma = 2.28$ W^{-1}/km.

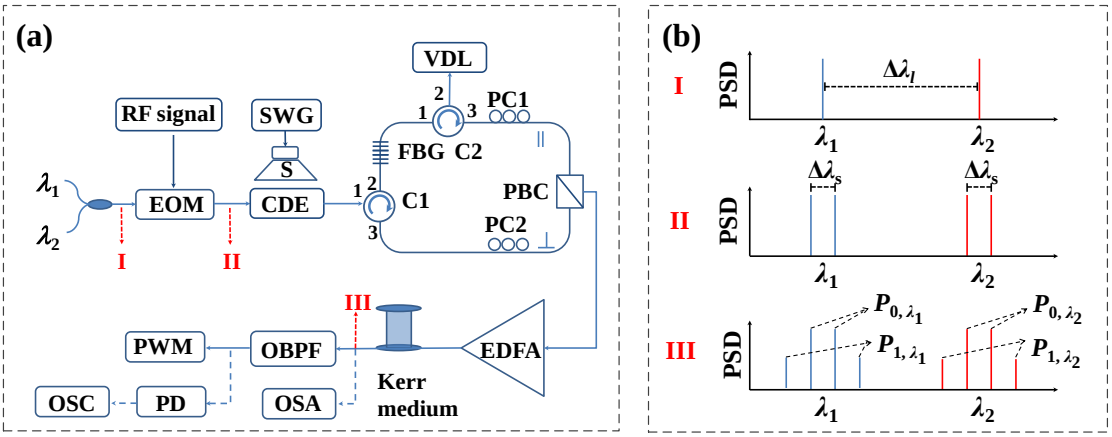

Figure 7.1: (a) Schematic of the CD monitoring setup based on a Kerr phase-interrogator, and (b) illustrations of the optical spectra at different points of the setup. EOM: electro-optic modulator; RF: radio frequency; CDE: chromatic-dispersion emulator; SWG: sinusoidal waveform generator; S: speaker; C: circulator; FBG: fiber Bragg grating; PC: polarization controller; VDL: variable delay line; PBC: polarization beam combiner; EDFA: erbium-doped fiber amplifier; OBPF: optical band-pass filter; OSA: optical spectrum analyzer; PWM: power meter; PD: photodiode; OSC: oscilloscope; PSD: power spectral density.

The amplitude of the SMOS carried by λ_j at the input of the Kerr medium is given by

$$A_j = \sqrt{\frac{P_p}{2}} \cos\left[\pi f_s \left(t - t_j\right)\right] \tag{7.1}$$

where P_P=20mW is the total peak power of the combined signal. Neglecting CD effects in the Kerr medium, the evolutions of the SMOSs in a low-birefringent fiber with random birefringence are governed Eq. (3.3) leading to $A_j\left(L_{Kerr}\right) = A_j\left(0\right)\exp\left(i\phi_{NL}\right)$ at output of Kerr medium, where

$$\phi_{NL} = \frac{4P_p \gamma L_{Kerr}}{9}\left\{\cos^2\left[\pi f_s\left(t-t_1\right)\right] + \cos^2\left[\pi f_s\left(t-t_2\right)\right]\right\} \ . \tag{7.2}$$

The phase modulation ϕ_{NL} leads to the formation of distinct sidebands P_k with k=1,2,..., as illustrated in Fig. 7.1(b). The value of P_1 is derived analytically as described in chapter 2 to obtain

$$P_1 = P_1^{max} \cos^2\left(\pi f_s D_c \Delta\lambda_l L + \phi_0\right) \tag{7.3}$$

for $4\gamma L_{Kerr} P_P / 9 < 0.2$, where P_1^{max} is the maximum value of P_1.

7.2.2 Experimental results

The operating wavelengths of the lasers are set to $\lambda_1 = 1550.05$ nm and $\lambda_2 = 1550.91$ nm, and the modulation frequency is set to f_m=9 GHz. The accumulated CD is varied from -617 ps/nm to -641 ps/nm in steps of 6 ps/nm and the spectrum of the signal at the output of the Kerr medium is measured by an optical spectrum analyzer (Yokogawa AQ6370C). Figure 7.2(a) presents the evolution of the measured spectra at the output of Kerr medium as the accumulated CD is varied and Fig. 7.2(b) presents a magnified image of the generated first-order sideband. The first-order sideband is extracted by a band-pass filter (TeraXion TFC) with a 3 dB bandwidth of 3 GHz and a power-meter (Agilent/HP 81536A) is used for measurement of P_1 as the accumulated CD is varied. Figure 7.2(c) presents the measured values of normalized power P_1 / P_1^{max} as the accumulated CD is varied between -644 ps/nm and -584 ps/nm in steps of 3 ps/nm. Also presented in Fig. 7.2(c) is the normalized power calculated using Eq. (7.3) showing close agreement with experimental values.

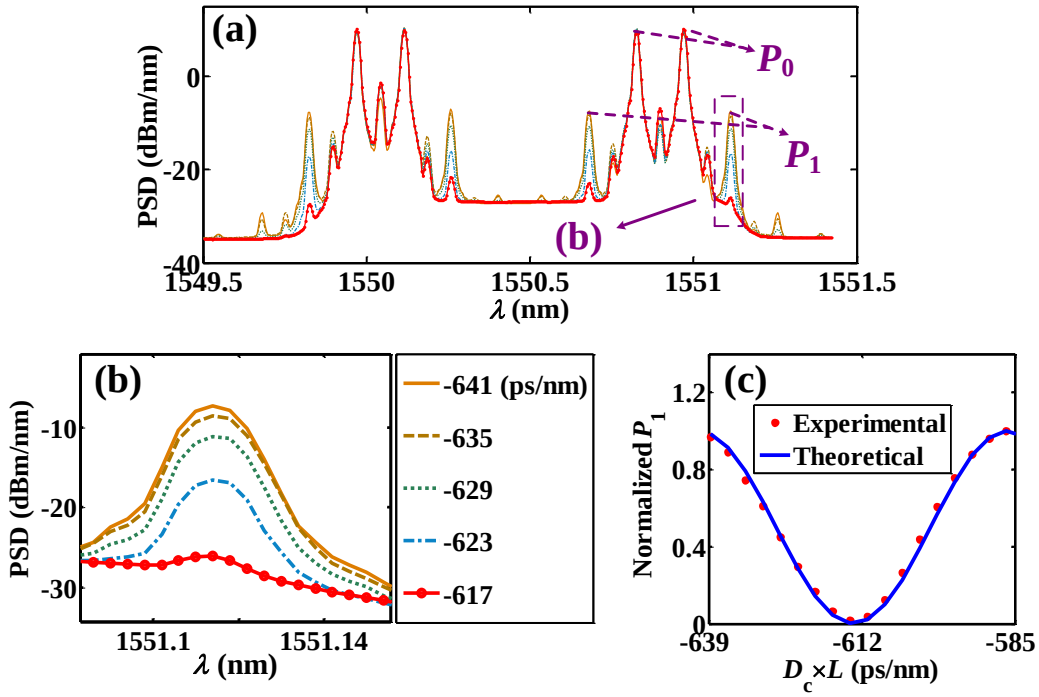

Figure 7.2: (a) Measured spectra at the output of the Kerr medium, and (b) a magnified image of the first-order sideband; (c) experimentally measured and theoretically calculated values of normalized power P_1/P_1^{max} as a function of the accumulated CD.

The power-meter is replaced by a photodiode that is connected to an electrical oscilloscope (Agilent DSO81204B) to record the real-time value of P_1 as the accumulated CD is varied. The accumulated CD is varied by a step of 3 ps/nm every minute in the range between -633 ps/nm and -624 ps/nm where P_1 has quasi-linear dependence on the accumulated CD. Figure 7.3(a) presents the measured trace of P_1 as a function of time showing correspondence between P_1 and the accumulated CD, and power fluctuation in the measured trace arises from the CD-fluctuation from the emulator.

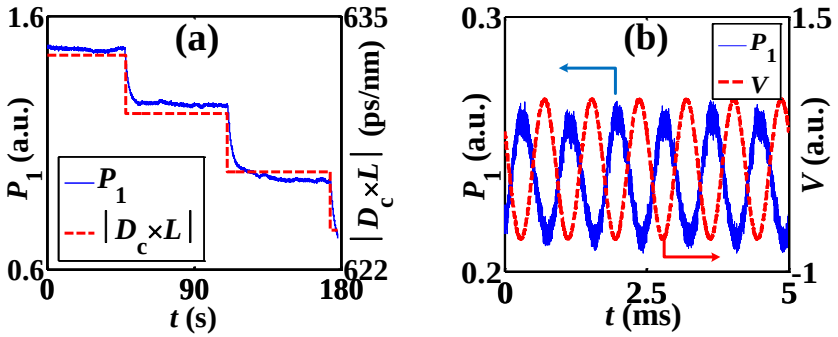

Figure 7.3: (a) Measured trace of P_1 as a function of time as $|D_c \times L|$ decreases in steps of 3 ps/nm every minute, and (b) measured trace of P_1 as a function of time showing the vibration induced variation in $|D_c \times L|$.

A speaker is placed on top of the CD emulator and is driven with a sinusoidal waveform generator at a frequency of 1.2 kHz. The acoustic wave from the speaker induces mechanical vibrations in the chirped fiber Bragg grating of the CD emulator leading to periodic variation of the accumulated CD. Real-time variation of the accumulated CD is monitored by measurement of the sideband power $P_1(t)$. Figure 7.3(b) presents the measured trace of $P_1(t)$ with a trace of the voltage that is used to drive the speaker showing correlation between these two signals.

7.3 Discussion

7.3.1 Resolution

The resolution of the proposed CD monitor is determined by the minimum resolvable phase-shift $\alpha = \pi f_s D_c \Delta\lambda_l L$. Differentiation of Eq. (7.3) leads to $|\delta\phi \sin(2\phi)| = |\delta P_1 / P_1^{max}|$, where $\phi = \pi f_s D_c \Delta\lambda_l L$, $\delta\phi$ and δP_1 represent fluctuations of phase-shift and power, respectively. Around the quadrature points at $\phi = \pi/4 + m\pi/2$ where m is an integer, the phase fluctuation is given by

$|\delta\phi| = |\delta P_1 / P_1^{max}|$. The minimum resolvable phase-shift $\alpha = \max\{|\delta\phi|\}$ can be verified experimentally from the power fluctuations $|\delta P_1 / P_1^{max}|$. Figure 7.4(a) presents a measured trace of normalized P_1 as a function of time where the accumulated CD is fixed at -628 ps/nm over a duration of 33 s and then is changed abruptly by 100 ps/nm. Figure 7.4(b) presents a magnified image of the measured trace showing that $|\delta P_1 / P_1^{max}| < 0.01$ leading to $\alpha = 0.01$ rad round quadrature points. Using f_s=18 GHz, $\Delta\lambda_1 = 0.9$ nm, and $\alpha = 0.01$ rad leads to a CD monitor resolution of 0.196 ps/nm.

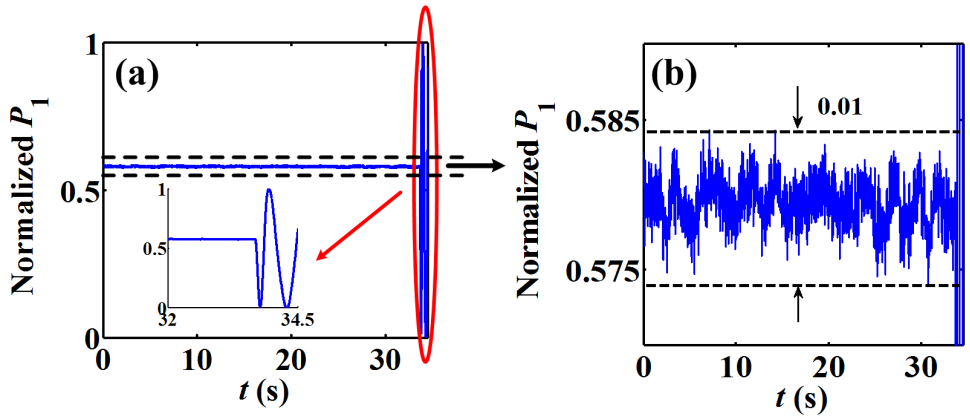

Figure 7.4: (a) Measured trace of P_1/P_1^{max} as a function of time with an inset showing the full power swing that results from changing $|D_c \times L|$ by 100 ps/nm, and (b) a magnified image showing the fluctuation of the normalized power when $|D_c \times L|$ is unchanged.

Fluctuations of P_1 are induced by the noise in the peak power P_P of the combined SMOS at the input of the Kerr medium. The peak power noise arises from the intensity-noise of the laser and the amplified spontaneous-emission noise of the EDFA. Peak power noise also arises from external mechanical and thermal disturbances that cause birefringence variation in the monitored device which induce polarization variation on SMOSs before PBC. The noise of P_P induces variations to

$P_p \gamma L_{Kerr}$ which lead to fluctuations δP_1 in the power of the first-order sideband. Shot-noise and dark-current noise of the photo-detector further increase the magnitude of δP_1. The resulting δP_1 leads to phase fluctuations $|\delta\phi| = |\delta P_1 / P_1^{max}|$, which limit the minimum resolvable phase-shift α, and consequently, limit the finesse of the achievable resolution. The magnitude of δP_1 can be reduced by utilization of a laser with low intensity-noise, a highly nonlinear Kerr-medium to eliminate the need for the EDFA, and a low noise photo-detector. Furthermore, external disturbances that cause polarization variation are relatively slow and their contribution to δP_1 can be eliminated by using a feedback control-system that corrects the polarization of the SMOSs before the PBC.

7.3.2 Dynamic-range

The dynamic-range $\{D_c \times L\}_{DR}$ refers to the range of CD variation within which the proposed approach based on a Kerr phase-interrogator can monitor, and is not limited by the equipment that comprises the CD monitor. In practice, a value of P_1 corresponds to multiple values of the accumulated CD due to the sinusoidal variation of P_1 with $D_c \times L$. To avoid post-measurement signal processing and obtain a one-to-one correspondence between P_1 and $D_c \times L$, the dynamic-range $\{D_c \times L\}_{DR}$ is restricted within the quasi-linear range over which P_1 varies from $0.2\,P_1^{max}$ to $0.8\,P_1^{max}$ around the quadrature points. Figure 7.2(c) shows that $P_1 = 0.2P_1^{max}$ at $D_c \times L = -621.0$ ps/nm and $P_1 = 0.8P_1^{max}$ at $D_c \times L = -633.5$ ps/nm leading to $\{D_c \times L\}_{DR} = 12.5$ ps/nm. The value of $\{D_c \times L\}_{DR}$ is estimated from Eq. (7.3) to be $\{D_c \times L\}_{DR} \approx 1/4 f_s \Delta\lambda_l$. Using f_s=18 GHz and $\Delta\lambda_l = 0.9$ nm leads to

$\{D_c \times L\}_{DR} = 15.4$ ps/nm in close agreement with the measured value.

8 Incoherent optical frequency domain reflectometry based on a Kerr phase-interrogator

This chapter presents a novel approach for incoherent optical frequency-domain reflectometry (I-OFDR) based on a frequency-swept sinusoidally-modulated optical signal (SMOS) and a Kerr phase-interrogator. The novel approach eliminates dependence on the laser coherence-length allowing for long-range operation.

8.1 Background

Optical frequency-domain reflectometry (OFDR) is one of the most popular approaches for high-resolution fault allocation [67], optical fiber component characterization [67-70], and distributed temperature and strain sensing [71]. Coherent optical frequency domain reflectometry (C-OFDR) utilizes a tunable laser and an interferometer to superpose a swept-laser signal with a time-delayed version of the same signal leading to a beat [67]. Spectral analysis of the beat signal allows for the location of reflection points along a laser path at high spatial-resolution and high dynamic-range [67, 68, 72]. The utilization of an interferometer makes C-OFDR highly dependent on the laser coherence properties limiting the range of reflection detection [67]. Several approaches have been used for range extension in C-OFDR. Utilization of a highly-coherent swept-laser implemented using a narrow linewidth fiber laser and a piezoelectric tuner has allowed for the location of Fresnel reflection

from the end of a 95 km long fiber at an unspecified spatial-resolution [73]. Phase-noise-compensation has allowed for the location of reflection points as far as 80 km at a spatial-resolution of 20 cm [74]. Band-width division has been combined with phase-noise-compensation to locate reflections as far as 40 km at an improved spatial-resolution of 5 cm [75]. Most recent, phase-noise measurement for a swept-laser reflected from points beyond the laser coherence length has allowed the location of Fresnel reflections as far as 170 km at a spatial resolution of 200 m [76].

I-OFDR has been investigated as an alternative for C-OFDR because it intrinsically allows for long-range reflection measurements [77-79]. In I-OFDR, the beat between a frequency-swept SMOS and a time-delayed version of the same signal determines the location of reflection points along the signal path. Existing implementations of I-OFDR utilize opto-electronic components and electronic signal processors for beat acquisition. Unfortunately, the bandwidth cap of electronic and opto-electronic devices limits the maximum sweep frequency-span and the minimum achievable spatial-resolution. The bandwidth cap can be eliminated by development of an all-optical approach for beat acquisition. A Kerr phase-interrogator can be utilized for all-optical beat acquisition which will potentially allow for long-range I-OFDR at micron-level spatial-resolution.

In this chapter, a novel approach for I-OFDR based on Kerr phase-interrogator is presented. The I-OFDR setup based on a Kerr phase-interrogator and frequency-swept SMOS is presented first. Theoretical analysis shows that the output of the Kerr phase-interrogator corresponds to the beat of the powers of orthogonally-polarized

frequency-swept SMOSs. Utilization of the novel I-OFDR approach for the location of reflection points on a fiber is experimentally demonstrated.

8.2 Experimental setup and results

8.2.1 Experimental setup

Figure 8.1 (a) shows the Kerr phase-interrogator configured for I-OFDR. A continuous-wave (CW) laser (Agilent 81980A), illustrated in Fig. 8.1(b), is amplitude-modulated using an electro-optic modulator (EO-Space) and a sinusoidal electrical signal generator (HP 83752A) with a time-varying frequency $f_m(t)=0.5(f_0+\rho t)$. The output of the modulator is a SMOS with a frequency $f_s(t)=f_0+\rho t$, and the optical spectrum of this SMOS is composed of two distinct peaks with time-varying separation $\Delta\nu=f_s(t)$ where ν is the optical frequency, as illustrated in Fig. 8.1(c). The power of the SMOS is split using a polarization beam splitter into a sensor path and a reference path corresponding to the parallel and perpendicular components, respectively. A circulator connects a fiber under test (FUT) that is terminated with a reflector to the sensor path. The signals from the reference and the sensor paths are recombined using polarization beam combiner (PBC). Figure 8.1(d) illustrates the spectrum and the time-trace of the combined signal at the output of the PBC.

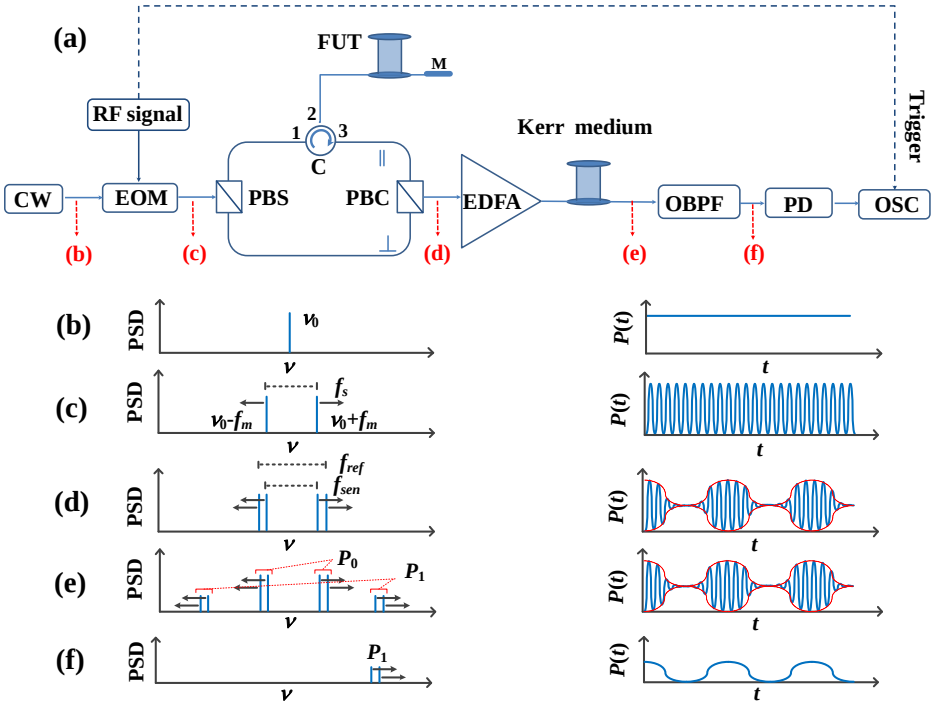

Figure 8.1: Schematic of (a) the I-OFDR setup based on a Kerr phase-interrogator, and illustrations of the spectrum and the power trace of (b) the CW laser signal, (c) the sinusoidal laser signal, (d) the combined reference and reflected SMOSs, (e) the phase-modulated SMOS, and (f) the filtered side-band. RF: radio-frequency; CW: continuous wave; EOM: electro-optic modulator; C: circulator; FUT: fiber under test; PBS: polarization beam splitter; PBC: polarization beam combiner; EDFA: Erbium-doped fiber amplifier; OBPF: optical band-pass filter; PD: photo-diode; OSC: oscilloscope; PSD: power spectral density.

The parallel and perpendicular components at the output of the PBC are given by $A_{\perp} = \sqrt{P_P/2}\cos\left(\pi f_{ref} t + \phi_{\perp}\right)$, $A_{\parallel} = \sqrt{P_P/2}\cos\left(\pi f_{sen} t + \phi_{\parallel}\right)$, where $\phi_{\perp} = -\pi f_{ref} t_{\perp}$, $\phi_{\parallel} = -\pi f_{sen} t_{\parallel}$, $f_{ref} = f_0 + \rho\left(t - t_{\perp}\right)$, and $f_{sen} = f_0 + \rho\left(t - t_{\parallel}\right)$ with $t_{\perp}$ and $t_{\parallel}$ being the delay-times required for the SMOSs to travel the reference and the sensor paths, respectively. The combined signal at the output of the PBC is amplified using an Erbium-doped fiber amplifier (Amonics AEDFA-33-B-FA) and then launched into a 4 km long fiber with low chromatic dispersion D_c=3 ps/(nm×km), which serves as a Kerr medium. The amplitudes of the perpendicular and the parallel field components at the output of the Kerr medium become

$$A_{\perp} = \sqrt{\frac{P_P}{2}} \cos\left(\pi f_{ref} t + \phi_{\perp}\right) \exp\left[j8\gamma P(t) L_{Kerr} / 9 \right] \tag{8.1}$$

$$A_{\parallel} = \sqrt{\frac{P_P}{2}} \cos\left(\pi f_{sen} t + \phi_{\parallel}\right) \exp\left[j8\gamma P(t) L_{Kerr} / 9 \right] \tag{8.2}$$

where γ, L_{Kerr} are the waveguide nonlinearity and the length of the Kerr medium, respectively, and $P(t) = |A_{\perp}|^2 + |A_{\parallel}|^2$ is the combined power given by

$$P(t) = \frac{P_P}{2}\left[\cos^2\left(\pi f_{ref} t + \phi_{\perp}\right) + \cos^2\left(\pi f_{sen} t + \phi_{\parallel}\right) \right] \tag{8.3}$$

The Kerr-effect induced sinusoidal phase modulation of $A_{\perp}$ and $A_{\parallel}$ leads to the formation of distinct sidebands P_i with i=1, 2, 3,..., as illustrated in Fig. 8.1(e). The $P_1(t)$ is obtained analytically by applying the Jacobi–Anger expansion to Eqs. (8.1)–(8.2) leading to (see Appendix for the detailed expression)

$$P_1(t) = \frac{P_p}{8}\left\{ J_1^2\left[m\cos\left(\pi f_d t + \phi_{\Delta}\right)\right] + J_2^2\left[m\cos\left(\pi f_d t + \phi_{\Delta}\right)\right]\right\} \tag{8.4}$$

where $m = 4\gamma L_{Kerr} P_P / 9$, $\phi_{\Delta} = \phi_{\perp} - \phi_{\parallel} = -\pi f_d t_{\perp} + \pi\left(f_{ref} - f_d \right) t_d$, $f_d = f_{ref} - f_{sen} = \rho t_d$, and $t_d = t_{\parallel} - t_{\perp}$. Utilization of the multiplication theorem for Bessel functions as described in chapter 2 leads to

$$P_1(t) = P_1^{max} \cos^2\left(\pi f_d t + \phi_{\Delta}\right) \tag{8.5}$$

for m<0.2, where P_1^{max} is the maximum value that P_1 attains. Equation (8.5) shows that the output of the Kerr phase-interrogator corresponds to the beat of the powers of two orthogonally polarized SMOSs that oscillate at two different frequencies $f_{ref} \neq f_{sen}$. This beat depends only on the powers of the SMOSs allowing for I-OFDR implementation. For the special case $f_{ref} = f_{sen}$, Eq. (8.5) reduces to $P_1(t) = P_1^{max} \cos^2\left(\phi_{\Delta}\right) = P_1^{max} \cos^2\left(\pi f_{ref} t_d\right)$ which is identical to the relation derived in chapter 2. A band-pass filter (TeraXion TFC 3 GHz bandwidth) with a center

frequency at $\left(\nu_0 + 1.5\left(f_s^{max} + f_s^{min}\right)/2\right)$, where $\nu_0 = c/\lambda_0$ with c being the speed of light in vacuum, is placed at the output of the Kerr medium and is followed by a photo-detector (New-Focus 1811) that is connected to an oscilloscope (Agilent DSO81204B) to obtain a time-trace of $P_1(t)$.

8.2.2 Experimental results

A CW laser with a wavelength λ_0=1550.202 nm is amplitude-modulated using a Mach-Zehnder modulator and a sinusoidal electrical signal generator to obtain a SMOS with a frequency varying linearly from $f_s^{min} = 18.5$ GHz to $f_s^{max} = 19.5$ GHz over a duration of 50 ms leading to ρ=20 GHz/s. The FUT has a length of 2.2 km and is terminated with an ultra-polished connector (UPC) to induce Fresnel back reflection. Figure 8.2(a) presents the measured value of $P_1(t)$ at the oscilloscope, and Fig. 8.2(b) presents a magnified section of $P_1(t)$ showing a sinusoidal variation with time in agreement with Eq. (8.5). The spectrum of $P_1(t)$ is calculated using $\mathcal{F}\left\{P_1(t)\right\}$, where $\mathcal{F}$ is the Fourier transform operator, and then the frequency f is replaced by the distance $d = fc/2\rho n_g$, where n_g=1.46 is the group refractive index of the FUT, to obtain the relative reflectivity as a function of distance, as shown in Fig. 8.2(c). The signal $P_1(t)$ is zero-padded to increase the frequency resolution of the Fourier transform allowing for the determination of the spatial-resolution Δd_{3dB}=9.3 cm, as shown in Fig. 8.2(d).

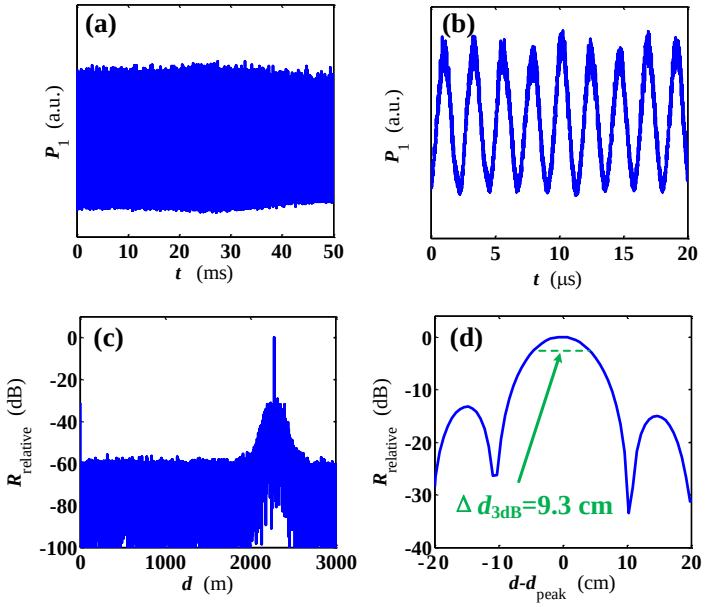

Figure 8.2: (a) Measured $P_1(t)$, (b) magnified section of $P_1(t)$, (c) relative reflectivity as a function of distance in the fiber under test, and (d) magnified section of the reflection at d_{peak}=2272.49278 m.

Similar to existing implementations of I-OFDR, the novel approach allows for the detection of multiple reflection points. Figure 8.3(a) presents the measured reflectivity as a function of distance for a combination of two fibers connected using non-matching fiber connectors, a UPC connector and an angle-polished connector (APC), to induce strong back-reflection at the interface between the two fibers. Reflection peaks are observed a d=2.2725 km and d=6.6480 km corresponding to the locations of end-facets of the first and the second fibers. Furthermore, the novel approach can detect reflection points on hundreds of kilometers of fiber. Figure 8.3(c) presents the measured reflection at the end of 151 km long fiber obtained with ρ=4 GHz/s. An erbium doped fiber amplifier is used for amplification of the signal reflected from the end of the 151 km long fiber to compensate for the attenuation induced by traveling along the fiber.

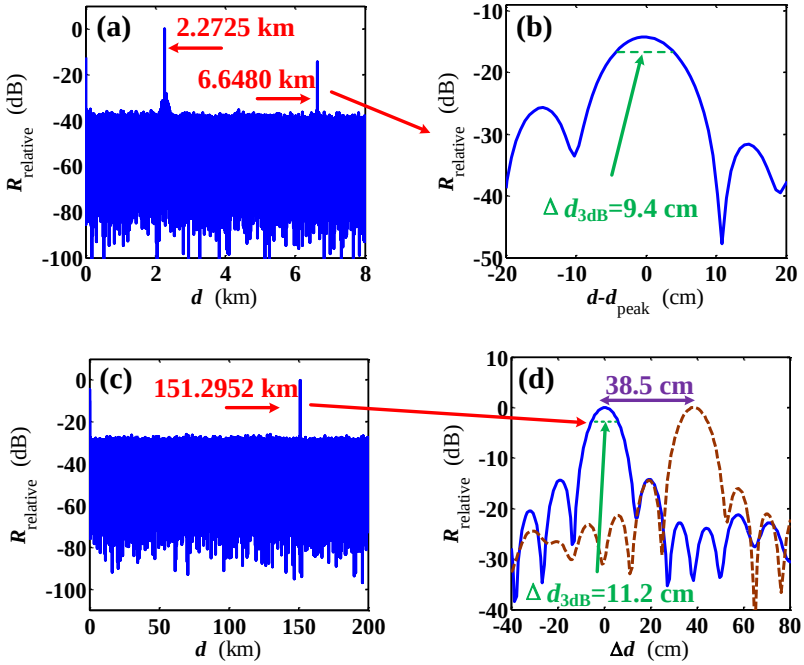

Figure 8.3: (a) Relative reflectivity for two concatenated fibers, (b) magnified image of the peak at d_{peak}=6.6480 km, (c) relative reflectivity for a 151 km long fiber, and (d) reflection peaks at the end of the 151 km fiber (solid curve) and at the end of a 37.4 cm fiber cord connected to the 151 km fiber (dashed curve).

8.3 Discussion

8.3.1 Spatial-resolution

The shortest distance between two reflection points to be located is determined by the spatial resolution of proposed approach based on a Kerr phase-interrogator. The frequency corresponding to a reflection point located at distance d is given by $f=2\rho d n_g/c$ leading to a spatial resolution $\Delta d=\Delta f c/2\rho n_g$. The spectrum of the measured time-trace $P_1(t)$ is a squared sinc function for which the 3 dB frequency resolution is calculated from the measured time-trace interval t_{span} using $\Delta f_{3\text{dB}}=0.88/t_{span}$ leading to $\Delta d_{3\text{dB}}=0.88c/2\rho n_g t_{span}$. Using ρ=20 GHz/s, n_g=1.46, and t_{span}=50 ms leads to $\Delta d_{3\text{dB}}$=9.04 cm in close agreement with the measured values at $\Delta d_{3\text{dB}}$=9.3 cm at

d=2.2725 km and Δd_{3dB}=9.4cm at d=6.6480 km, as shown in Fig. 8.2(d) and Fig. 8.3(b), respectively. To further investigate the spatial-resolution, Fig. 8.3(d) presents the reflection peak at the end of the 151 km fiber and the peak that results after connecting a 37.4 cm fiber cord at the 151 km fiber end. The 3 dB spatial-resolution for the peak at d=151.2952 km is Δd_{3dB}=11.2 cm showing that the spatial-resolution is maintained over long distances. Furthermore, the reflection peaks in Fig. 8.3(d) are clearly distinguishable and are separated by 38.5 cm in close agreement with the length of the fiber cord.

8.3.2 Dynamic-range

The measured signal is given by $P_1^{meas}(t)=\left[P_1^{ideal}(t)+\nu(t)\right]\times \mathrm{rect}(t)$ where $P_1^{ideal}(t)$ is the ideal signal, $v(t)$ is the noise, and rect(t) is a square pulse with a duration t_{span}. The signal-to-noise ratio (SNR) of $P_1^{meas}(t)$ can be increased by using a highly-nonlinear chalcogenide fiber as a Kerr medium to induce nonlinear Kerr effects at lower signal powers eliminating the need for optical amplifiers that generate noise through amplified spontaneous emission. The SNR can also be increased by using low-noise photo-diodes to reduce dark-current noise and shot-noise such that $P_1^{ideal}(t)\gg\nu(t)$. Finally, the SNR penalty induced by the finite measurement duration t_{span} is obtained from the normalized spectrum of rect(t) given by $\sin^2(\pi f t_{span})/(\pi f t_{span})^2$. Increasing the sweep frequency-span N times increases t_{span} by a factor N, and consequently, reduces the SNR penalty of rect(t) by a factor N^2.

Similar to C-OFDR, the power of the reflected signal must be weak in the presence of multiple reflectors to prevent the generation of artificial peaks that arise

from mixing of the frequencies corresponding to actual reflection peaks. Unfortunately, the dynamic-range, which refers to the farthest achievable reflection location, is reduced when the signal from the sensor path is weaker than the signal from the reference path. Enhancement of the dynamic-range is essential for the detection of Rayleigh back-scattering in the FUT allowing for distributed sensing of strain and temperature [71, 80]. Future work will focus on enhancement of the dynamic-range for the implementation of distributed temperature and strain sensors.

9 Summary and future work

9.1 Summary

In this thesis, a Kerr phase-interrogator has been proposed and demonstrated theoretically and experimentally. The Kerr phase-interrogator converts phase-shift $\Delta\phi$ of two sinusoidally-modulated optical signals (SMOS) into power of first-order sideband P_1 generated by nonlinear interaction between the two SMOSs in a Kerr medium, and acquires $\Delta\phi$ from sinusoidal dependence of P_1 on $\Delta\phi$.

Two theoretical models have been employed to explain the dependence of P_1 on $\Delta\phi$. The first model considers the generation of first-order sideband as a result of sinusoidal phase-modulations induced by SMOSs through Kerr effect. The phase-modulation-based model is intuitive and allows for conceptual understanding of the operation of the Kerr phase-interrogator in terms of superposition of the sinusoidal phase-modulations of two SMOSs. The second mode employs theory of four-wave mixing (FWM) and accounts for the generation of first-order sideband as a result of FWM process among the frequency components of the SMOSs. The FWM-based model is essential for acquiring insight into the operation of a Kerr phase-interrogator, and can account for the impact of chromatic dispersion (CD) of Kerr medium on the generation of first-order sidebands.

Birefringence and CD of Kerr medium used in a Kerr phase-interrogator play important roles in the nonlinear interaction of the SMOSs, and affect the generation of

first-order sidebands. In this thesis, vector analysis is performed on the nonlinear interaction between two orthogonally-polarized or co-polarized SMOSs in a Kerr medium with randomly-varying low birefringence. The analysis reveals that the nonlinear phase induced by self-phase modulation (SPM) in randomly birefringent Kerr medium is identical to the nonlinear phase induced by cross-phase modulation (XPM) between orthogonally-polarized SMOSs, whereas it is half to that induced by XPM between co-polarized SMOSs. Based on the vector analysis, sinusoidal variation of $P_1(\Delta\phi)$ is analyzed. The analysis indicates that the extinction-ratio of sinusoidal variation $P_1(\Delta\phi)$ is infinite due to the $P_1^{min}=0$ in the case of orthogonally-polarized SMOSs, whereas the extinction-ratio is 9 in the case of co-polarized SMOSs. In addition, sinusoidal variation of P_1 is dramatically perturbed by the phase noise of the laser sources when two co-polarized SMOSs are carried by identical wavelengths due to the interference between electric fields of the SMOSs. This study supplements the theory of Kerr phase-interrogator, and provides insight into the dependence of operation of the Kerr phase-interrogator on the polarization-states of SMOSs.

The impact of CD of Kerr medium on the generation of first-order sideband is also studied using the theory of FWM. The theoretical analysis and experimental results reveal that the CD of Kerr medium has impact on the magnitude, extinction ratio and phase-shift of the sinusoidal dependence of P_1 on $\Delta\phi$ by inducing intra-SMOS phase-mismatch and additional inter-SMOS phase-mismatch. This study suggests that a Kerr phase-interrogator should adopt Kerr medium with low or even

zero dispersion at the operation-wavelength rang to avoid CD-induced distortion of sinusoidal dependence of P_1 on $\Delta\phi$, which benefits high accuracy measurements based on Kerr phase-interrogator.

The proposed Kerr phase-interrogator has the merits of instantaneous response, utilization of all-optical signal processing, and being free from the coherence properties of light source. The function that converts phase variation into power variation and the merits of the Kerr phase-interrogator make it practical in various applications. In this thesis, four applications of Kerr phase-interrogator are theoretically and experimentally demonstrated. Firstly, a novel approach of CD measurement based on a Kerr phase-interrogator is presented. CD in four commercially available single mode fibers and one polarization-maintaining fiber is characterized. Secondly, a high-resolution temperature sensor utilizing the temperature dependence of the reflection group-delay in LC-FBGs is implemented. A Kerr phase-interrogator is utilized for conversion of temperature-induced variations of the reflection group-delay into power variations. Temperature sensing at a sensitivity of 1.122 rad/ ^{o}C and a resolution of 0.0089 ^{o}C is achieved. Next, a real-time CD monitor based on a Kerr phase-interrogator is achieved. CD induced group-delay difference of two SMOSs carried by two different wavelengths is converted to power variation by a Kerr phase-interrogator. The proposed CD monitor takes advantage of ultrafast response of the Kerr phase-interrogator and attains real-time CD monitoring. Monitoring of CD at a resolution of 0.196 ps /nm is achieved. High-resolution real-time CD monitoring opens ways for novel sensing applications. Finally, Kerr

phase-interrogator is used for incoherent optical frequency domain reflectometry (I-OFDR). The I-OFDR using a Kerr phase-interrogator eliminates the limitation of finite coherent length of the light source, and achieves measurement of long-range distance beyond the coherent length of the light source. Reflections measurement as far as 151 km at a spatial-resolution of 11.2 cm is implemented.

9.2 Future work

The resolution of Kerr phase-interrogator in term of phase-shift measurement is limited by the fluctuations δP_1 in P_1. The noise in the peak power P_p of the SMOSs at the input of Kerr medium dominantly contributes to δP_1 by inducing variations to $P_p \gamma L_{Kerr}$. The peak power noise mainly arises from the amplified spontaneous-emission noise of the Erbium-doped fiber amplifier (EDFA). The magnitude of δP_1 can be reduced by utilization of a highly nonlinear Kerr-medium such as a photonic crystal fiber to eliminate the need for the EDFA. Peak power noise also arises from external mechanical and thermal disturbances that cause birefringence variation in the optical paths which induce polarization variation on SMOSs before polarization beam combiner (PBC). These external disturbances are relatively slow and their contributions to δP_1 can be eliminated by using a feedback control-system that corrects the polarization of the SMOSs before the PBC.

Kerr phase-interrogator is employed in sensing and real-time monitoring applications utilizing the dependence of the measured physical parameter on the phase-shift of two SMOSs, and acquires the phase-shift by measuring P_1. Due to the

sinusoidal dependence of P_1 on the phase-shift, a value of P_1 corresponds to multiple values of the phase-shift. Therefore, a Kerr phase-interrogator is expected operating around the quadrature point of the sinusoidal variation of P_1 to attain one-to-one correspondence. In addition, operation round the quadrature point guarantees high-sensitivity measurement. The operation of Kerr phase-interrogator can be locked at quadrature point by adjusting the group-delay between two SMOSs using a variable delay line and a feedback-control electric circuit.

Currently, the Kerr phase-interrogator is not practical in the applications due to its complicated and large setup. Integrating the Kerr phase-interrogator into a more compact environment is a promising orientation. Owing to the development of integrated optical active and passive devices, the techniques of integrated optical circuits, and the realization of photolithographic microfabrication, it is possible to set up a Kerr phase-interrogator within miniaturized optical integrated circuits in sub-meter scale. The implementation of the Kerr phase-interrogator in compact environments will extend its applications to smart sensing, bio-sensing and large-scale quasi-distributed sensing.

Kerr phase-interrogator could also be used in the following applications:

Firstly, considering the fact that the reflection group-delay and reflection dispersion of a chirped FBG are temperature and stain dependent, Kerr phase-interrogator would be a promising method to implement simultaneous measurements of temperature and strain by measurements of variations in the reflection group-delay and reflection dispersion of a quadratically-chirped FBG

induced by temperature and strain. The key to implement simultaneous measurements of temperature and strain is the design of a chirped FBG, of which the group-delay spectrum is smooth and quadratically chirped. By adopting proper apodization on the chirped grating, this key can be solved and the simultaneous measurements are accomplishable.

Secondly, the implement of real-time CD monitoring using a Kerr phase-interrogator opens ways for novel sensing applications. Therefore, Kerr phase-interrogator based real-time sensing that utilizes dependence of the monitored physical parameter on the CD would be a promising future research.

In this thesis, all proposed sensing applications of Kerr phase-interrogator are point sensing. Distributed sensing is another promising orientation for Kerr phase-interrogator. Kerr phase-interrogator based I-OFDR has attained long-range detection of reflection points by acquiring the beat signal formed by the SMOS reflected by fault in the sensing path and the SMOS in the reference path. By effectively amplifying Rayleigh scattering, Kerr phase-interrogator can acquire the beat signals formed by Rayleigh scattering of the SMOS in the sensing path and the SMOS in the reference path allowing for distributed sensing. Therefore, high-spatial-resolution distributed sensing such as temperature or strain over long range would be achieved by utilization of Kerr phase-interrogator based I-OFDR. In addition, phase-sensitive optical time-domain reflectometer based on a Kerr phase-interrogator would be realized for distributed vibration measurement.

Bibliography

[1] G. P. Agrawal, *Nonlinear Fiber Optics*, 4th ed. (Academic, 2007).

[2] L. G. Cohen and C. Lin, "Pulse delay measurements in the zero material dispersion wavelength region for optical fibers," Appl. Opt. 16, 3136–3139 (1977).

[3] B. Costa, D. Mazzoni, M. Puleo, and E. Vezzoni, "Phase shift technique for the measurement of chromatic dispersion in optical fibers using led's," IEEE J. Quantum Electron.18(10), 1509–1515 (1982).

[4] A. L. Campillo, "Chromatic dispersion-monitoring technique based on phase-sensitive detection, " IEEE Photon. Technol. Lett. 17, 1241 – 1243 (2005).

[5] M. N. Petersen, Z. Pan, S. Lee, S. A. Havstad, and A. E. Willner, " Online chromatic dispersion monitoring and compensation using a single inband subcarrier tone," IEEE Photon. Technol. Lett. 14, 570– 572 (2002).

[6] K. J. Park, J. H. Lee, C. J. Youn, and Y. C. Chung, " A simultaneous monitoring technique for polarization-mode dispersion and group-velocity dispersion," in Proc. OFC , 199 –200 (2002).

[7] T. E. Dimmick, G. Rossi, and D. J. Blumenthal, "Optical dispersion monitoring technique using double sideband subcarriers," IEEE Photon. Technol. Lett. 12, 900 – 902 (2000).

[8] M. Abramowitz and I. A. Stegun, *Handbook of mathematical functions with Formulas, Graphs, and Mathematical Tables* (United States Department of Commerce and National Bureau of Standards, 1964).

[9] D. Colton and R. Kress, *Inverse acoustic and electromagnetic scattering theory* (Applied Mathematical Sciences, 93, 2nd ed. 1998)

[10] GillesCazelais,(wikipedia)
http://en.wikipedia.org/wiki/List_of_trigonometric_identities#cite_note-29

[11] M. Y. Frankel and R.D. Esman, “Optical Single-Sideband Suppressed-Carrier Modulation for Wide-Band Signal Processing,” J. of Lightwave Technol., 16, 859-862(1998).

[12] G. H. Smith, D. Novak and Z. Ahmed, “Technique for optical SSB generation to overcome dispersion penalties in fibre-radio system,” Electron. Lett. 33, 74–75 (1997).

[13] G. H. Smith, D. Novak, and Z. Ahmed, “Overcoming chromatic-dispersion effects in fiber-wireless systems incorporating external mod-ulators,” IEEE Trans. Microwave Theory Tech., 45, 1410–1415(1997).

[14] Q. Lin and G. P. Agrawal, “Vector theory of cross-phase modulation: Role of nonlinear polarization rotation,” IEEE J. Quantum Electron 40, 958–964 (2004).

[15] Q. Lin and G. P. Agrawal, “Vector theory of four-wave mixing: Polarization effects in fiber-optic parametric amplifiers,” J. Opt. Soc. Am. B21, 1216–1224 (2004).

[16] Q. Lin and G. P. Agrawal, “Vector theory of stimulated raman scattering and its application to fiber-based raman amplifiers,” J. Opt. Soc. Am. B20, 1616–1631 (2003).

[17] Hellwarth, J. Cherlow, and T. Yang, “Origin and frequency dependence of nonlinear optical susceptibilities of glasses,” Phys. Rev. A11, 964–967 (1975).

[18] J. N. Damask, Polarization Optics in Telecommunications. Springer, 2005.

[19] C. Ting-Kuang, N. Kagi, T. Fong, M. Marhic, and L. Kazovsky., “Crossphase modulation in dispersive fibers: theoretical and experimental investigation of the impact of modulation frequency,” Photon. Technol.Lett., 6, 733–736(1994).

[20] J. Lee and J. Ira, “Cross-phase modulation analysis using sinusoidally modulated signal,” in Applications of Photonic Technology 4, 4087,Proceedings of SPIE, 298–307(2000).

[21] N. Shibata, R. P. Braun, and R. G. Waarts, “Phase-mismatch dependence of efficiency of wave generation through four-wave mixing in a singlemode optical fiber,” IEEE J. Quantum Electron., QE-23(1987).

[22] M. W. Maeda, W. B. Sessa, W. I. . Way, A. Yi-Yan, L. Curtis, R. Spicer, and R. I. Laming, “The effect of four-wave mixing in fibers on optical frequency-division multiplexed systems,” J. Lightwave Technol., 8, 1402–1408(1990).

[23] Y. R. Shen, Principles of Nonlinear Optics. Wiley, 1984.

[24] S. G. Evanglides, L. F. Mollenauer, J. P. Gordon, and N. S. Bergano, “Polarization multiplexing with solitons,” J. Lightwave Technol. 10, 28–35(1992).

[25] P. K. A. Wai and C. R. Menyuk, “Polarization mode dispersion, decorrelation and diffusion in optical fibers with randomly varying birefringence,” J. Lightwave Technol. 14, 148–157(1996).

[26] T. I. Lakoba, “Concerning the equations governing nonlinear pulse propagation in randomly birefringent fibers,” J. Opt. Soc. Am. B. 13, 2006–2011(1996).

[27] L. G. Cohen and C. Lin, “Pulse delay measurements in the zero material dispersion wavelength region for optical fibers,” Appl. Opt. 16, 3136–3139 (1977).

[28] B. Costa, D. Mazzoni, M. Puleo, and E. Vezzoni, “Phase shift technique for the measurement of chromatic dispersion in optical fibers using led’s,” IEEE J. Quantum Electron.18(10), 1509–1515 (1982).

[29] K. S. Abedin, M. Hyodo, and N. Onodera, “Measurement of the chromatic dispersion of an optical fiber by use of a sagnac interferometer employing asymmetric modulation,” Opt. Lett.25(5), 299–301 (2000).

[30] L. Zong, F. Luo, S. Cui, and X. Cao, “Rapid and accurate chromatic dispersion measurement of fiber using asymmetric sagnac interferometer,” Opt. Lett.36(5), 660–662 (2011).

[31] M. Tateda, N. Shibata, and S. Seikai, “Interferometric method for chromatic dispersion measurement in a single-mode optical fiber,” Quantum Elec.17(3), 404–407 (1981).

[32] H.-T. Shang, “Chromatic dispersion measurement by white-light interferometry on metre-length single-mode optical fibres,” Electron. Lett.17(17), 603–605 (1981).

[33] M. Jinno, and T. Matsumoto, "Ultrafast, low power, and highly stable all-optical switching in an all polarization maintaining fiber Sagnac interferometer," IEEE Photon. Technol. Lett. 2, 349-351 (1990).

[34] N. Nishizawa, and T. Goto, "Widely wavelength-tunable ultrashort pulse generation using polarization maintaining optical fibers," IEEE J.Sel. Top. Quant. Electron. 7, 518-524 (2001).

[35] A. R. Dixon, Z. L. Yuan, J. F. Dynes, A. W. Sharpe and A. J. Shields, "Gigahertz decoy quantum key distribution with 1Mbit/s secure key rate," Opt. Express 16, 18790-18797 (2008).

[36] D. A. Flavin, "Dispersion of birefrinigence and differential group delay in polarization-maintaining fiber," Opt. Lett. 27, 1010-1012 (2002).

[37] P. Hlubina, "Dispersion of group and phase modal birefringence in elliptical-core fiber measured by white-light spectral interferometry," Opt. Express 11, 2793-2798 (2003).

[38] X. Chen, H. Zhang, D. Jia, T. Liu and Y. Zhang, "Spectral-domain measurement of chromatic dispersion difference of polarization modes in polarization-maintaining fibers," J. MOD. OPTIC. 58, 26-31 (2011).

[39] Y. Lu, C. Baker, L. Chen and X. Bao, “Chromatic-dispersion monitor based on a differential phase-shift method using a Kerr phase-interrogator,” IEEE Photonics. 7, 7101406 (2015).

[40] B. Christensen, J. Mark, G. Jacobsen, and . Bødtker, “Simple dispersion measurement technique with high resolution,” Electron. Lett. 29, 132–134 (1993).

[41] E. Al-Fakih, N. A. A. Osman, and F. R. M. Adikan, “The use of fiber Bragg grating sensors in biomechanics and rehabilitation applications: the state-of-the-art and ongoing research topics,” Sensors, 12, 12 890–12 926 (2012).

[42] Y. Rao, D. J. Webb, D. A. Jackson, L. Zhang, and I. Bennion, “In-fiber Bragg-grating temperature sensor system for medical applications,” J. Lightwave Technol. 15, 779–785 (1997).

[43] M. S. Milczewski, J. C. C. da Silva, I. Abe, L. Carvalho, R. N. Nogueira, A. S. Paterno, H. J. Kalinowski, and J. L. Pinto, “Determination of setting expansion of dental materials using fibre optical sensing,” Meas. Sci. Technol. 17, 1152–1156 (2006).

[44] P. Moyo, J. M. W. Brownjohn, R. Suresh, and S. C. Tjin, “Development of fiber Bragg grating sensors for monitoring civil infrastructure,”Eng. Struct. 27, 1828–1834 (2005).

[45] V. D. Marty, P. Ferdinand, E. Bocherens, R. Carbone, H. Beranger, S. Bourasseau, M. Dupont, and D. Balageas, “Embedded fiber Bragg grating sensors for industrial composite cure monitoring,” J. Intell. Mat. Syst. Str. 9, 785–787 (1998).

[46] H. Li, D. Li, and G. Song, “Recent applications of fiber optic sensors to health monitoring in civil engineering,” Eng. Struct. 26, 1647–1657 (2004).

[47] Y. Zhao, Y. Liao, and S. Lai, “Simultaneous measurement of down-hole high pressure and temperature with a bulk-modulus and FBG sensor,” Photon. Technol. Lett. 14, 1584–1586 (2002).

[48] C. E. Lee, J. J. Alcoz, Y. Yeh, W. N. Gibler, R. A. Atkins, and H. F. Taylor, “Optical fiber Fabry-Perot sensors for smart structures,” Smart Mater. Struct. 1, 123 (1992).

[49] G. Meltz, J. R. Dunphy, W. H. Glenn, J. D. Farina, and F. J. Leonberger, “Fiber optic temperature and strain sensors,” in Proc. SPIE, Fiber Optic Sensors II, 798, 104–114 (1987).

[50] D. C. Johnson, K. O. Hill, F. Bilodeau, and S. Faucher, “New design concept for a narrowband wavelength-selective optical tap and combiner,” Electron. Lett. 23, 668–669 (1987).

[51] H. Choi, H. F. Taylor, and C. E. Lee, “High performance fiber optic temperature sensor using low coherence interferometry,” Opt. Lett. 22, 1814–1816 (1997).

[52] T. Erdogan, “Fiber grating spectra,” J. Lightwave Technol. 15, 1277–1294 (1997).

[53] T. Erdogan, V. Mizrahi, P. J. Lemaire, and D. Monroe, “Decay of ultravio-letinduced fiber Bragg gratings,”J. Appl. Phys. 76, 73–80 (1994).

[54] G. Brambilla, “High-temperature fibre Bragg grating thermometer,” Electron. Lett. 38, 954–955 (2002).

[55] D. C. Kilper et al., “Optical performance monitoring,” J. Lightw. Technol. 22, 294 –304 (2004).

[56] W. H. Hatton and M. Nisimura, “Temperature dependence of chromatic dispersion in single mode fibers,” J. Lightwave Technol. 4, 1552 –1555 (1986).

[57] M. E. Lines, “Physical origin of the temperature dependence of chromatic dispersion in fused silica,” J. Appl. Phys. 73, 2075– 2079 (1993).

[58] T. Imai, T. Komukai, and M. Nakazawa, “Dispersion tuning of a linearly chirped fiber Bragg grating without a center wavelength shift by applying a strain gradient,” IEEE Photon. Technol. Lett. 10, 845 – 847 (1998).

[59] C. S. Goh, S. Y. Set, and K. Kikuchi, “Design and fabrication of a tunable

dispersion-slope compensating module based on strain-chirped fiber Bragg gratings, ” IEEE Photon. Technol. Lett. 16, 524 –526 (2004).

[60] F. N. Khan, A. P. T. Lau, C. Lu, and P. K. A. Wai, “ Chromatic dispersion monitoring for multiple modulation formats and data rates using sideband optical filtering and asynchronous amplitude sampling technique, ” Opt. Exp. 19, 1007 – 1015 (2011).

[61] B. Kozicki, A. Maruta, and K. Kitayama, “Transparent performance monitoring of RZ-DQPSK systems employing delay-tap sampling, ” J. Opt. Netw. 6, 1257 –1269 (2007).

[62] Z. Li and G. Li, “Chromatic dispersion and polarization-mode dispersion monitoring for RZ-DPSK signals based on asynchronous amplitude-histogram evaluation, ” J. Lightwave Technol. 24, 2859 – 2866 (2006).

[63] A. L. Campillo, “Chromatic dispersion-monitoring technique based on phase-sensitive detection, ” IEEE Photon. Technol. Lett. 17, 1241 – 1243 (2005).

[64] M. N. Petersen, Z. Pan, S. Lee, S. A. Havstad, and A. E. Willner, “ Online chromatic dispersion monitoring and compensation using a single inband subcarrier tone,” IEEE Photon. Technol. Lett. 14, 570– 572 (2002).

[65] K. J. Park, J. H. Lee, C. J. Youn, and Y. C. Chung, “ A simultaneous monitoring technique for polarization-mode dispersion and group-velocity dispersion,” in Proc. OFC , 199 –200 (2002).

[66] T. E. Dimmick, G. Rossi, and D. J. Blumenthal, “Optical dispersion monitoring technique using double sideband subcarriers,” IEEE Photon. Technol. Lett. 12, 900 – 902 (2000).

[67] W. Eickhoff and R. Ulrich, “Optical frequency domain reflectometry in single-mode fiber,” Appl. Phys. Lett. 39, 693–695 (1981).

[68] H. Barfuss and E. Brinkmeyer, “Modified optical frequency domain reflectometry with high spatial resolution for components of integrated optic systems,” J. Lightwave Technol. 7, 3–10 (1989).

[69] U. Glombitza and E. Brinkmeyer, “Coherent frequency-domain reflectometry for characterization of single-mode integrated-optical waveguides,” J. Lightwave Technol. 11, 1377–1384 (1993).

[70] J. P. Von der Weid, R. Passy, G. Mussi, and N. Gisin, “On the characterization of optical fiber network components with optical frequency domain reflectometry,”

J. Lightwave Technol.15, 1131–1141 (1997).

[71] M. Froggatt and J. Moore, “High-spatial-resolution distributed strain measurement in optical fiber with Rayleigh scatter,” Appl. Opt. 37, 1735–1740 (1998).

[72] G. Mussi, N. Gisin, R. Passy, and J. P. VonderWeid, “-152.5 dB sensitivity high dynamic-range optical frequency-domain reflectometry,” Electron. Lett.32, 926–927 (1996).

[73] J. Geng, C. Spiegelberg, and S. Jiang, “Narrow linewidth fiber laser for 100-km optical frequency domain reflectometry,” Photonics Tech. Lett. 17, 1827–1829 (2005).

[74] X. Fan, Y. Koshikiya, N. Araki, and F. Ito, “Field trials of PNC-OFDR in different environments for detecting short beat lengths,” IEEE Photon. Technol. Lett. 24, 1288–1291 (2012).

[75] X. Fan, Y. Koshikiya, and F. Ito, “Centimeter-level spatial resolution over 40 km realized by bandwidth-division phase-noise-compensated OFDR,” Opt. Express19, 19122–19128 (2011).

[76] Z. Ding, X. S. Yao, T. Liu, Y. Du, K. Liu, Q. Han, Z. Meng, J. Jiang, and H. Chen, “Long measurement range OFDR beyond laser coherence length,” IEEE Photon. Technol. Lett.25, 202–205 (2013).

[77] R. I. MacDonald, “Frequency domain optical reflectometer,” Appl. Opt. 20, 1840–1844 (1981).

[78] S. Venkatesh and D. W. Dolfi, “Incoherent frequency modulated cw optical reflectometry with centimeter resolution,” Appl. Opt. 29, 1323–1326 (1990).

[79] B. Schlemmer, “A simple and very effective method with improved sensitivity for fault location in optical fibers,” IEEE Photon. Technol. Lett. 3, 1037–1039 (1991).

[80] X. Bao and L. Chen, “Recent progress in distributed fiber optic sensors,” Sensors 12, 8601–8639 (2012).

Appendix

Appendix A

Sinusoidal phase-modulation ϕ_{NL} is given by

$$\begin{aligned}\phi_{NL} &= \frac{8\gamma L_{Kerr}}{9}\left\{0.5P_P\cos^2\left[0.5\omega_s\left(t-t_{\parallel}\right)\right]+0.5P_P\cos^2\left[0.5\omega_s\left(t-t_{\perp}\right)\right]\right\} \\ &= \frac{4\gamma L_{Kerr}P_p}{9}+\frac{4\gamma L_{Kerr}P_p}{9}\cos\left(\Delta\phi\right)\cos\left[\omega_s t-0.5\omega_s\left(t_{\perp}+t_{\parallel}\right)\right]\end{aligned} \tag{A.1}$$

where $\omega_s = 2\pi f_s$ and $\Delta\phi = 0.5\omega_s t_d$. Using (A.1), the perpendicular field component at the output of Kerr medium is written as

$$A_{\perp} = \sqrt{P_p/2}\cos\left[0.5\omega_s\left(t-t_{\perp}\right)\right]e^{im}e^{im\cos(\Delta\phi)\cos\left[\omega_s t-0.5\omega_s\left(t_{\perp}+t_{\parallel}\right)\right]} \tag{A.2}$$

with $m = 4\gamma L_{Kerr}P_P/9$. We will use the Jacobi-Anger expansion [8, 9]

$$e^{iz\cos\theta} = \sum_{n=-\infty}^{\infty} i^n J_n\left(z\right)e^{in\theta} \tag{A.3}$$

to obtain

$$\begin{aligned}&e^{im\cos(\Delta\phi)\cos\left[\omega_s-0.5\omega_s\left(t_{\perp}+t_{\parallel}\right)\right]} \\ &= \sum_{n=-\infty}^{\infty} i^n J_n\left(m\cos\left(\Delta\phi\right)\right)e^{in\left[\omega_s t-0.5\omega_s\left(t_{\perp}+t_{\parallel}\right)\right]} \\ &= \sum_{n=-\infty}^{\infty} i^n J_n\left(m\cos\left(\Delta\phi\right)\right)e^{in\left[\omega_s\left(t-t_{\perp}\right)-\Delta\phi\right]}\end{aligned} \quad . \tag{A.4}$$

Using Eq. (A.4) in Eq. (A.2) and replacing $\cos\left[0.5\omega_s\left(t-t_{\perp}\right)\right]$ with $0.5\left(e^{i0.5\omega_s(t-t_{\perp})}+e^{-i0.5\omega_s(t-t_{\perp})}\right)$ gives

$$A_{\perp} = \sqrt{\frac{P_p}{2}}\frac{e^{im}}{2}\left[\begin{aligned}&e^{i0.5\omega_s(t-t_{\perp})}\sum_{n=-\infty}^{\infty} i^n J_n\left(m\cos\left(\Delta\phi\right)\right)e^{i\left[n\omega_s(t-t_{\perp})-0.5n\omega_s t_d\right]} \\ &+e^{-i0.5\omega_s(t-t_{\perp})}\sum_{n=-\infty}^{\infty} i^n J_n\left(m\cos\left(\Delta\phi\right)\right)e^{i\left[n\omega_s(t-t_{\perp})-0.5n\omega_s t_d\right]}\end{aligned}\right] \tag{A.5}$$

which is rewritten as

$$A_{\perp}=\sqrt{\frac{P_p}{2}}\frac{e^{im}}{2}\left[\begin{array}{l}\sum_{n=-\infty}^{\infty} i^n e^{-i0.5n\omega_s t_d} J_n\left(m\cos\left(\Delta\phi\right)\right)e^{i(n+0.5)\omega_s\left(t-t_{\perp}\right)}\\ +\sum_{n=-\infty}^{\infty} i^n e^{-i0.5n\omega_s t_d} J_n\left(m\cos\left(\Delta\phi\right)\right)e^{i(n-0.5)\omega_s\left(t-t_{\perp}\right)}\end{array}\right]. \tag{A.6}$$

We will change n to n+1 in the second summation and combine the two summations to obtain

$$A_{\perp}=\sqrt{P_p/2}\frac{e^{im}}{2}\sum_{n=-\infty}^{\infty} i^n e^{-i0.5n\omega_s t_d}\left[\begin{array}{l}J_n\left(m\cos\left(\Delta\phi\right)\right)\\ +ie^{-i0.5\omega_s t_d} J_{n+1}\left(m\cos\left(\Delta\phi\right)\right)\end{array}\right]e^{i(n+0.5)\omega_s\left(t-t_{\perp}\right)}. \tag{A.7}$$

Splitting the summation for negative and positive n, Eq. (A.7) is rewritten as

$$A_{\perp}=\sqrt{\frac{P_p}{2}}\frac{e^{im}}{2}\left\{\begin{array}{l}\sum_{n=0}^{\infty} i^n e^{-i0.5n\omega_s t_d}\left[\begin{array}{l}J_n\left(m\cos\left(\Delta\phi\right)\right)\\ +ie^{-i0.5\omega_s t_d} J_{n+1}\left(m\cos\left(\Delta\phi\right)\right)\end{array}\right]e^{i(n+0.5)\omega_s\left(t-t_{\perp}\right)}\\ +\sum_{n=-\infty}^{-1} i^n e^{-i0.5n\omega_s t_d}\left[\begin{array}{l}J_n\left(m\cos\left(\Delta\phi\right)\right)\\ +ie^{-i0.5\omega_s t_d} J_{n+1}\left(m\cos\left(\Delta\phi\right)\right)\end{array}\right]e^{i(n+0.5)\omega_s\left(t-t_{\perp}\right)}\end{array}\right\}. \tag{A.8}$$

Replace n with -n and replace n by n+1 in the summation of $\sum_{n=-\infty}^{-1}$ leads to

$$A_{\perp}=\sqrt{\frac{P_p}{2}}\frac{e^{im}}{2}\left\{\begin{array}{l}\sum_{n=0}^{\infty} i^n e^{-i0.5n\omega_s t_d}\left[\begin{array}{l}J_n\left(m\cos\left(\Delta\phi\right)\right)+\\ ie^{-i0.5\omega_s t_d} J_{n+1}\left(m\cos\left(\Delta\phi\right)\right)\end{array}\right]e^{i(n+0.5)\omega_s\left(t-t_{\perp}\right)}+\\ \sum_{n=0}^{\infty} i^{-(n+1)} e^{i0.5(n+1)\omega_s t_d}\left[\begin{array}{l}J_{-(n+1)}\left(m\cos\left(\Delta\phi\right)\right)+\\ ie^{-i0.5\omega_s t_d} J_{-n}\left(m\cos\left(\Delta\phi\right)\right)\end{array}\right]e^{i(-n-0.5)\omega_s\left(t-t_{\perp}\right)}\end{array}\right\}. \tag{A.9}$$

We will replace $J_{-\nu}\left(z\right)=\left(-1\right)^{\nu} J_{\nu}\left(z\right)=i^{2\nu}J_{\nu}\left(z\right)$ in Eq. (A.9) to obtain

$$A_{\perp}=\sqrt{\frac{P_p}{2}}\frac{e^{im}}{2}\left\{\begin{array}{l}\sum_{n=0}^{\infty} i^n e^{-i0.5n\omega_s t_d}\left[\begin{array}{l}J_n\left(m\cos\left(\Delta\phi\right)\right)+\\ ie^{-i0.5\omega_s t_d} J_{n+1}\left(m\cos\left(\Delta\phi\right)\right)\end{array}\right]e^{i(n+0.5)\omega_s\left(t-t_{\perp}\right)}+\\ \sum_{n=0}^{\infty} i^{-(n+1)} e^{i0.5(n+1)\omega_s t_d}\left[\begin{array}{l}i^{2(n+1)} J_{n+1}\left(m\cos\left(\Delta\phi\right)\right)+\\ ie^{-i0.5\omega_s t_d} i^{2n} J_n\left(m\cos\left(\Delta\phi\right)\right)\end{array}\right]e^{i(-n-0.5)\omega_s\left(t-t_{\perp}\right)}\end{array}\right\} \tag{A.10}$$

which is reorganized as

$$A_{\perp}=\sqrt{\frac{P_p}{2}}\frac{e^{im}}{2}\left\{\begin{array}{l}\sum_{n=0}^{\infty}i^n e^{-i0.5n\omega_s t_d}\left[\begin{array}{l}J_n\left(m\cos\left(\Delta\phi\right)\right)+\\ ie^{-i0.5\omega_s t_d}J_{n+1}\left(m\cos\left(\Delta\phi\right)\right)\end{array}\right]e^{i(n+0.5)\omega_s(t-t_{\perp})}+\\ \sum_{n=0}^{\infty}i^n e^{i0.5(n+1)\omega_s t_d}\left[\begin{array}{l}iJ_{n+1}\left(m\cos\left(\Delta\phi\right)\right)+\\ e^{-i0.5\omega_s t_d}J_n\left(m\cos\left(\Delta\phi\right)\right)\end{array}\right]e^{i(-n-0.5)\omega_s(t-t_{\perp})}\end{array}\right\}. \quad (A.11)$$

The amplitude of the $\left|A_{\perp}(\omega)\right|^2_{(n+0.5)\omega_s}$ components is given by

$$\begin{aligned}P_{\perp,n}&=\left|\sqrt{\frac{P_p}{2}}\frac{e^{im}}{2}\left[J_n\left(m\cos\left(\Delta\phi\right)\right)+ie^{-i0.5\omega_s t_d}J_{n+1}\left(m\cos\left(\Delta\phi\right)\right)\right]\right|^2 \\ &=\frac{P_p}{8}\left[\begin{array}{l}J_n^2\left(m\cos\left(\Delta\phi\right)\right)+J_{n+1}^2\left(\mathrm{m}\cos\left(\Delta\phi\right)\right)\\ +2\sin\left(\Delta\phi\right)J_n\left(m\cos\left(\Delta\phi\right)\right)J_{n+1}\left(m\cos\left(\Delta\phi\right)\right)\end{array}\right]\end{aligned}. \quad (A.12)$$

Similarly, the power of *n*-order sideband of $\left|A_{\parallel}(\omega)\right|^2_{(n+0.5)\omega_s}$ is given by

$$P_{\parallel,n}=\frac{P_p}{8}\left[\begin{array}{l}J_n^2\left(m\cos\left(\Delta\phi\right)\right)+J_{n+1}^2\left(\mathrm{m}\cos\left(\Delta\phi\right)\right)\\ -2\sin\left(\Delta\phi\right)J_n\left(m\cos\left(\Delta\phi\right)\right)J_{n+1}\left(m\cos\left(\Delta\phi\right)\right)\end{array}\right]. \quad (A.13)$$

Accordingly, the powers of first-order sidebands of $A_{\perp}$ and $A_{\parallel}$ are respectively given by

$$P_{\perp,1}=\frac{P_p}{8}\left[\begin{array}{l}J_1^2\left(m\cos\left(\Delta\phi\right)\right)+J_2^2\left(\mathrm{m}\cos\left(\Delta\phi\right)\right)\\ +2\sin\left(\Delta\phi\right)J_1\left(m\cos\left(\Delta\phi\right)\right)J_2\left(m\cos\left(\Delta\phi\right)\right)\end{array}\right] \quad (A.14)$$

$$P_{\parallel,1}=\frac{P_p}{8}\left[\begin{array}{l}J_1^2\left(m\cos\left(\Delta\phi\right)\right)+J_2^2\left(\mathrm{m}\cos\left(\Delta\phi\right)\right)\\ -2\sin\left(\Delta\phi\right)J_1\left(m\cos\left(\Delta\phi\right)\right)J_2\left(m\cos\left(\Delta\phi\right)\right)\end{array}\right] \quad (A.15)$$

with $\Delta\phi=0.5\omega_s t_d$ and $m=4\gamma L_{Kerr}P_P/9$.

Appendix B

In the case that the peak powers of the perpendicular and the parallel components are different, the sinusoidal phase-modulation becomes

$$\phi_{NL}=\frac{8\gamma L_{Kerr}}{9}\left\{P_{\parallel}\cos^2\left[0.5\omega_s\left(t-t_{\parallel}\right)\right]+P_{\perp}\cos^2\left[0.5\omega_s\left(t-t_{\perp}\right)\right]\right\} \quad (B.1)$$

Using the following linear combinations of trigonometric functions

$$s\sin(x)+k\sin(x+a)=g\sin(x+b) \tag{B.2}$$

with $b=\arctan\left[k\sin(a)/\left(s+k\cos(a)\right)\right]$ and $g=\sqrt{s^2+k^2+2sk\cos(a)}$ [10], we rewrite the Eq. (B.1) as

$$\begin{aligned}\phi_{NL}&=\frac{8\gamma L_{Kerr}}{9}\left\{0.5\left(P_{\|}+P_{\perp}\right)+g\cos\left[\omega_s\left(t-t_{\|}\right)+b_{\|}\right]\right\}\\&=\frac{8\gamma L_{Kerr}}{9}\left\{0.5\left(P_{\|}+P_{\perp}\right)+g\cos\left[\omega_s\left(t-t_{\perp}\right)-b_{\perp}\right]\right\}\end{aligned} \tag{B.3}$$

where $b_{\|,\perp}=\arctan\left[P_{\perp,\|}\sin(2\Delta\phi)/\left(P_{\|,\perp}+P_{\perp,\|}\cos 2(\Delta\phi)\right)\right]$ with $\Delta\phi=0.5\omega_s t_d$ and $g=0.5\sqrt{P_{\|}^2+P_{\perp}^2+2P_{\|}P_{\perp}\cos(2\Delta\phi)}$. Accordingly, the perpendicular and the parallel field components at the output of Kerr medium can be written as

$$A_{\perp}=\sqrt{P_{\perp}}\cos\left[0.5\omega_s\left(t-t_{\perp}\right)\right]e^{i\phi_P}e^{im'\cos\left[\omega_s\left(t-t_{\perp}\right)-b_{\perp}\right]} \tag{B.4}$$

$$A_{\|}=\sqrt{P_{\|}}\cos\left[0.5\omega_s\left(t-t_{\|}\right)\right]e^{i\phi_P}e^{im'\cos\left[\omega_s\left(t-t_{\|}\right)+b_{\|}\right]} \tag{B.5}$$

where $m'=8\gamma L_{Kerr}g/9$ and $\phi_P=4\gamma L_{Kerr}\left(P_{\|}+P_{\perp}\right)/9$. We will repeat the operations from Eq. (A.2) to Eq. (A.13) to obtain the power of first order sideband of $A_{\perp}$ and $A_{\|}$ that are respectively given by

$$P_{\perp,1}=\frac{P_{\perp}}{4}\left[J_1^2\left(m'\right)+J_2^2\left(m'\right)+2\sin\left(b_{\perp}\right)J_1\left(m'\right)J_2\left(m'\right)\right] \tag{B.6}$$

$$P_{\|,1}=\frac{P_{\|}}{4}\left[J_1^2\left(m'\right)+J_2^2\left(m'\right)-2\sin\left(b_{\|}\right)J_1\left(m'\right)J_2\left(m'\right)\right]. \tag{B.7}$$

For $m'<0.2$, Eq. (B.6) and Eq. (B.7) reduce to

$$P_{\perp,1}=\frac{P_{\perp}}{4}J_1^2\left(m'\right) \tag{B.8}$$

$$P_{\|,1}=\frac{P_{\|}}{4}J_1^2\left(m'\right) \tag{B.9}$$

Using $J_1\left(m'\right)=\left(0.5m'\right)/\Gamma(2)$ and $m'=8\gamma L_{Kerr}g/9$ in Eq. (B.8) and Eq. (B.9), $P_{\perp,1}$ and $P_{\|,1}$ are finally given by

$$P_{\perp,1} = \frac{P_{\perp}\gamma^2 L^2_{Kerr}\left[P_{\parallel}^2 + P_{\perp}^2 + 2P_{\parallel}P_{\perp}\cos\left(2\Delta\phi\right)\right]}{81} \tag{B.10}$$

$$P_{\parallel,1} = \frac{P_{\parallel}\gamma^2 L^2_{Kerr}\left[P_{\parallel}^2 + P_{\perp}^2 + 2P_{\parallel}P_{\perp}\cos\left(2\Delta\phi\right)\right]}{81} \tag{B.11}$$

Appendix C

At the input of Kerr medium, the amplitudes of perpendicular and parallel components respectively are given by

$$A_{\perp} = \sqrt{\frac{P_p}{2}}\cos\left(0.5\omega_1\left(t - t_{\perp}\right)\right) \tag{C.1}$$

$$A_{\parallel} = \sqrt{\frac{P_p}{2}}\cos\left(0.5\omega_2\left(t - t_{\parallel}\right)\right) \tag{C.2}$$

where $t_{\parallel} = t_{\perp} + t_d$ and $\omega_2 = \omega_1 + \omega_b$. The perpendicular and parallel field components at output of Kerr medium are given by

$$A_{\perp} = \sqrt{\frac{P_p}{2}}\cos\left(0.5\omega_1\left(t - t_{\perp}\right)\right)\exp\left[j8\gamma P\left(t\right)L_{Kerr}/9\right] \tag{C.3}$$

$$A_{\parallel} = \sqrt{\frac{P_p}{2}}\cos\left(0.5\omega_2\left(t - t_{\parallel}\right)\right)\exp\left[j8\gamma P\left(t\right)L_{Kerr}/9\right] \tag{C.4}$$

where

$$\begin{aligned} P\left(t\right) &= \left|A_{\perp}\right|^2 + \left|A_{\parallel}\right|^2 \\ &= \frac{P_p}{4}\left[2 + \cos\left(\omega_1\left(t - t_{\perp}\right)\right) + \cos\left(\omega_2\left(t - t_{\parallel}\right)\right)\right] \end{aligned} . \tag{C.5}$$

Using $t_{\parallel} = t_{\perp} + t_d$ and $\omega_2 = \omega_1 + \omega_b$ in Eq. (C.5) gives

$$P\left(t\right) = \frac{P_p}{2}\left\{\begin{aligned} &1 + \cos\left[0.5\omega_d\left(t - t_{\perp}\right) - 0.5\left(\omega_1 + \omega_d\right)t_d\right] \\ &\times\cos\left[\omega_1\left(t - t_{\perp}\right) + 0.5\omega_d\left(t - t_{\perp}\right) - 0.5\left(\omega_1 + \omega_d\right)t_d\right] \end{aligned}\right\} \tag{C.6}$$

which can also be written as

$$P(t)=\frac{P_p}{2}\begin{Bmatrix}1+\cos\left[0.5\omega_d\left(t-t_{\parallel}\right)-0.5\left(\omega_2-\omega_d\right)t_d\right]\\ \times\cos\left[\omega_2\left(t-t_{\parallel}\right)-0.5\omega_d\left(t-t_{\parallel}\right)+0.5\left(\omega_2-\omega_d\right)t_d\right]\end{Bmatrix}. \tag{C.7}$$

Applying Eq. (C.6) into Eq. (C.3) gives

$$\begin{aligned}A_{\perp}=&\sqrt{\frac{P_p}{2}}\cos\left(0.5\omega_1\left(t-t_{\perp}\right)\right)\exp\left(jm\right)\\ &\times\exp\begin{Bmatrix}jm\cos\left[0.5\omega_d\left(t-t_{\perp}\right)-0.5\left(\omega_1+\omega_d\right)t_d\right]\\ \times\cos\left[\omega_1\left(t-t_{\perp}\right)+0.5\omega_d\left(t-t_{\perp}\right)-0.5\left(\omega_1+\omega_d\right)t_d\right]\end{Bmatrix}\end{aligned} \tag{C.8}$$

where $m=4/9\gamma P_p L_{Kerr}$. We will use the Jacobi-Anger expansion

$$e^{jz\cos\theta}=\sum_{n=-\infty}^{\infty}j^n J_n\left(z\right)e^{jn\theta} \tag{C.9}$$

to obtain

$$\begin{aligned}&\exp\begin{Bmatrix}jm\cos\left[0.5\omega_d\left(t-t_{\perp}\right)-0.5\left(\omega_1+\omega_d\right)t_d\right]\\ \times\cos\left[\omega_1\left(t-t_{\perp}\right)+0.5\omega_d\left(t-t_{\perp}\right)-0.5\left(\omega_1+\omega_d\right)t_d\right]\end{Bmatrix}\\ &=\sum_{n=-\infty}^{\infty}j^n e^{jn\left[\omega_1\left(t-t_{\perp}\right)+0.5\omega_d\left(t-t_{\perp}\right)-0.5\left(\omega_1+\omega_d\right)t_d\right]}J_n\left(\theta\right)\end{aligned} \tag{C.10}$$

where $\theta=m\cos\left[0.5\omega_d\left(t-t_{\perp}\right)-0.5\left(\omega_1+\omega_d\right)t_d\right]$. Therefore Eq. (C.8) becomes

$$\begin{aligned}A_{\perp}=&\sqrt{\frac{P_p}{2}}\cos\left(0.5\omega_1\left(t-t_{\perp}\right)\right)e^{jm}\\ &\times\sum_{n=-\infty}^{\infty}j^n e^{jn\left[\omega_1\left(t-t_{\perp}\right)+0.5\omega_d\left(t-t_{\perp}\right)-0.5\left(\omega_1+\omega_d\right)t_d\right]}J_n\left(\theta\right)\end{aligned}. \tag{C.11}$$

Using $\cos\left(0.5\omega_1\left(t-t_{\perp}\right)\right)=0.5\left[e^{j0.5\omega_1\left(t-t_{\perp}\right)}+e^{-j0.5\omega_1\left(t-t_{\perp}\right)}\right]$ in Eq. (C.11) gives

$$\begin{aligned}A_{\perp}=&\sqrt{\frac{P_p}{2}}\frac{e^{jm}}{2}\\ &\times\begin{Bmatrix}\sum_{n=-\infty}^{\infty}j^n e^{-j0.5n\left(\omega_1+\omega_d\right)t_d}e^{j\left[\left(n+0.5\right)\omega_1\left(t-t_{\perp}\right)+0.5n\omega_d\left(t-t_{\perp}\right)\right]}J_n\left(\theta\right)\\ +\sum_{n=-\infty}^{\infty}j^n e^{-j0.5n\left(\omega_1+\omega_d\right)t_d}e^{j\left[\left(n-0.5\right)\omega_1\left(t-t_{\perp}\right)+0.5n\omega_d\left(t-t_{\perp}\right)\right]}J_n\left(\theta\right)\end{Bmatrix}\end{aligned}. \tag{C.12}$$

Change n to n+1 in the second summation and we obtain

$$A_{\perp}=\sqrt{\frac{P_p}{2}}\frac{e^{jm}}{2}$$
$$\times\left\{\begin{array}{l}\displaystyle\sum_{n=-\infty}^{\infty} j^n e^{-j0.5n(\omega_1+\omega_d)t_d} e^{j\left[(n+0.5)\omega_1(t-t_{\perp})+0.5n\omega_d(t-t_{\perp})\right]} J_n(\theta) \\ \displaystyle+\sum_{n=-\infty}^{\infty} j^{n+1} e^{j\left[0.5\omega_d(t-t_{\perp})-0.5(n+1)(\omega_1+\omega_d)t_d\right]} e^{j\left[(n+0.5)\omega_1(t-t_{\perp})+0.5n\omega_d(t-t_{\perp})\right]} J_{n+1}(\theta)\end{array}\right\}. \qquad \text{(C.13)}$$

Combining the two summations leads to

$$A_{\perp}=\sqrt{\frac{P_p}{2}}\frac{e^{jm}}{2}$$
$$\times\sum_{n=-\infty}^{\infty}\left\{\begin{array}{l} j^n e^{-j0.5n(\omega_1+\omega_d)t_d} e^{j\left[(n+0.5)\omega_1(t-t_{\perp})+0.5n\omega_d(t-t_{\perp})\right]} \\ \times\left[J_n(\theta)+je^{j\left[0.5\omega_d(t-t_{\perp})-0.5(\omega_1+\omega_d)t_d\right]}J_{n+1}(\theta)\right]\end{array}\right\}. \qquad \text{(C.14)}$$

Split the summation for negative and positive n and we obtain

$$A_{\perp}=\sqrt{\frac{P_p}{2}}\frac{e^{jm}}{2}$$
$$\times\left\{\begin{array}{l}\displaystyle\sum_{n=0}^{\infty}\left\{\begin{array}{l} j^n e^{-j0.5n(\omega_1+\omega_d)t_d} e^{j\left[(n+0.5)\omega_1(t-t_{\perp})+0.5n\omega_d(t-t_{\perp})\right]} \\ \times\left[J_n(\theta)+je^{j\left[0.5\omega_d(t-t_{\perp})-0.5(\omega_1+\omega_d)t_d\right]}J_{n+1}(\theta)\right]\end{array}\right\} \\ \displaystyle+\sum_{n=-\infty}^{-1}\left\{\begin{array}{l} j^n e^{-j0.5n(\omega_1+\omega_d)t_d} e^{j\left[(n+0.5)\omega_1(t-t_{\perp})+0.5n\omega_d(t-t_{\perp})\right]} \\ \times\left[J_n(\theta)+je^{j\left[0.5\omega_d(t-t_{\perp})-0.5(\omega_1+\omega_d)t_d\right]}J_{n+1}(\theta)\right]\end{array}\right\}\end{array}\right\}. \qquad \text{(C.15)}$$

In the second summation, replacing n with $-n$ and then changing n by $n+1$ results in

$$A_{\perp}=\sqrt{\frac{P_p}{2}}\frac{e^{jm}}{2}$$
$$\times\left\{\begin{array}{l}\displaystyle\sum_{n=0}^{\infty}\left\{\begin{array}{l} j^n e^{-j0.5n(\omega_1+\omega_d)t_d} e^{j\left[(n+0.5)\omega_1(t-t_{\perp})+0.5n\omega_d(t-t_{\perp})\right]} \\ \times\left[J_n(\theta)+je^{j\left[0.5\omega_d(t-t_{\perp})-0.5(\omega_1+\omega_d)t_d\right]}J_{n+1}(\theta)\right]\end{array}\right\} \\ \displaystyle+\sum_{n=0}^{\infty}\left\{\begin{array}{l} j^{-(n+1)} e^{j0.5(n+1)(\omega_1+\omega_d)t_d} e^{j\left[(-n-0.5)\omega_1(t-t_{\perp})-0.5(n+1)\omega_d(t-t_{\perp})\right]} \\ \times\left[J_{-(n+1)}(\theta)+je^{j\left[0.5\omega_d(t-t_{\perp})-0.5(\omega_1+\omega_d)t_d\right]}J_{-n}(\theta)\right]\end{array}\right\}\end{array}\right\}. \qquad \text{(C.16)}$$

Replace $J_{-v}(z)=(-1)^v J_{-v}(z)$ in Eq. (C.16) and we obtain

$$A_{\perp}=\sqrt{\frac{P_p}{2}}\frac{e^{jm}}{2}$$
$$\times\left\{\begin{array}{l}\sum_{n=0}^{\infty}\left\{\begin{array}{l}j^n e^{-j0.5n(\omega_1+\omega_d)t_d}e^{j\left[(n+0.5)\omega_1(t-t_{\perp})+0.5n\omega_d(t-t_{\perp})\right]}\\ \times\left[J_n(\theta)+je^{j\left[0.5\omega_d(t-t_{\perp})-0.5(\omega_1+\omega_d)t_d\right]}J_{n+1}(\theta)\right]\end{array}\right\}\\ +\sum_{n=0}^{\infty}\left\{\begin{array}{l}j^{-(n+1)}e^{j0.5(n+1)(\omega_1+\omega_d)t_d}e^{j\left[(-n-0.5)\omega_1(t-t_{\perp})-0.5(n+1)\omega_d(t-t_{\perp})\right]}\\ \times\left[(-1)^{n+1}J_{n+1}(\theta)+je^{j\left[0.5\omega_d(t-t_{\perp})-0.5(\omega_1+\omega_d)t_d\right]}(-1)^n J_n(\theta)\right]\end{array}\right\}\end{array}\right\}. \qquad \text{(C.17)}$$

Using $(-1)^{\nu}=(j)^{2\nu}$ in Eq. (C.17) results in

$$A_{\perp}=\sqrt{\frac{P_p}{2}}\frac{e^{jm}}{2}$$
$$\times\left\{\begin{array}{l}\sum_{n=0}^{\infty}\left\{\begin{array}{l}j^n e^{-j0.5n(\omega_1+\omega_d)t_d}e^{j\left[(n+0.5)\omega_1(t-t_{\perp})+0.5n\omega_d(t-t_{\perp})\right]}\\ \times\left[J_n(\theta)+je^{j\left[0.5\omega_d(t-t_{\perp})-0.5(\omega_1+\omega_d)t_d\right]}J_{n+1}(\theta)\right]\end{array}\right\}\\ +\sum_{n=0}^{\infty}\left\{\begin{array}{l}j^n e^{j0.5(n+1)(\omega_1+\omega_d)t_d}e^{j\left[(-n-0.5)\omega_1(t-t_{\perp})-0.5(n+1)\omega_d(t-t_{\perp})\right]}\\ \times\left[jJ_{n+1}(\theta)+e^{j\left[0.5\omega_d(t-t_{\perp})-0.5(\omega_1+\omega_d)t_d\right]}J_n(\theta)\right]\end{array}\right\}\end{array}\right\}. \qquad \text{(C.18)}$$

After reorganization, Eq. (C.18) becomes

$$A_{\perp}=\sqrt{\frac{P_p}{2}}\frac{e^{jm}}{2}$$
$$\times\left\{\begin{array}{l}\sum_{n=0}^{\infty}\left\{\begin{array}{l}j^n e^{-j0.5n(\omega_1+\omega_d)t_d}e^{j\left[(n+0.5)\omega_1(t-t_{\perp})+0.5n\omega_d(t-t_{\perp})\right]}\\ \times\left[J_n(\theta)+je^{j\left[0.5\omega_d(t-t_{\perp})-0.5(\omega_1+\omega_d)t_d\right]}J_{n+1}(\theta)\right]\end{array}\right\}\\ +\sum_{n=0}^{\infty}\left\{\begin{array}{l}j^n e^{j0.5(n+1)(\omega_1+\omega_d)t_d}e^{j\left[(-n-0.5)\omega_1(t-t_{\perp})-0.5n\omega_d(t-t_{\perp})\right]}\\ \times\left[e^{j\left[-0.5(\omega_1+\omega_d)t_d\right]}J_n(\theta)+je^{j\left[-0.5\omega_d(t-t_{\perp})\right]}J_{n+1}(\theta)\right]\end{array}\right\}\end{array}\right\}. \qquad \text{(C.19)}$$

The amplitude of the $\left|A_{\perp}(\omega)\right|^2_{(n+0.5)\omega_1}$ components is given by (for positive *n*)

$$\begin{array}{l}\frac{P_p}{8}\left|\left[J_n(\theta)+je^{j0.5\left[\omega_d(t-t_{\perp})-(\omega_1+\omega_d)t_d\right]}\right]J_{n+1}(\theta)\right|^2\\ =\frac{P_p}{8}\left[\begin{array}{l}J_n^2(\theta)+J_{n+1}^2(\theta)\\ -2\sin\left(0.5\omega_d(t-t_{\perp})-0.5(\omega_1+\omega_d)t_d\right)J_n(\theta)J_{n+1}(\theta)\end{array}\right]\end{array} \qquad \text{(C.20)}$$

or (for negative *n*)

$$\begin{aligned}&\frac{P_p}{8}\left\|\left[e^{j\left[-0.5(\omega_1+\omega_d)t_d\right]}J_n(\theta)+je^{j\left[-0.5\omega_d(t-t_\perp)\right]}J_{n+1}(\theta)\right]\right\|^2\\&=\frac{P_p}{8}\begin{bmatrix}J_n^2(\theta)+J_{n+1}^2(\theta)\\-2\sin\left(-0.5\omega_d(t-t_\perp)+0.5(\omega_1+\omega_d)t_d\right)J_n(\theta)J_{n+1}(\theta)\end{bmatrix}.\end{aligned}\tag{C.21}$$

Similarly, the amplitude of the $\left|A_{\parallel}(\omega)\right|^2_{(n+0.5)\omega_1}$ component is given by (for positive *n*)

$$\begin{aligned}&P_p/8\left\|\left[e^{j\left[0.5\omega_d(t-t_\perp)-0.5(\omega_1+\omega_d)t_d\right]}J_n(\theta)+jJ_{n+1}(\theta)\right]\right\|^2\\&=P_p/8\begin{bmatrix}J_n^2(\theta)+J_{n+1}^2(\theta)\\+2\sin\left(0.5\omega_d(t-t_\perp)-0.5(\omega_1+\omega_d)t_d\right)J_n(\theta)J_{n+1}(\theta)\end{bmatrix}\end{aligned}\tag{C.22}$$

or (for negative *n*)

$$\begin{aligned}&P_p/8\left\|\left[e^{j\left[-0.5\omega_d(t-t_\perp)\right]}J_n(\theta)+je^{j\left[-0.5(\omega_1+\omega_d)t_d\right]}J_{n+1}(\theta)\right]\right\|^2\\&=P_p/8\begin{bmatrix}J_n^2(\theta)+J_{n+1}^2(\theta)\\+2\sin\left(-0.5\omega_d(t-t_\perp)+0.5(\omega_1+\omega_d)t_d\right)J_n(\theta)J_{n+1}(\theta)\end{bmatrix}.\end{aligned}\tag{C.23}$$

The spectral components P_n for positive *n* is calculated from

$$\begin{aligned}P_n&=\left|A_\perp(\omega)\right|^2_{(n+0.5)\omega_s}+\left|A_{\parallel}(\omega)\right|^2_{(n+0.5)\omega_s}\\&=\frac{P_p}{4}\left[J_n^2(\theta)+J_{n+1}^2(\theta)\right]\end{aligned}\tag{C.24}$$

and for negative *n* is calculated from

$$\begin{aligned}P_n&=\left|A_\perp(\omega)\right|^2_{(-n-0.5)\omega_s}+\left|A_{\parallel}(\omega)\right|^2_{(-n-0.5)\omega_s}\\&=\frac{P_p}{4}\left[J_n^2(\theta)+J_{n+1}^2(\theta)\right]\end{aligned}.\tag{C.25}$$

The Bessel functions have the following asymptotic forms. For small arguments $0<x\ll\sqrt{\alpha+1}$, one obtains, when α is not a negative integer $J_\alpha(x)\approx\frac{1}{\Gamma(\alpha+1)}\left(\frac{x}{2}\right)^\alpha$. Therefore, the power both positive and negative *n*=1 is given by

$$P_1=P_p/8\left[\frac{1}{\Gamma(2)}\left(\frac{\theta}{2}\right)\right]^2+P_p/8\left[\frac{1}{\Gamma(3)}\left(\frac{\theta}{2}\right)^2\right]^2.\tag{C.26}$$

Equation (C.26) can be reduced to

$$P_1 = P_p / 8\left[\frac{1}{\Gamma(2)}\left(\frac{\theta}{2}\right)\right]^2 \tag{C.27}$$

for $m < 0.2$ because the value of $\left[\frac{1}{\Gamma(3)}\left(\frac{\theta}{2}\right)^2\right]^2$ is much smaller than that of $\left[\frac{1}{\Gamma(2)}\left(\frac{\theta}{2}\right)\right]^2$. Using $\Gamma(2)=1$ and $\theta = \phi_m / 2\cos\left(0.5\omega_d\left(t-t_\perp\right)-0.5\left(\omega_1+\omega_d\right)t_d\right)$ gives

$$P_1 = \frac{\gamma^2 P_P^3 L_{Kerr}^2}{162}\cos^2\left[0.5\omega_d\left(t-t_\perp\right)-0.5\left(\omega_1+\omega_d\right)t_d\right] \tag{C.28}$$

Using $\omega_d = \omega_2 - \omega_1$, $\omega_{j=1,2} = 2\pi f_{1,2}$ and $f_{1,2} = f_0 + \rho\left(t - t_{\perp,\|}\right)$, Eq. (C.28) becomes

$$P_1 = \frac{\gamma^2 P_P^3 L_{Kerr}^2}{162}\cos^2\left(\pi f_d t + \phi_\Delta\right) \tag{C.29}$$

with $\phi_\Delta = -\pi f_d t_\perp + \pi\left(f_1 - f_d\right)t_d$.

Curriculum Vitae

Full name Yang Lu

Education

Ph.D Candidate (Sep.2012- present)

Department of Physics

University of Ottawa, Ottawa, Canada

Supervisors: Prof. Xiaoyi Bao

M.Sc. (Sep.2009- Dec.2011)

College of Optoelectronic Science and Engineering

National University of Defense Technology, Changsha, P. R. China

Supervisors: Prof. Zhou Meng

B.S. (Sep.2005-Jun.2009)

College of Optoelectronic Science and Engineering

National University of Defense Technology, Changsha, P. R. China

Publications

Journal Paper

1. **Y. Lu**, C. Baker, L. Chen and X. Bao. “Polarization dependence of nonlinear interaction between sinusoidally-modulated optical signals in randomly birefringent Kerr medium,” Appl. Opt. 54(32), 9563-9567(2015).

2. **Y. Lu**, C. Baker, L.Chen, and X. Bao, “Study of chromatic-dispersion impact on nonlinear interaction between two sinusoidally modulated optical signals using theory of four-wave mixing,” J. Opt. Soc. Am. B: Opt. Phys. Accepted.

3. **Y. Lu**, C. Baker, L.Chen, and X. Bao, “Chromatic-dispersion monitor based on a differential phase-shift method using a Kerr phase-interrogator,” IEEE Photonics J. 7(2), 7101406(2015).

4. **Y. Lu**, C. Baker, L. Chen, and X. Bao, “Group-delay based temperature sensing in linearly-chirped fiber Bragg gratings using a Kerr phase-interrogator,” J. Lightwave Technol. 33(2), 381-385(2015).

5. C. Baker, **Y. Lu**, J. Song, and X. Bao, “Incoherent optical frequency domain reflectometry based on a Kerr phase-interrogator,” Opt. Express 22(13), 15370-15 375(2014).

6. C. Baker, **Y. Lu**, and X. Bao, “Chromatic-dispersion measurement by modulation phase-shift method using a Kerr phase-interrogator,” Opt. Express 22(19), 22314-22 319(2014).

7. M. Pang, X. Bao, L. Chen, Z. Qin, **Y. Lu**, and P. Lu, “Frequency stabilized coherent Brillouin random fiber laser: theory and experiments,” Opt. Express 21(22), 27155-27168(2013).

Conference paper and presentation

1. **Y. Lu**, C. Baker, and X. Bao, “Dispersion characterization of group birefringence in polarization-maintaining fiber using a Kerr phase-interrogator,” the 5th Asia Pacific Optical Sensors Conference, 2015, Jeju, Korea (Oral).

2. Yanping Xu, Meiqi Ren, **Yang Lu**, Ping Lu, Xiaoyi Bao, and Sophie LaRochelle, “Multi-parameter sensing based on the stimulated Brillouin scattering of higher-order acoustic modes in OAM fiber,” the 24th international conference on optical fiber sensors, 2015, Curitiba, Brazil (Oral).